

SINGLE MOLECULE DETECTION AND FLUORESCENCE CORRELATION SPECTROSCOPY ON SURFACES

THÈSE N° 3433 (2005)

PRÉSENTÉE À LA FACULTÉ SCIENCES ET TECHNIQUES DE L'INGÉNIEUR

Institut d'imagerie et optique appliquée

SECTION DE MICROTECHNIQUE

ÉCOLE POLYTECHNIQUE FÉDÉRALE DE LAUSANNE

POUR L'OBTENTION DU GRADE DE DOCTEUR ÈS SCIENCES

PAR

Kai HABLER

Mag.rer.nat. , Universität Wien, Autriche
de nationalité autrichienne

acceptée sur proposition du jury:

Prof. T. Lasser, directeur de thèse
Prof. O. Martin, rapporteur
Prof. R. Rigler, rapporteur
Prof. H. Vogel, rapporteur
Prof. J. Widengren, rapporteur

Lausanne, EPFL
2006

Abstract

In this thesis a new approach for single molecule detection and analysis is explored. This approach is based on the combination of two well established methods, fluorescence correlation spectroscopy (FCS) and total internal reflection fluorescence microscopy (TIRFM). In contrast to most existing fluorescence spectroscopy techniques, the subject of primary interest in FCS is not the fluorescence intensity itself but the random intensity fluctuation around the mean value. Intensity fluctuations are induced by thermal noise in a minute observation volume, which is in classical FCS the confocal volume of a confocal microscope. E.g. FCS is commonly utilized to investigate diffusion. In this case, diffusing fluorescent molecules entering or leaving the observation volume cause intensity fluctuations, which are analyzed by calculating the temporal autocorrelation of the observed signal. The autocorrelation is a measure for the self-similarity of a signal and contains information about the average fluctuation strength and duration. The confocal observation volume, i.e. the measurement volume that is actually seen by the detector is approximately given by the product of the optical transfer function with the fluorescence exciting intensity distribution of a focused laser beam. To achieve a high signal-to-background ratio a small observation volume is absolutely essential, first of all because the background from e.g. scattered light increases with the size of the observation volume. Second, a small volume assures for a small average number of fluorophores inside the observation volume and therefore for a high fluctuation amplitude i.e. FCS signal.

This thesis proposes and discusses an alternative to confocal FCS specially conceived for measurements on surface-bound molecular systems, such as biological receptors or immobilized enzymes. In contrast to confocal FCS, fluorescence is excited within an evanescent field generated by total internal reflection (TIR) of a laser beam at the interface between a microscope coverslip and the sample. This is achieved by focusing the laser beam off-axis at the back focal plane of a high NA oil-immersion objective. The collimated beam that emerges from the objective is incident at an oblique angle at the coverslip-sample interface and totally internal reflected. In contrast to confocal FCS, the generated observation volume is completely confined to the surface and background fluorescence as well as scattered light from the bulk is efficiently suppressed.

Our method, called objective-type TIR-FCS in the following, features an increased collection efficiency compared to existing techniques that combine evanescent wave excitation and FCS. Existing techniques use total internal reflection on the surface of a prism to generate an evanescent field. This leads to a configuration where the choice of objectives is limited to air or water-immersion objectives. In our system we use a high NA oil-immersion objective, specially conceived for TIR applications, which collects light efficiently. The collection efficiency is further enhanced by a naturally occurring change of the emission properties of fluorophores close to interfaces between dielectric media. The presence of the interface favors emission into the optically denser medium so that about 60% of the emitted light can be collected. These factors, together with a reduced observation volume lead to a very sensitive method with a high potential for applications in single molecule detection and analysis. The performance of the proposed method was experimentally shown for measurements on molecules subject to Brownian motion and

binding to modified coverslips. In particular, it was experimentally shown that objective-type TIR-FCS features high signal-to-background ratio on a single molecule level.

In this thesis, concise derivations of analytical expressions for autocorrelation functions for diffusion and most important, the case of ligands reversibly binding to a single and localized binding site are presented. The derived model allows for the quantitative determination of binding rates for a single receptor. We strongly believe that the application of these results in the context of investigations of receptor-ligand binding kinetics will allow for deeper understanding of cellular signaling.

Moreover, this thesis discusses the applicability of the proposed method in enzymology. Enzymes, as most proteins are subject to continuous changes of their structure or conformation. These conformational changes are correlated with the function of the enzyme. In the discussed example the enzyme catalyzes an oxidation where the product is fluorescent but the substrate is not. The function of the enzyme i.e. the recurring product formation leads to observable intensity fluctuations. Since function and conformational states are correlated, conformational fluctuations can be investigated by means of FCS as was already shown for confocal FCS.

A technique closely related to FCS is fluorescence lifetime spectroscopy (where lifetime refers to the mean lifetime of the electronic excited state). Whereas in FCS the relaxation after random deviations from thermal equilibrium is investigated, relaxation of excited fluorophores towards their electronic ground-state is investigated in lifetime spectroscopy. The technique is used for e.g. discrimination between fluorophores with different lifetimes. Lifetime spectroscopy combined with imaging is used in many domains of life-science, including microarray reading and medical diagnostics. In preliminary work we developed a novel approach to perform lifetime imaging that is based on a multiplexing technique. The proposed method requires no mechanical scanning stage and only a single-point detector. Furthermore, noise is reduced under certain circumstances if the signal is low. Characteristics of this technique as well as advantages and disadvantages are shortly discussed.

Zusammenfassung

Gegenstand dieser Arbeit ist eine neue Methode zur Einzelmolekül Detektion. Grundlage der vorgeschlagenen Methode ist die Kombination zweier weit verbreiteter Techniken: 'fluorescence correlation spectroscopy' (FCS) und 'total internal reflection fluorescence microscopy' (TIRFM). In FCS ist die Messgröße nicht die Intensität selbst, sondern, im Gegensatz zum Großteil der auf Fluoreszenz Spektroskopie basierenden Methoden, die Schwankung derselben. Die Intensitätsschwankungen werden durch thermodynamische Fluktuationen in einem äußerst kleinen Beobachtungsvolumen ausgelöst. Dieses Volumen ist im Fall von klassischem FCS das konfokale Volumen eines konfokalen Mikroskops. Eine typische Anwendung von FCS ist die Messung von Diffusionskoeffizienten. Fluktuationen in der Fluoreszenz-Intensität werden dann durch Brownsche Bewegung die zur Schwankungen der Anzahl von Molekülen im Volumen führt, ausgelöst. Zur Analyse wird die Autokorrelation des gemessenen Fluoreszenzsignals berechnet. Die Autokorrelation ist ein Maß der "Selbstähnlichkeit" des Signals und enthält Information zur mittleren Stärke und Dauer der Schwankungen. Ein kleines Beobachtungsvolumen ist in dieser Art von Messung äußerst wichtig um ein hohes Signal-zu-Hintergrund Verhältniss zu erreichen. Ein kleines Volumen garantiert einerseits, dass der gemessene Anteil von Streulicht gering ist und andererseits, dass die mittlere Anzahl der fluoreszierenden Moleküle im Beobachtungsvolumen klein ist. Daraus folgt, dass die Amplitude der Fluktuationen und daher das FCS Signal hoch ist. Das Beobachtungsvolumen ist im Fall von konfokalem FCS näherungsweise durch das Produkt der optischen Transferfunktion der konfokalen Lochblende mit der 'point-spread function' des optischen Systems gegeben. Die Größe dieses Volumens bewegt sich typischerweise zw. 0.2 fl und 1 fl.

In dieser Arbeit wird eine Alternative zu konfokalem FCS vorgestellt, welche für Messung an biologischen Systemen (z.B. Enzyme und Rezeptoren) an Oberflächen konzipiert wurde. Fluoreszenz wird in diesem Fall innerhalb eines evaneszenten Feldes angeregt, welches durch totale interne Reflexion (TIR) eines Laserstrahls an der Grenzfläche zwischen einem Mikroskop Deckglas und dem Sample generiert wird. Dazu wird der Laserstrahl parallel zur optischen Achse verschoben und auf die hintere Brennebene eines Ölimmersionsobjektivs fokussiert. Der Laserstrahl ist daher nach Austritt aus dem Objektiv kollimiert und fällt unter einem schiefen Winkel (der den kritischen Winkel übertrifft) auf die Sample-Deckglas Trennfläche wo er reflektiert wird. Im Gegensatz zu konfokalem FCS ist das so erzeugte Beobachtungsvolumen auf die unmittelbare Nähe zur Grenzfläche beschränkt und das Hintergrundsignal verursacht durch Raman Streuung im Sample oder ungewollter, nicht an der Oberfläche generierter Fluoreszenz effizient unterdrückt.

Unsere Methode, die wir im folgenden 'objective-type TIR-FCS' nennen profitiert von einer sehr hohen Fluoreszenz-Kollektionseffizienz des optischen Systems. Existierende TIR-FCS Methoden verwenden TIR an der Oberfläche eines Prismas um das evaneszente Feld zu erzeugen. Das führt zu einer Konfiguration in der die Wahl des Licht-sammelnden Objektivs auf Luft und Wasser-Immersionsojektive beschränkt ist. Wir verwenden in unserem Aufbau ein Ölimmersionsobjektiv mit hoher Apertur welches speziell für TIR Applikationen entwickelt

wurde und Fluoreszenz effizient sammelt. Weiters ändern sich die Abstrahlcharakteristika von Fluorophoren in der Nähe von Grenzflächen zwischen Dielektrika und zwar in einer Art und Weise die die Kollektionseffizienz in 'objective-type TIR-FCS' günstig beeinflusst. Die Grenzfläche begünstigt die Abstrahlung in das optisch dichtere Medium, sodass mehr als 60% des emittierten Lichtes gesammelt werden kann (unter Vernachlässigung von Reflektionsverlusten). Diese Faktoren gemeinsam mit einem kleinen Beobachtungsvolumen machen aus 'objective-type TIR-FCS' eine höchst sensitive Methode, geeignet für Einzelmolekül Detektion und Analyse. Die Leistungsfähigkeit von 'objective-type TIR-FCS' wurde experimentell am Beispiel diffundierender und an das Deckglas bindender Fluorophore gezeigt. Einzelmolekül Messungen konnten mit hohem Signal-zu-Hintergrund Verhältniss durchgeführt werden.

In der vorliegenden Arbeit werden weiters Ableitungen analytischer Ausdrücke für die Autokorrelationsfunktionen diffundierender Moleküle und Liganden die an einen einzelnen, lokalisierten Rezeptor binden präsentiert. Das präsentierte mathematische Modell für Bindung erlaubt die quantitative Bestimmung der Bindungsrate eines isolierten Rezeptors. Wir sind der Meinung, dass die Anwendung dieser Ergebnisse im Rahmen von Untersuchungen an Rezeptor-Liganden Systemen zu einem tieferen Verständniss der Signalverarbeitungsprozesse in Zellen führen wird.

Weiters wird in dieser Arbeit die Anwendbarkeit der Methode im Bereich der Enzymologie besprochen. Die Struktur oder Konformation von Enzymen ist ständiger thermodynamischer Schwankungen unterworfen. Konformationsschwankungen sind an die Funktion des Enzyms gekoppelt. In dem beschriebenen Beispiel katalysiert das Enzym eine Reaktion die ein nicht-fluoreszierendes Substrat in ein fluoreszierendes Produkt umwandelt. Die Produktbildung führt zu beobachtbaren Intensitätsfluktuationen. Da die Funktion des Enzyms an seine Konformation gekoppelt ist, kann FCS eingesetzt werden um die Konformationsänderungen zu untersuchen, wie für den Fall konfokalen FCSs bereits demonstriert wurde.

Eine dem FCS ähnliche, auf Fluoreszenz basierende Messtechnik ist 'fluorescence lifetime spectroscopy'. In FCS ist der Gegenstand der Messung die Relaxation eines molekularen Systems nach einer stochastischen Abweichung vom thermodynamischen Gleichgewicht. In 'fluorescence lifetime spectroscopy' ist die Relaxation von Fluorophoren zu ihrem elektronischen Grundzustand nach Anregung durch Photonabsorption Gegenstand der Messung. Diese Technik wird z.B. verwendet um verschiedene Fluorophore aufgrund ihrer Lebenszeiten (mittlere Verweildauer im angeregten Zustand) zu unterscheiden. Die Verbindung dieser Technik mit Mikroskopie, genannt 'fluorescence lifetime imaging' (FLIM), kommt in vielen Bereichen der Biologie und der Medizin zur Anwendung. Im Rahmen von Arbeiten die der Entwicklung von 'objective-type TIR-FCS' vorausgingen, wurde eine neue Methode entwickelt um FLIM Messungen zu realisieren. Die vorgeschlagene Methode, 'Hadamard lifetime imaging' (HLI) genannt, welche auf einer Multiplexing Technik beruht, kommt ohne mechanisches Scannen der Probe aus; weiters wird nur ein einzelner Detektor benötigt. HLI hat die Eigenschaft unter bestimmten Umständen Rauschen effizient zu unterdrücken, was in einer zuverlässigeren Schätzung der Lebenszeiten resultiert. Die Charakteristiken dieser Methode als auch Vorteile und Nachteile werden kurz präsentiert.

Contents

Abstract	iii
Zusammenfassung	v
1 Introduction	1
2 Fluorescence	5
2.1 History of fluorescence	5
2.2 The physics of fluorescence	6
2.2.1 Excitation and de-excitation pathways	6
2.2.2 Excited state lifetime	7
2.2.3 Quantum yield	8
2.2.4 Molecular absorption cross-section	9
3 Fluorescence lifetime spectroscopy and imaging	11
3.1 Measurement techniques	12
3.1.1 Time correlated single photon counting	12
3.1.2 Phase fluorometry	13
3.2 Fluorescence lifetime imaging	14
4 Fluorescence correlation spectroscopy (FCS)	15
4.1 History of FCS	16
4.2 General aspects of FCS	17
4.3 FCS for translational diffusion	20
5 Total internal reflection fluorescence	25
5.1 Total internal reflection (TIR)	25
5.2 TIRFM	28
5.2.1 Background	30
5.2.2 Collection efficiency	30
5.2.3 Handling	31
6 Objective-type TIR-FCS	33
6.1 Motivation	33
6.2 Description of the setup	34
6.2.1 Fluorescence excitation	35
6.2.2 Fluorescence detection	36
6.2.3 Background suppression	38
6.2.4 Molecule detection efficiency	39

7	Diffusion studies	43
7.1	Derivation of the autocorrelation function for diffusion	43
7.2	Measurements and data analysis	44
8	Binding studies	49
8.1	The autocorrelation function for binding	49
8.2	Measurements and data analysis	56
8.2.1	Adsorption and desorption	56
8.2.2	Binding to a single binding site	58
9	Enzymatic activity of horseradish peroxidase	61
9.1	Motivation	61
9.2	Horseradish peroxidase	62
9.3	Materials and Methods	63
9.3.1	Optical setup	63
9.3.2	Chemicals	64
9.3.3	Surface preparation	64
9.3.4	Data acquisition and analysis	64
9.4	Results	64
9.4.1	Activity of horseradish peroxidase in solution	64
9.4.2	Measurements on the substrate in the absence of the enzyme	65
9.4.3	Measurements on the immobilized enzyme	65
9.4.4	Control Measurements	67
10	Conclusions and outlook	69
	Acknowledgements	79
	Publications	81
	Curriculum vitae	115

Chapter 1

Introduction

The utilization of fluorescence spectroscopy and imaging in life science has a long history. In the course of time it became an integral part of cellular biology, molecular biology and medicine. Several techniques emerged that harness different characteristics of fluorescence, including e.g. fluorescence lifetime spectroscopy [1, 2] and imaging microscopy (FLIM) [3], different relaxation techniques as fluorescence recovery after photobleaching (FRAP) [4], fluorescence correlation spectroscopy (FCS) [5], further fluorescence distribution analysis (FIDA) [6, 7, 8], fluorescence resonance energy transfer (FRET) [9] and many others. The sensitivity of fluorescence based methods increased continually with progresses made in microscopy and detector technology. A particularly important development step that opened a brand new field of possible applications was the first successful observation of individual fluorophores in a biologically relevant environment in the late 1980s [10] (see also [11, 12, 13]). This step was the foundation stone of a new domain in fluorescence spectroscopy: *single molecule detection* (SMD) [13]. Since then several research groups showed how the observation of individual fluorescently labeled proteins can lead to amazing insights into the mechanisms of life on a nanometer scale. Many details about the functioning of molecular motors, cellular trafficking and signaling could be revealed by SMD (for an extensive overview see for instance [13, 14]).

A very interesting representative of fluorescence techniques featuring single-molecule sensitivity is FCS [15, 16, 17, 18, 5, 19]. FCS is a special case of *relaxation analysis*. That is to say, kinetic parameters of a molecular system are inferred by observing how the system returns back to equilibrium after a small perturbation. FCS utilizes deviations from equilibrium that are due to thermal noise. In contrast to most fluorescence based techniques the measured parameter is not the fluorescence intensity itself but small deviations of the fluorescence signal from the mean value. In principle the kinetics of all molecular processes that manifest themselves as a variation of the fluorescence signal is accessible by this technique. For instance it is rather straightforward to measure diffusion times and concentrations of fluorescent molecules as Brownian motion leads to concentration fluctuations in a small observation volume, which in turn causes measurable intensity fluctuations. Mean frequencies at which fluctuations occur as well as their mean strength are conveniently obtained by calculating the temporal autocorrelation of the fluctuating signal.

Classical FCS as most of the very sensitive fluorescence based techniques is based on *confocal microscopy* [20, 21]. Fluorescence is detected from a minute observation volume realized by exciting fluorescence inside the tight focus of a laser beam and using in addition a pinhole in front of the detector, which rejects out-of-focus light. A small volume, which is in the case of confocal FCS typically less than 1 fl assures firstly that at each instant only few molecules reside in the observation volume and secondly that background from e.g. scattered light is low.

The framework of the presented work was the development of existing fluorescence based

techniques towards higher sensitivity. Part of preliminary research was e.g. the investigation of a novel way to perform FLIM based on a multiplexing approach (see paper I). In the course of this thesis an alternative to confocal FCS was developed and characterized, which uses total internal reflection (TIR) in order to excite fluorescence in the proximity of a glass surface. Here, a laser beam propagating in a glass slide and incident at the glass-sample interface at an angle that exceeds the critical angle is totally reflected at the interface and generates an evanescent field at the surface that vanishes exponentially with distance z to the surface. Therefore, only fluorophores very close to the surface ($z < 100$ nm) are efficiently excited. The high confinement of the excitation field and hence observation volume leads to reduced background and artifacts if the investigated molecular system is confined to the surface.

Using total internal reflection in order to excite fluorescence proved already useful in microscopy; in fact, this method became a technique on its own called total internal reflection microscopy (TIRFM) [22, 23, 24, 25]. This technique of fluorescence excitation was used in very early FCS experiments [26, 27] as it was the natural way to confine the observation volume before the adaption of the confocal principle from microscopy. In these experiments the evanescent field was generated by means of total internal reflection at the surface of a prism, typically above the objective of an inverted microscope, used to collect fluorescence.

In this thesis a different approach is proposed, which consists in adapting an objective-type TIRFM [28, 23, 25] configuration for measuring FCS. In objective-type TIRFM (or prismless TIRFM), fluorescence is excited and collected by means of an epi-illumination configuration [20], which means that light falls on the sample from the observation side. This approach offers several advantages compared to the 'prism-type' configuration, most important the light collection efficiency is considerably increased [29]. In the course of the present thesis the high performance of objective-type TIR-FCS in terms of collection efficiency and signal-to-background ratio could be shown in different experiments. The method was successfully applied to measure diffusion times of fluorophores diffusing above a microscope cover slide. Further it was shown that the proposed technique can be used to investigate binding. The high count rates per molecule and signal-to-background ratio (~ 35) allowed for measuring binding rates of individual molecules binding to a single, localized binding site. In order to analyze FCS data analytical models for the autocorrelation function were derived. This was done for free diffusion as well as for combined diffusion and most important binding to a single, localized receptor. The models were successfully applied to analyze FCS data for free diffusion as well as for binding.

Single molecule techniques allow to answer questions that cannot be addressed by measurements on an ensemble of molecules. Numerous interesting questions relate to enzymology. Most enzymes are proteins and after translation, before they become functional, they have to fold into a particular conformation. Protein folding is a well investigated but very complex process. Many pathways on a rough energy landscape lead to different final structures. Thermodynamically induced conformational changes in already folded enzymes are less investigated although it is known from theory and several experiments that these changes are closely related to the function of enzymes [30, 31].

Motivated by results obtained with confocal FCS by L. Edman et al. [32] we studied the applicability of objective-type TIR-FCS to investigate conformational changes in single horseradish peroxidase molecules. Horseradish peroxidase is capable of catalyzing the oxidation of the non-fluorescent substrate dihydrorhodamine 6G. Since the product (rhodamine 6G) is highly fluorescent, product formation leads to intensity fluctuations, which can be investigated by means of FCS. Presented experiments show the advantages and actual limitations of the approach.

This thesis is organized as follows:

Chapters 2 to 5 give an overview on fluorescence and fluorescence based techniques related to the presented work. Results are presented in three published papers found in the annexe.

Supplementary material and detailed discussions are presented in chapters 6 to 9.

Chapter 2 gives an overview on the phenomenon fluorescence. Physical principles as well as historical facts are discussed. Chapter 3 is devoted to fluorescence lifetime spectroscopy for the purpose of an introduction to the work presented in paper I. Chapter 4 is an introduction to FCS. Technical aspects and application fields are discussed. For later reference a derivation of the autocorrelation function for diffusion is presented. Chapter 5 discusses several aspects of evanescent wave excitation. Objective-type TIR-FCS is introduced in chapter 6. The method is thoroughly characterized on a theoretical basis. In chapter 7 the autocorrelation function for diffusion is derived and experimental results are discussed. Results serve as means for a characterization of the setup. The derivation of the autocorrelation function for the case of diffusion combined with binding of ligands to a single, localized receptor is presented in chapter 8. The derived function constitutes a new and important result, which makes quantitative investigations of single molecule binding possible. Measurement results for dyes adsorbing to a microscope slide as well as binding to a single localized binding site are presented and discussed. The experiments on horseradish peroxidase are presented in chapter 9. Limitations and sources of artifacts are discussed and solutions are proposed. The work is summarized in the conclusions (chapter 10).

Chapter 2

Fluorescence

This thesis deals with fluorescence spectroscopy whose underlying basic physical principle is photoluminescence and in particular fluorescence. The present chapter is intended to introduce the phenomenon of fluorescence. In the following several aspects of general interest, important terms, and physical mechanisms, which are crucial for the understanding of subsequent chapters will be presented.

2.1 History of fluorescence

Fluorescence is a *luminescence* (from Latin *lumen* = light) phenomenon that is to say, a phenomenon of light emission, which is not solely conditioned by the rise in temperature, according to the original definition and introduction of the term by the physicist and science historian Eilhardt Wiedemann in 1888. In other words, the term luminescence denotes all mechanisms of light emission that are not attributed to incandescence.¹ This definition covers a large variety of different phenomena, which are categorized according to the mode of excitation. Some examples are [33]: Photoluminescence (including fluorescence, phosphorescence and delayed fluorescence), sonoluminescence, bioluminescence, chemiluminescence, radioluminescence and thermoluminescence. *Photoluminescence* covers all phenomena where molecules reach an electronic excited state by absorption of a photon and emit another photon, in general at a larger wavelength.

The oldest documented observation of photoluminescence we know, relates to fluorescence. In 1565 the Spanish physician Nicolas Monardes discovered that fluorescence is emitted from the infusion of the wood *Lignum Nephriticum*. Among others Isaac Newton investigated the light emission of the infusion from *Lignum Nephriticum*, but the observed phenomenon was not understood at this time. Another important discovery was made in the beginning of the 17th century by the Italian cobbler and alchemist Vincenzo Cascariolo. He reported the observation of phosphorescence after calcination of a mineral, which became known under the name *Bolognian phosphor*. The name *phosphor* comes from the Greek *phōsphóros*, meaning 'which bears light', or 'who brings light' (in Latin: Lucifer). The same name was assigned to the phosphorescent chemical element discovered in the middle of the 17th century by Hennig Brandt. George Gabriel Stokes investigated the emission of light by quinine sulfate in solution after the excitation with ultraviolet light (published in 1852). Shortly later, he introduced the name fluorescence for the observed phenomenon. The term fluorescence is derived from the mineral fluorspar, which was known to emit light after excitation in the UV. Interestingly, fluorescence of fluorspar is due to impurities (europium, yttrium and dysprosium), which are often found in this mineral

¹*Incandescence* is the emission of electromagnetic radiation of a hot body due to its high temperature. Typically in the infrared and visible region of the electromagnetic spectrum.

[33]. By illuminating quinine sulfate with different wavelengths using a prism, and the sun as a light source Stokes recognized that the emitted fluorescence has a longer wavelength than the incident light. This shift in wavelength is today known as Stokes shift. In fact, Stokes was not the first one who stated this effect. Already some years before, the French physicist Alexandre-Edmond Becquerel² reported the wavelength shift for light emitted by calcium sulfide, which is phosphorescent.

In the beginning of the 20th century a lot of progress was made in the understanding of photoluminescence, which paved the way for the development of a huge number of fluorescence based applications in many different domains. Today, fluorescence is gaining increasing popularity as a tool for imaging and spectroscopic techniques in life-science, especially in medicine and molecular biology, but also in material and chemical science. In combination with basic microscopic imaging it gives us information about structure, when used with techniques like single molecule tracking [34, 35], fluorescence resonance energy transfer (see e.g. [36] and references cited therein) or FCS [5, 19, 37], function can be investigated. Applications include among others staining of samples for microscopy, DNA sequencing [38], DNA detection [33], microarrays [39], probing of micro-environments [33], single molecule detection and tracking in cells, and investigation of molecular motors and enzymes [40, 41].

2.2 The physics of fluorescence

2.2.1 Excitation and de-excitation pathways

Fluorophores are excited by absorption of a single photon which leads to a transition of an electron from its ground state to a state of higher energy, the excited state. The detailed mechanisms of this process are most conveniently illustrated in the *Perrin-Jablonski diagram* (Fig. 2.1). The

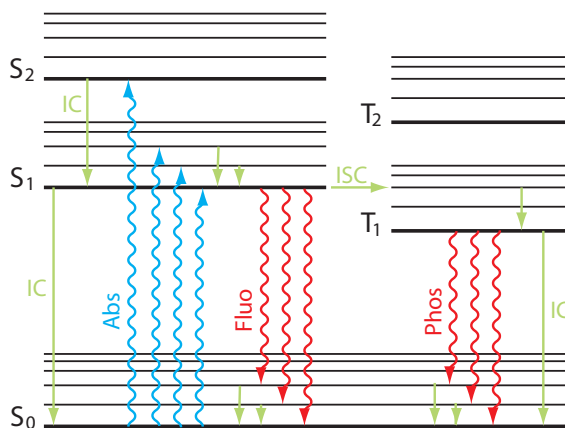


Figure 2.1: Perrin-Jablonski diagram. Electronic (thick horizontal lines) and associated vibrational energy levels (thin horizontal lines) and the most important excitation and de-excitation pathways are shown. Wavy lines denote absorption and radiative pathways. Straight lines with arrow-heads represent possible non-radiative pathways. Abs: absorption; Fluo: fluorescence; Phos: phosphorescence; IC: internal conversion; ISC: intersystem crossing.

diagram represents the structure of the energy levels and different excitation and de-excitation pathways. In general the excitation is a transition from one singlet state to another singlet state, i.e. the promoted electron of a pair of electrons does not change its spin and the spin

²Alexandre-Edmond Becquerel is the father of the famous physicist Antoine Henri Becquerel who discovered radioactivity in 1896. He got the Nobel price in physics together with Marie and Pierre Curie in 1903.

quantum number, $S = \sum s_i$, with $s_i = +\frac{1}{2}$ or $-\frac{1}{2}$, remains zero³. The term *singlet* refers to the multiplicity of the total spin quantum number, $M = 2S + 1$ (number of spin states with equal energy). For singlet states, the ground state is denoted S_0 and S_1, S_2, S_3, \dots denote the excited states. Once in the excited state, the molecule has different pathways to return to its ground state including fluorescence emission, which is a transition between S_1 and S_0 accompanied by the emission of one photon. Other de-excitation mechanisms are intersystem crossing, internal conversion, intramolecular charge transfer, conformational change, and pathways due to intermolecular interactions such as electron transfer, proton transfer, energy transfer, excimer formation, exciplex formation, photochemical transformation [33]. Most of the cited de-excitation pathways are *non-radiative*, which means they lead to the ground state without the emission of a photon. De-excitation via intersystem crossing is of particular interest. This pathway does not lead directly from S_1 to the ground state but to an excited *triplet state* (multiplicity of the total spin quantum number $M = 3$), T_1 . The transition from the singlet to the triplet state is accompanied by a change of spin of the promoted electron. The probability for this transition is much lower than for fluorescence because the change of spin is quantum mechanically forbidden if only spin-states are considered [36]. Nevertheless, there is always a weak interaction of the wavefunctions of different multiplicities making a transition between singlet and triplet states possible. The responsible effect is called *spin-orbit coupling* and can be understood within the framework of the Bohr atom-model as an interaction between the magnetic fields caused by the orbital movement and the spin of the electrons, respectively [36]. Because this interaction is small, the excited triplet state is long-lived compared to the corresponding excited singlet state. From the triplet state the molecule will either reach directly S_0 by emission of a photon (*phosphorescence*) or by *delayed fluorescence* via the state S_1 after thermally induced reverse intersystem crossing, or by nonradiative internal conversion. The emitted photon in the case of phosphorescence has a longer wavelength compared to fluorescence because the triplet state has lower energy than the singlet state of the same configuration, according to Hund's law [33].

Fluorescent molecules in solution exhibit rather broad, continuous absorption and emission spectra. In fact, with each electronic state there is a multitude of energy levels associated. The different energy levels correspond to different vibrational states of the molecules forming apparently continuous bands. At room temperature most of the molecules are at the vibrational ground state. Absorption of a photon is normally accompanied by a transition to higher vibrational states. Vibrational relaxation causes a de-excitation towards the vibrational ground-state, which is a rather fast process ($\sim 10^{-13}$ s – 10^{-11} s) compared to the typical excited state lifetime [33]. After this relaxation the radiative transition takes the molecule from the vibrational ground state of S_1 , to S_0 . During vibrational relaxation energy is dissipated in form of heat, which explains that the photon emitted afterward carries less energy than the absorbed photon. This effect is known as Stokes shift.⁴ The fact that the relaxation to the vibrational ground state is a fast process compared to the de-excitation to S_0 implies further that the emission spectrum is independent from the excitation wavelength.

2.2.2 Excited state lifetime

After excitation and vibrational relaxation the molecule does not instantly reach its electronic ground state. The relaxation to S_0 takes place after some random time delay t which is expo-

³Some exceptions exist where the ground state of the fluorescent species is not a singlet state.

⁴Rather rarely a contrary effect is observed, that is to say the emission of a photon with higher energy compared to the absorbed photon. In fact, at room temperature a fraction of (not excited) molecules is found to occupy higher vibrational states; the occupancy of different energy levels is governed by the Boltzmann distribution. If the molecule is in a higher vibrational state when excited an anti-Stokes shift to lower wavelengths may occur. For this reason, the emission and excitation spectra of fluorophores in solution are partially overlapping.

nentially distributed. The mean time delay τ_L , also called the *excited state lifetime* or simply *lifetime* depends on the individual rate constants k_i of the different de-excitation pathways and is given by the formula [36]

$$\tau_L = \frac{1}{\sum_i k_i}. \quad (2.1)$$

The rate constants k_i are in general not invariable parameters associated with a particular fluorophore but dependent on its micro-environment. Factors that influence the decay rates are refractive index, pH [42, 43], oxygen concentration [44], ion-concentration [45] and temperature [36]. The strong lifetime dependence on the before mentioned factors, observed for several fluorescent compounds, makes fluorescence a useful tool to probe changes in the micro-environment by measuring the excited state lifetime. Furthermore, the lifetime may be used as a means to distinguish different dye labels. A differentiation based on the emission and excitation wavelengths alone is often insufficient, because the broad emission or excitation spectra of usable dyes are often overlapping. Combining both, spectral and lifetime information can considerably increase the sensitivity for differentiation of molecular species. Different techniques exist for measuring the excited state lifetime. Most important is the frequency modulation technique [36] and time correlated single photon counting (TCSPC) [46]. The latter consists in exciting fluorescence by means of a short laser pulse and measuring the delay between excitation and emission of a photon.

2.2.3 Quantum yield

Related to the de-excitation rates is the brightness of the fluorophore, or more precisely the *fluorescence quantum yield*, Φ_F . This quantity is defined as the probability that the fluorophore returns to the ground state via fluorescence emission [33]. In other words it is the ratio of excited molecules to emitted photons due to fluorescence. The fluorescence quantum yield depends on the rate constants [33]:

$$\Phi_F = \frac{k_F}{\sum_i k_i}, \quad (2.2)$$

where k_F is the rate constant of fluorescence transition. The relation between rates and quantum yields for phosphorescence, internal conversion, etc. are given by analogue formula. As the rates k_i are dependent on the fluorophores micro-environment the same holds for the fluorescence quantum yield; hence with Φ_F one has another observable at hand that can be monitored to study micro-environments. This dependency of Φ_F is used in *fluorescence resonance energy transfer* (FRET) to measure distances between two fluorophores, a *donor* and an *acceptor* [9]. If an acceptor is very close (a few nanometers) to an excited donor, the donor wont undergo a fluorescence transition, its fluorescence will be *quenched*. The energy difference between excited and ground state is instead transfered to the acceptor which causes the latter to emit fluorescence. The acceptor emits fluorescence at a longer wavelength than the donor. Since the efficiency of FRET is dependend on the distance between the two molecules one can determine the distance by measuring the relative fluorescence emission of acceptor and donor. Less complex applications include for example DNA detection; for some fluorophores Φ_F is increased upon binding to DNA.⁵

⁵In the first FCS experiments D. Magde, W.W. Webb and E. Elson investigated the binding of the small intercalating dye ethidium bromide (EtBr) to DNA [15]. When EtBr binds to DNA, its fluorescence quantum yield increases. By investigating the fluorescence fluctuations associated with binding and de-binding, they were able to determine the chemical reaction rates.

2.2.4 Molecular absorption cross-section

Another important parameter that characterizes fluorescent molecules is the efficiency of light absorbance, which is dependent on the wavelength λ . It is most conveniently expressed by the *molecular absorption cross-section* $\sigma(\lambda)$, which is related to the fraction of intensity absorbed by a thin layer [33]:

$$\frac{dI}{I} = \sigma(\lambda) N_A C dl. \quad (2.3)$$

Here, I is the incident intensity, dI the intensity absorbed by a layer of thickness dl , N_A is Avogadro's constant, and C the concentration of the absorbing species. Unlike the quantum yield, this quantity is in general independent of the fluorophore's (chemical) environment. Integration of Eq. 2.3 yields the Beer-Lambert law, which states that the intensity decreases exponentially when light traverses a homogeneous, absorbing medium

$$I(l) = I_0 e^{-\sigma N_A C l}. \quad (2.4)$$

Chapter 3

Fluorescence lifetime spectroscopy and imaging

In life science fluorescence is employed as a tool for detection, discrimination and sensing. In all three application fields we rely on the possibility to access characteristic attributes of the fluorescence signal. Detection requires that we are able to distinguish a fluorescence signal from background (e.g. spurious fluorescence from impurities or scattered light); discrimination and sensing require that we are able to distinguish between different fluorophores and microenvironments, respectively. The measurable attributes that are available are wavelength, brightness, position, orientation (of the dipole moment) and last but not least fluorescence lifetime. The most important attributes in this context are the first three; e.g. fluorescence microscopy, single molecule tracking, FIDA rely on the possibility to precisely determine these observables.

An important driving force for developments in fluorescence spectroscopy is DNA sequencing. Today, the most important sequencing technology is still gel-electrophoresis. The throughput of this method is rather slow, typically a few bases per second [47], which implies that the sequencing of the human genome (3×10^9 bases) requires several years. The method requires further a quite large amount of genetic material and therefore the application of amplification techniques as polymerase chain reaction (PCR). A considerable amount of work is invested in order to make sequencing faster and to decrease the needed amount of DNA. A lot of the efforts aim on the goal to obtain sequence information from one single DNA molecule. A very interesting approach was proposed by Jett et al. [48]. The basic idea consists in immobilizing a single DNA molecule whose bases are labeled with different fluorophores. An exonuclease¹ enzyme cuts single labeled bases from an end of the DNA strand. The bases are transported in a microfluidic device through a detection volume, where fluorescence is excited and detected. The sequence may be obtained by labeling the bases with different, distinguishable markers.

This is one example where a reliable discrimination between different fluorophores is crucial. The task is made difficult by the fact that the number of photons that can be detected from one fluorophore in the short time-laps between entering and leaving the detection volume is limited. Discrimination by means of fluorescence spectra alone can be insufficient in this case. Fluorescence dyes have very broad spectra, which for two usable dyes will almost always have a considerable overlap. The discrimination may be improved by measuring the fluorescence lifetime of the dyes. Using the lifetimes rather than the spectra for the purpose of discrimination has several advantages. If the lifetime is the only parameter to be accessed, only one excitation source and one detection channel is needed. If the lifetime measurement is performed by means

¹*Exonucleases* are enzymes that cleave nucleotides, one at a time, from a polynucleotide chain. Exonucleases proceed from an end of a polynucleotide chain, as opposed to *endonucleases*, which cleave bonds within the chain.

of time correlated single photon counting, time gating may be used to decrease the influence of background. Moreover, if the discrimination is based on the two parameters wavelength and lifetime, this may considerably decrease the number of wrong identifications.

Fluorescence lifetime is further harnessed to sense microenvironments [49, 33]. As pointed out in the preceding chapter 2, the fluorescence lifetime is not an invariant property of a molecule but depends on several parameters e.g. the refractive index of the ambient medium, its pH [42, 43], concentrations of different ions [45], oxygen concentration [44] etc.

3.1 Measurement techniques

The time a fluorescent molecule resides in its excited state S_1 is not a constant but a random variable with exponential probability density function. Two kinds of measurements exist to determine the average excited state or fluorescence lifetime, frequency domain and time domain [36, 46, 33]. In frequency domain measurements, the excitation intensity is modulated by a sine function. The fluorescence intensity is also modulated but shifted in phase. Measuring the phase shift allows to determine the fluorescence lifetime. In time domain measurements, the delay between a short illumination pulse and fluorescence emission is measured directly. Time domain measurements are very sensitive and can give accurate results for only a few hundred detected photons [50, 51]. The two most common techniques, time correlated single photon counting (TCSPC) [46] and phase fluorometry [33] will be shortly discussed in the following.

3.1.1 Time correlated single photon counting

This method is based on measuring the delay between each detected photon and the preceding excitation pulse. Fluorescence is excited by a train of light-pulses, ideally shorter than the expected fluorescence lifetime, which is in the order of one to several nanoseconds. Excitation may be realized by means of a flash lamp or a mode locked laser. A very convenient and today relatively inexpensive possibility are diode lasers, which generate pulses shorter than 100 ps at repetition rates up to almost 100 MHz. A single photon avalanche diode (SPAD) or photomultiplier tube (PMT) is used to detect fluorescence emission. Each detection event triggers a voltage ramp in a time to amplitude converter (TAC). A stop signal is triggered by the succeeding laser pulse. The voltage is converted into an address by means of an analogue to digital converter and a count number incremented by one at the corresponding address. In this way a histogram builds up, which can be analyzed using different fitting algorithms. The number of detected photons needed depends evidently on the accuracy required for lifetime determination. The accuracy depends on factors as background level, the width of the instrument response function, resolution of the histogram and the character of the fluorescence decay. In the simplest case the probability density of the delay between excitation and emission is a single exponential function. If e.g. more than one fluorophore is present the probability density becomes a sum of several exponential functions and analyzing the data may become extremely difficult. The histogram is never a simple exponential function but shows besides the characteristics of the fluorescence decay the characteristics of the detecting system. In fact, the probability density that describes the histogram is a convolution between the fluorescence decay (e.g. single exponential function) with the impulse-response function of the measurement system. If the width of the impulse-response is large or if the measurement has to be very precise, the data has to be deconvolved before a fitting algorithm can be applied.

The start signal for the TAC is triggered by the detection of a photon and the stop signal by the succeeding excitation pulse. The reason to proceed this way and not the other way round, is to generate fewer voltage ramps. After each voltage ramp, the system experiences a certain

dead-time in which the electronic finds back to its ground state. Triggering the start signal by a detection event ensures that the accumulated dead time of the system is minimal.

TCSPC features outstanding sensitivity and can be applied on very low light levels. There exists however an upper threshold for the intensity that should not be exceeded, typically beyond 10 MHz photon count rate. This is because the average number of detected photons per second should not exceed one per ten excitation pulses. If it does, the probability of detecting two photons in the time-window between two subsequent excitation pulses is not negligible any more. The system will detect only the first photon which leads to a distortion of the histogram; it will appear narrower.

It is worth noting that besides measuring the lifetime TCSPC can be used to suppress background. Unlike fluorescence, Raman or Rayleigh scattered light appears simultaneously with the excitation pulse. By considering only photons that arrive after the excitation pulse has died away, this background can be completely suppressed [3].

3.1.2 Phase fluorometry

Here, the sample is excited by a fast varying sinusoidally modulated light source. In a simplified manner we may write the detected fluorescence intensity, $I(t)$, as a convolution between the probability density for a photon to be emitted a certain time t after excitation, $p(t)$, and the excitation intensity $\mathcal{I}(t)$ [33]

$$I(t) = \kappa p(t) * \mathcal{I}(t) \equiv \kappa \int_{-\infty}^t p(t-t') \mathcal{I}(t') dt'. \quad (3.1)$$

The constant κ accounts for excitation efficiency, quantum yield and light losses in the detection path. The excitation intensity as a function of time is

$$\mathcal{I}(t) = \mathcal{I}_0 (1 + m_0 e^{i\omega t}), \quad (3.2)$$

with m_0 denoting the modulation depth. The detected fluorescence intensity varies with the same frequency but it is demodulated and its phase is shifted with respect to $\mathcal{I}(t)$. With Eq. 3.2, Eq. 3.1 and $u = t - t'$ we get

$$I(t) = \kappa \mathcal{I}_0 \left(1 + m_0 e^{i\omega t} \int_0^\infty p(u) e^{-i\omega u} du \right). \quad (3.3)$$

This can be written as

$$I(t) = \kappa \mathcal{I}_0 \left(1 + m e^{i\omega t - i\phi} \right) \quad (3.4)$$

with

$$M e^{-i\phi} = \int_0^\infty p(t) e^{-i\omega t} dt. \quad (3.5)$$

We introduced the relative modulation depth, $M = m/m_0$. In the case of a single exponential decay, that is to say $p(t) = \tau^{-1} \exp(-t/\tau)$ for $t \geq 0$ we derive

$$\tau = \frac{1}{\omega} \tan \phi \quad \text{and} \quad (3.6)$$

$$\tau = \frac{1}{\omega M} \sqrt{1 - M^2}. \quad (3.7)$$

If $p(t)$ is a sum of several exponential functions, the different lifetimes and fractions can in principal be obtained by measuring for different modulation frequencies, ω . For frequency domain measurements, no deconvolution is required. This can be a certain advantage, because deconvolution is quite a sensible task and can introduce additional noise [52].

3.2 Fluorescence lifetime imaging

Fluorescence lifetime as a sensor for microenvironments unfolds its whole potential when the lifetime information is combined with information on position, which leads to fluorescence lifetime imaging microscopy (FLIM) [3, 53]. With FLIM e.g. quantitative images of pH in cells could be obtained [54]. FLIM was further successfully used to discriminate different types of tissue [55], with an application in breast [56] and skin-tumor detection [57].

Two approaches are commonly used to obtain (microscopic) fluorescence lifetime images. Scanning confocal microscopy can be combined with time domain or frequency domain techniques to perform FLIM [58]. Alternatively a CCD camera in combination with a gated microchannel plate (FWHM) can be used [59, 60]. In the latter case a stroboscopic technique² is applied to obtain fluorescence decay histograms.

In the course of this doctoral thesis a new method was developed that is based on multiplexed imaging and TCSPC. A short introduction to this method called *Hadamard lifetime imaging* is provided in the following; for a detailed description of the proposed technique see paper I. The basic idea consists in illuminating the whole sample and masking the fluorescence emission, such that a subset of pixels is imaged onto a single point detector. This is achieved by placing a mask at an appropriate plane in the detection path. A mask can be realized by means of a micromirror device or liquid crystal array placed at an intermediate image plane. The mask is then imaged onto the detector e.g. a photomultiplier tube. Alternatively, the mask may be placed in an appropriate plane in the illumination path to create an image on the sample. A sequence of histograms for different well defined masks is recorded by means of TCSPC (or an alternative technique). In this way one obtains a set of data, which allows to derive a fluorescence lifetime image by applying a linear transformation to the data set.

If a sequence of masks defined by e.g. Hadamard matrices [61] is used, this approach may lead to a higher signal-to-noise ratio and more accuracy in parameter estimation compared to confocal scanning. A detailed investigation of this effect by means of Monte Carlo simulations is provided in paper I. The simulations show that an increase in the signal-to-noise ratio with respect to scanning may be expected if the noise is mainly due to detector dark counts. However, the error in parameter estimation will be higher for Hadamard lifetime imaging if the main noise source is statistical noise. But most important, the proposed technique may constitute the base of a low cost system; no intensified camera, no scanning stage are necessary and TCSPC may be replaced by the stroboscopic technique.

²The *stroboscopic technique* consists in exciting the sample by a train of light pulses. A photomultiplier is gated by a voltage pulse with the result that fluorescence is collected only within a small, with respect to the excitation pulse precisely delayed time window. The gating is synchronized with the light source by means of a master clock. Fluorescence intensity as a function of time is obtained by measuring for different time delays after excitation.

Chapter 4

Fluorescence correlation spectroscopy (FCS)

The basic idea of *fluorescence correlation spectroscopy* (FCS) consists in investigating thermal fluctuations to gain insight in the dynamic and kinetic properties of a molecular system at equilibrium [15, 16, 17, 18, 5, 19]. FCS is based on the so-called *fluctuation-dissipation theorem* of statistical physics, which states that the fluctuation properties of a system and its response to an external perturbation are closely related [62, 63]. This characteristic of molecular systems gave rise to several techniques used to study equilibrium statistics by investigating relaxation to equilibrium after a small perturbation.

One popular technique relying on external perturbation is *fluorescence recovery after photobleaching* (FRAP) (sometimes also called fluorescence photobleaching recovery or short, FPR), which can be applied to study binding kinetics and diffusion [4, 64, 65, 26]. The technique consists in bleaching the fluorophores inside a small observation volume by applying a short and intense light pulse. The term *observation volume* means loosely speaking a generally very small volume in which we measure the value of our observable. The measured value consists of some kind of weighted average taken over the whole observation volume. In FRAP as well as in FCS, the observable is the fluorescence intensity emitted from this volume. After photobleaching, the deviation from equilibrium consisting in a local absence of fluorescent molecules is relaxed by Brownian motion or other transport mechanism. By observing the increase in fluorescence intensity emitted from the observation volume one can determine parameters describing the molecular dynamics at equilibrium. In case of Brownian motion, the diffusion coefficient of the fluorescent or fluorescently labeled species may be obtained in this way. If the molecules undergo some binding to immobile or slowly diffusing receptors, information about the binding kinetics can further be obtained. The method was e.g. successfully applied to monitor membrane trafficking in living cells [4].

Another perturbation method worth mentioning is the temperature-jump method developed by M. Eigen [66]. Here, laser pulse absorption or capacitor discharge leads to a fast localized increase in temperature. The relaxation dynamics is for instance accessed by observing a change in the UV absorption.

FCS is similar in the sense that it is based on the fluctuation-dissipation theorem. However, FCS does not perturb the studied system because it does not cause any deviation from the equilibrium state. In fact this technique harnesses the deviations from equilibrium that occur naturally in the form of thermal noise. On the molecular level, equilibrium states are highly dynamic and the smaller the observed system the higher are the fluctuations that are observable by, e.g. FCS. The fluctuating parameter of interest is frequently a local concentration of some

molecular species. The concentration or more precisely, the number of some particular molecules in the observation volume can be coupled to a fluorescence signal by labeling the molecules of interest with a fluorescent tag. When studying the rather simple case of diffusion, Brownian motion will cause variations in the number of fluorescently labeled molecules residing in the observation volume. This translates into a variation of the intensity emitted from this volume element. The intensity, $I(t)$, is detected as a function of time and the autocorrelation of the deviation from the mean concentration is calculated. Among other parameters the *diffusion time* which is approximately the average time a molecule stays inside the observation volume and the number of molecules in the volume can be obtained by fitting an appropriate model to the intensity fluctuation autocorrelation.

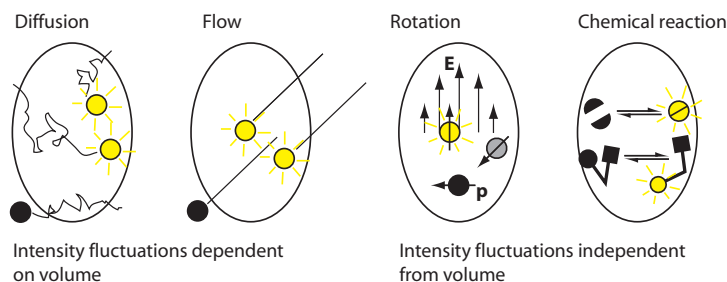


Figure 4.1: This scheme illustrates how molecular fluctuations of different kind are coupled to intensity fluctuations (from [33]). Diffusion and flow change the number of fluorescently tagged molecules inside the observation volume. Rotation can be studied by selectively exciting molecules with a particular orientation using polarized light. Binding kinetics and conformational dynamics can be investigated if these introduce changes in the fluorescence quantum yield of an attached fluorophore.

FCS is not limited to measure parameters related to diffusion (see Fig. 4.1). Another parameter that can be accessed via a fluorescence signal is the orientation of fluorophores with respect to the polarization of the excitation light field [67]. The rotation of fluorophores in the polarized light field gives rise to intensity fluctuations. From their correlation the rotational diffusion time can be inferred. Furthermore FCS can be used to study conformational changes of biomolecules by labeling with a dye that is quenched in one particular configuration [68, 69]. Binding kinetics can be studied by FCS if the diffusion constant of the labeled ligand or the fluorescence quantum yield changes upon binding [70, 71].

4.1 History of FCS

FCS was invented and introduced by D. Magde, E. Elson and W.W. Webb in 1972 [15]. The technique was applied to study the binding of ethidium bromide (EtBr) to double-stranded DNA. When the small fluorescent molecule EtBr binds to DNA, or more precisely, when it is inserted between DNA bases its fluorescence quantum yield increases dramatically. Hence every binding or de-binding event as well as diffusion inside the observation volume translates into a fluctuation of intensity. In their experiment, Magde and Webb used laser excitation of 6 kW cm^{-2} at 514 nm . A parabolic mirror was used to collect the fluorescence and to image the observation volume onto a photomultiplier. Today, dichroic mirrors and interference filters can be conveniently used to efficiently separate the excitation light from the fluorescence light. In 1972 a solution of $\text{K}_2\text{Cr}_2\text{O}_7$ was used to filter the scattered excitation light. The observation volume was several orders of magnitude larger compared to what became standard today. The resulting diffusion time for the DNA-fluorophore complex was about 10-100 ms, slow enough to observe the binding kinetics of DNA and EtBr molecules during their random walk through the

observation volume. Despite the comparable simple technology they had at hand, Magde et al. were able to derive the diffusion coefficient of the DNA strand and the rate constants in this pioneering experiment.

Although FCS and the underlying theory existed already in the early 70's the advent of this method started only in the early 90's with the adaption of the confocal principle [72]. The concept, borrowed from microscopy, which consists in using a pinhole at an intermediate image plane in the detection path, resulted in a dramatic decrease of the observation volume to a size of about $0.2 - 10 \text{ fl}$. A small size is important not only in order to get high spatial resolution, which in confocal microscopy and FCS is limited by diffraction, but also to get a high signal to background ratio. By decreasing the size of the volume, the background from scattered light will decrease but the relative amplitude of the intensity fluctuation will increase. For these reasons, a small volume is of uttermost importance when conducting measurements on the single molecule level.

Since the early 90's, the number of publications on FCS, containing the term 'fluorescence correlation spectroscopy' in title, abstract or key-word list was continually increasing and reached a number of 167 in 2004. The number of applications in life science grew accordingly. So far FCS was used e.g. for drug screening, the investigation of conformational changes in biomolecules, measuring diffusion inside cells and on the cell membrane, adsorption kinetics and enzyme kinetics (for a review see [37]).

4.2 General aspects of FCS

This section is intended to provide some information on more technical aspects of FCS for later reference. A scheme of a standard setup for confocal FCS is shown in Fig. 4.2. The optical

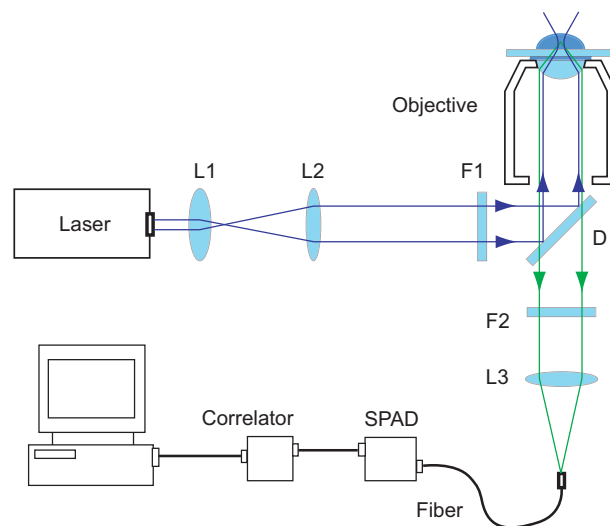


Figure 4.2: Scheme of a confocal FCS setup. L1-L3: lenses; F1,F2: filters; D: dichroic mirror; SPAD: single photon avalanche diode. In the shown setup the fiber-end acts as a confocal pinhole, rejecting out of focus light.

part of the setup is identical to a confocal microscope. A laser beam is focused by means of a dichroic mirror and a high power water immersion objective into the sample that consists of an aqueous solution. Inside the sample fluorescence is excited and the emitted light is collected by the same objective. The fluorescence light is focused onto a pinhole located at the axis in the image plane of the detection system. The role of the pinhole is to efficiently reject out of focus

light and to further reduce the lateral extent of the observation volume. A dichroic mirror and an emission filter are used to filter scattered excitation light. Today single-photon avalanche diodes (SPAD) are used to detect fluorescence. These detectors collect single photons with an excellent photon detection efficiency (ratio of incident photons to detector counts) and a high time resolution.¹ After detection, the signal is processed by a hardware correlator or recorded by means of a multichannel scaler and stored for later software correlation.

The autocorrelation function of the intensity fluctuations, $\delta I(t) = I(t) - \langle I(t) \rangle_t$, at time τ is defined as [73]²

$$G(\tau) = 1 + \frac{\langle \delta I(t + \tau) \delta I(t) \rangle_t}{\langle I(t) \rangle_t^2}, \quad (4.1)$$

where $\langle \cdot \rangle_t$ denotes a time average. In FCS we deal in general with ergodic systems and may therefore replace the time average by an ensemble average, which is of some importance when deriving a mathematical model for $G(\tau)$. In this case

$$G(\tau) = 1 + \frac{\langle \delta I(\tau) \delta I(0) \rangle}{\langle I \rangle^2}, \quad (4.2)$$

where $\langle \cdot \rangle$ denotes an ensemble average. This function decays to 1 with time, τ ; the typical decay time gives information about the average duration of the fluctuation signal, which is coupled to the underlying dynamics (see Fig. 4.3 for an example). The power of FCS stems

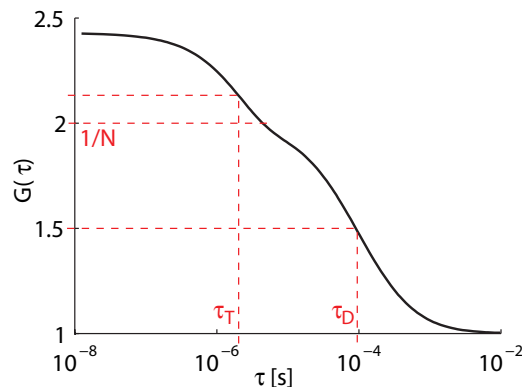


Figure 4.3: $G(\tau)$ for one-component diffusion and triplet kinetics. The inverse of the height of the lower plateau equals the number of molecules in the observation volume. $G(\tau)$ decreases to half of this value after the diffusion time τ_D . τ_T : mean triplet state lifetime.

amongst others from the fact that dynamics on very different time scales can be observed in one single measurement. The time window that can be accessed by FCS ranges typically from 10^{-12} s (when using a multichannel scaler) to several seconds. Besides the information about dynamics, which is embedded in the shape and time dependence of the autocorrelation, $G(\tau)$ carries information about concentrations. The amplitude of the autocorrelation, $G(0)$, is proportional to the variance of the intensity fluctuations. In the case of diffusion, the number of molecules in the observation volume follows a Poisson distribution. The average number of fluorescent molecules in the volume element is then simply related to $G(0)$ by $1/\langle N \rangle = G(0) - 1$.

¹As an example, the SPAD used in our experiments (SPCM-AQR-13-FC, PerkinElmer, Wellesley, MA) features a photon detection efficiency of maximal 70% at 650 nm and a single photon timing resolution of 350 ps FWHM.

²The authors define $G(\tau)$ without the summand 1, which is common practice. Here, the present definition was chosen for convenience, since it corresponds better to the signal provided by the used correlator.

The measured intensity fluctuations depend on the concentration fluctuations of fluorescent molecules in the observation volume

$$\delta I(t) = a \int_{\Omega} \text{MDE}(\mathbf{r}) \sum_{k=1}^m Q_k \delta C_k(\mathbf{r}, t) d^3r, \quad (4.3)$$

where the integral is carried out over the whole space Ω and $\delta C_k(\mathbf{r}, t) \equiv C_k(\mathbf{r}, t) - \langle C_k \rangle$. $C_k(\mathbf{r}, t)$ denotes the concentration of a particular molecular species k and $\delta C_k(\mathbf{r}, t)$ is the deviation from the mean $\langle C_k \rangle$. The parameter Q_k is the product of the fluorescence quantum yield with the absorption cross section of the component k and a is a constant that denotes the 'overall' detection efficiency of the system. The function MDE is the molecule detection efficiency [37, 72], which weighs the intensity contribution of fluorophores according to their position in the sample. Note, that we do not consider shot noise. This simplification does not affect the form of the autocorrelation function, since shot noise is uncorrelated for $\tau \neq 0$. Shot noise will nevertheless influence the signal to noise ratio in the FCS data. By substituting Eq. 4.3 into Eq. 4.2 we obtain $G(\tau)$, which is a sum of auto- and cross-correlation terms of different molecular species, weighted by their brightnesses (compare [37]):

$$\begin{aligned} G(\tau) &= 1 + \sum_{k,l} G_{kl}(\tau) \\ &= 1 + \frac{\sum_{k,l} Q_k Q_l \int_{\Omega} \int_{\Omega} \text{MDE}(\mathbf{r}) \text{MDE}(\mathbf{r}') \phi_{kl}(\mathbf{r}, \mathbf{r}', \tau) d^3r d^3r'}{(\sum_k Q_k \int_{\Omega} \text{MDE}(\mathbf{r}) \langle C_k(\mathbf{r}) \rangle d^3r)^2}. \end{aligned} \quad (4.4)$$

The concentration fluctuations $\phi_{kl}(\mathbf{r}, \mathbf{r}', \tau) \equiv \langle \delta C_k(\mathbf{r}, \tau) \delta C_l(\mathbf{r}', 0) \rangle$ have to be obtained by solving the differential equations that govern the molecular dynamics.

The observation volume is mathematically represented by the *molecule detection efficiency* (MDE) function. The MDE is proportional to the intensity detected from a single emitter as a function of its position, \mathbf{r} , in the sample volume. It is calculated by multiplying the excitation intensity I_{ex} by the *collection efficiency function* (CEF) [72]

$$\text{MDE}(\mathbf{r}) = I_{ex}(\mathbf{r}) \text{CEF}(\mathbf{r}). \quad (4.5)$$

The CEF describes the probability that a photon will be detected as a function of the position of the emitter [74] and reads

$$\text{CEF}(\mathbf{r}) = \frac{1}{\Delta} \int_S \text{circ}(\mathbf{r}'/\rho) \text{PSF}(\mathbf{r} - \mathbf{r}', z) dx dy, \quad (4.6)$$

where PSF denotes the point spread function of the optical system and Δ is a normalization factor. The convolution is carried out in the sample space. The disk function, circ, represents the transfer function of the pinhole projected into the sample space. Therefore, ρ is the diameter of the confocal pinhole divided by the magnification of the detection system.

In the case of confocal FCS, the MDE is frequently approximated by a product of three Gauss functions

$$\text{MDE}_g(\mathbf{r}) = \text{MDE}_g(0) \exp\left(-2\frac{x^2 + y^2}{\omega_{xy}}\right) \exp\left(-2\frac{z^2}{\omega_z}\right). \quad (4.7)$$

This approximation works quite well for most applications and the resulting deviation from the real $G(\tau)$ remains small. A better approximation is the so called Gauss-Gauss-Lorentzian

profile, where the z dependence of the MDE is modeled by a Lorentzian function. The molecule detection efficiency reads in this case [74]

$$\text{MDE}_l(\mathbf{r}) = \text{MDE}_l(0) \exp\left(-2\frac{r^2}{\omega(z)}\right), \quad (4.8)$$

with $\omega(z) = \omega_0 \left\{1 + [z\lambda/(\pi\omega_0^2)]^2\right\}$. The Gauss approximation is however most of the time the better choice because it leads often to a simple analytical form for $G(\tau)$.

The intensity autocorrelation function at time zero is inversely proportional to the number of molecules in the observation volume. In order to measure concentrations we need to assign a size to this volume. This size is normally defined by the effective volume V_{eff} [37]

$$V_{eff} \equiv \frac{W_1^2}{W_2}, \quad (4.9)$$

where

$$W_n \equiv \frac{1}{\text{MDE}^n(0)} \int \text{MDE}^n(\mathbf{r}) d^3r. \quad (4.10)$$

Using 4.7 we derive as an approximation for the effective volume

$$V_{eff} \approx \pi^{3/2} \omega_{xy}^2 \omega_z. \quad (4.11)$$

4.3 FCS for translational diffusion

Measuring diffusion is a particular important application of FCS. The determination of the diffusion coefficient, D , of a molecule in an aqueous solution allows to calculate its molecular weight by using the Stokes-Einstein relationship [73]

$$D = \frac{k_B T}{6\pi\eta R_h}. \quad (4.12)$$

The symbol η represents the viscosity of the solution. The molecular weight can be estimated from the hydrodynamic radius R_h . Measuring the diffusion coefficient can be used to determine the presence of an interaction between a fluorescently labeled ligand and a receptor if the receptor-ligand complex is big compared to the labeled ligand. The presence of a receptor-ligand complex will reflect itself in the autocorrelation curve as a second, slowly diffusing component. This finds an application in *high-throughput screening* (HTS) in pharmaceutical drug development [75, 76]. HTS, which consists in testing a huge number of synthetic or natural compounds against a target of therapeutic interest evolved to a discrete discipline in the last years. FCS allows to detect aggregation of the target with interaction partners and hence potential candidates for new drugs within seconds by monitoring changes in the diffusion coefficient. Though, the sensitivity of this technique is limited because the diffusion coefficient of a molecule is indirect proportional to the hydrodynamic radius, R_h , and therefore $D \propto 1/m^{1/3}$, where m is the mass of the molecules. To efficiently resolve two molecular species by measuring their diffusion coefficients, their mass, m , should differ by about an order of magnitude [19]. The differential equation that describes the dynamics of diffusion is the Einstein diffusion equation

$$\frac{\partial}{\partial t} C(\mathbf{r}, t) = D \nabla^2 C(\mathbf{r}, t). \quad (4.13)$$

This can be rewritten to give an equation for the concentration correlations

$$\frac{\partial}{\partial \tau} \phi(\mathbf{r}, \mathbf{r}', \tau) = D \nabla_{\mathbf{r}}^2 \phi(\mathbf{r}, \mathbf{r}', \tau), \quad (4.14)$$

where $\phi(\mathbf{r}, \mathbf{r}', \tau) \equiv \langle \delta C(\mathbf{r}, \tau) \delta C(\mathbf{r}', 0) \rangle$. The general solution of this equation can be found by Fourier transforming with respect to the spatial variables \mathbf{r} [37]. We mark Fourier transformed functions with a tilde and get

$$\frac{\partial}{\partial \tau} \tilde{\phi}(\mathbf{q}, \mathbf{r}', \tau) = -\mathbf{q}^2 D \tilde{\phi}(\mathbf{q}, \mathbf{r}', \tau), \quad (4.15)$$

where the elements of \mathbf{q} are the variables in Fourier space. This is easily integrated to give

$$\tilde{\phi}(\mathbf{q}, \mathbf{q}', \tau) = \tilde{\phi}(\mathbf{q}, \mathbf{r}', 0) \exp(-\mathbf{q}^2 D \tau). \quad (4.16)$$

By virtue of the convolution theorem for Fourier transformation we find

$$\phi(\mathbf{r}, \mathbf{r}', \tau) = \phi(\mathbf{r}, \mathbf{r}', 0) *_r \phi_G(\mathbf{r}, \mathbf{r}', \tau). \quad (4.17)$$

The symbol $*_r$ denotes convolution with respect to the variables \mathbf{r} and $\phi_G(\mathbf{r}, \mathbf{r}', \tau)$ is the Green's function:

$$\phi_G(\mathbf{r}, \mathbf{r}', \tau) = (4\pi D\tau)^{-3/2} \exp\left(-\frac{(\mathbf{r} - \mathbf{r}')^2}{4D\tau}\right). \quad (4.18)$$

The solution depends on the initial condition, or zero time correlation. These are determined by the condition of the ideality of the chemical solution, which states that the correlation length is small compared to the typical distances between molecules. The positions of different molecules are hence uncorrelated and the initial condition reads [17, 77, 19]

$$\phi(\mathbf{r}, \mathbf{r}', 0) = \langle C \rangle \delta(\mathbf{r} - \mathbf{r}'). \quad (4.19)$$

With Eq. 4.17 we get

$$\phi(\mathbf{r}, \mathbf{r}', \tau) = \langle C \rangle \phi_G(\mathbf{r}, \mathbf{r}', \tau). \quad (4.20)$$

Substituting into Eq. 4.4 and defining a diffusion time $\tau_D = \omega_{xy}/(4D)$ finally yields

$$G(\tau) = 1 + \frac{\gamma}{\langle N \rangle} \left(1 + \frac{\tau}{\tau_D}\right)^{-1} \left(1 + \frac{\tau}{\omega^2 \tau_D}\right)^{-1/2}, \quad (4.21)$$

where ω is a geometric parameter, defined as $\omega \equiv \omega_z/\omega_{xy}$ and γ is a geometric parameter depending mainly on the exact definition of $\langle N \rangle$, the mean number of molecules in the observation volume. Most commonly, $\langle N \rangle$ is defined by $\langle N \rangle \equiv \langle C \rangle V_{eff}$. With this definition, we derive the numerical value of γ by substituting Eq. 4.19 into Eq. 4.4. Using Eq. 4.10 we get

$$G(0) - 1 = \frac{W_2}{W_1^2 \langle C \rangle} = \frac{1}{\langle N \rangle}, \quad (4.22)$$

and hence $\gamma = 1$. Note that this holds only if the MDE is exactly represented by a product of three Gauss function. In reality, the MDE deviates from this approximation and γ will be slightly different from 1.

A more complete description takes into account that fluorophores may undergo intersystem crossing to a triplet state. In a simplified manner, this can be seen as a two-state process where a fluorophore fluctuates between a light-emitting state, Σ_1 (singlet states), and a dark state, Σ_0 (triplet state) [19].



In a more rigorous treatment (see e.g. [78]), three levels (S_0 , S_1 and T_1) would be considered. The fluorescence lifetime is in general several orders of magnitude smaller than the time scales

of the investigated dynamic processes. Because the kinetics of fluorescence transition does not contribute to the autocorrelation function for times much larger than the fluorescence lifetime, it is most of the time not taken into account in the analysis. Compared to the fluorescence lifetime (in the order of a few nanoseconds), the mean decay time of the triplet state, τ_T , is huge (a few milliseconds) and can be close to investigated time-scales. Hence, in general it should be taken into account in the analysis.

For later reference we will give a concise presentation of the derivation of the autocorrelation function for combined diffusion and triplet kinetics. The derivation presented here follows closely the derivation given in [19]. Triplet kinetics, according to the simple model presented above is described by the equation

$$\frac{d}{dt}\eta_i(t) = \sum_{j=0}^1 K_{ij} \eta_j(t), \quad (4.24)$$

where $\eta_i(t)$ denotes the fractional occupancy of the state Σ_i . The K_{ij} are

$$\mathbf{K} = \begin{pmatrix} -k_{01} & k_{10} \\ k_{01} & -k_{10} \end{pmatrix} \quad (4.25)$$

The k_{ij} are the rate constants of the transition according to scheme 4.23. We use the common simplification that the rates do not depend on the intensity, hence they do not depend on the position \mathbf{r} .

At this point, the picture we adapt to describe the effect of intersystem-crossing may seem very rough. The aim of the present work, however, is not to derive a function $G(\tau)$ that can be used as a tool to get precise parameter estimates for triplet kinetics but to analyze diffusion. In this context the above approximations are widely used and have proven appropriate in many FCS applications.

We define the concentration correlation-terms as $\phi_{ij}(\mathbf{r}, \mathbf{r}', \tau) \equiv \langle \delta C_i(\mathbf{r}, \tau) \delta C_j(\mathbf{r}', 0) \rangle$. The concentrations are C_1 for molecules in the light-emitting state and C_0 for molecules in the dark state. Therefore, $\eta_i(t) = C_i(t)/C(t)$ and $C(t) = C_0(t) + C_1(t)$. The function $G(\tau)$ is then given by Eq. 4.4 with subscripts that take the values 0 and 1. This formula simplifies to $G(\tau) = 1 + G_{11}(\tau)$ because the absorption cross section assigned to the dark state is zero and hence $Q_0 = 0$.

In the case of diffusion of one molecular species, considering triplet kinetics adds a source term to the Einstein diffusion equation.

$$\frac{\partial}{\partial \tau} \phi_{ij}(\mathbf{r}, \mathbf{r}', \tau) = D \nabla_{\mathbf{r}}^2 \phi_{ij}(\mathbf{r}, \mathbf{r}', \tau) + \sum_{k=0}^1 K_{ik} \phi_{kj}(\mathbf{r}, \mathbf{r}', \tau), \quad (4.26)$$

This equation can be solved by making the ansatz

$$\phi_{ij}(\mathbf{r}, \mathbf{r}', \tau) = g_{ij}(\tau) \phi(\mathbf{r}, \mathbf{r}', \tau), \quad (4.27)$$

where $\phi(\mathbf{r}, \mathbf{r}', \tau)$ is a solution of Eq. 4.14. It follows that the $g_{ij}(\tau)$ must satisfy the Eqs. 4.24 for all j . In matrix notation:

$$\frac{d}{d\tau} \mathbf{g} = \mathbf{K} \mathbf{g}. \quad (4.28)$$

These equations are analogue to the Kolmogorov equations for a two-state Markov process [79] but with initial conditions

$$g_{ij}(0) = \delta_{ij} \langle \eta_i \rangle. \quad (4.29)$$

The initial conditions follow again from the assumption of ideality of the chemical solution. The general solution for Eq. 4.28 reads

$$\mathbf{g}(\tau) = \mathbf{g}(0) e^{\mathbf{K}\tau}. \quad (4.30)$$

We derive

$$g_{11}(\tau) = \frac{k_{01}}{(k_{01} + k_{10})^2} \{k_{01} + k_{10} \exp [-(k_{01} + k_{10})\tau]\}. \quad (4.31)$$

By substituting $\phi_{11}(\mathbf{r}, \mathbf{r}', \tau)$ into Eq. 4.4 and integrating we derive for the autocorrelation function of combined diffusion and triplet kinetics

$$\begin{aligned} G_T(\tau) &= 1 + \frac{g_{11}(\tau)}{\eta_1^2} [G(\tau) - 1] \\ &= 1 + \frac{\gamma}{\langle N \rangle} \left[1 + \frac{p}{1-p} \exp\left(-\frac{\tau}{\tau_T}\right) \right] \left(1 + \frac{\tau}{\tau_D}\right)^{-1} \left(1 + \frac{\tau}{\omega^2 \tau_D}\right)^{-1/2}. \end{aligned} \quad (4.32)$$

The parameter $p \equiv k_{10}/(k_{10} + k_{01})$. We used that at equilibrium $\langle C_1 \rangle / \langle C_0 \rangle = k_{01}/k_{10}$, which implies that p equals the fraction of molecules (in the observation volume) in the triplet state, $p \equiv \eta_0$. The mean decay time of the triplet state is given by $\tau_T = 1/(k_{10} + k_{01})$.

Chapter 5

Total internal reflection fluorescence

We already noted the importance of a small observation volume for FCS measurements. Decreasing the size of the observation volume will, for a given concentration, allow to enter a regime where at each moment only the signal of a single molecule is observed. In addition, noise due to e.g. scattered excitation light will be reduced. Further arguments for a very small observation volume exist when the studied molecular system is partly or completely immobilized. Examples are two-dimensional diffusion (e.g. in membranes), binding kinetics on immobilized receptors or enzyme kinetics [80]. In this cases one would ideally have an observation volume with comparable size to the observed molecules, not only to reduce the background from scattered light but also to 'fade out' other dynamical processes like diffusion of free dyes in solution. To create an observation volume of the size of a single molecule is not possible, however if the studied molecular system is bound to a glass surface, total internal reflection excitation may be used to efficiently confine the observation volume to the surface.

5.1 Total internal reflection (TIR)

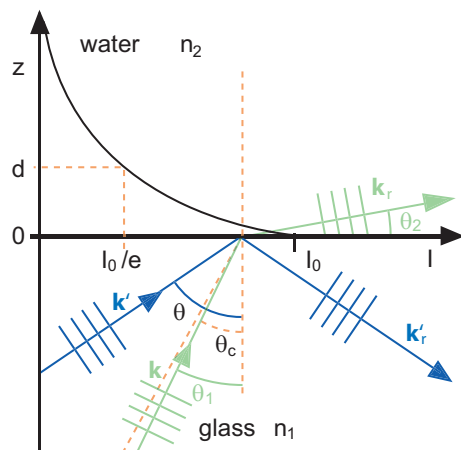


Figure 5.1: Scheme illustrating total internal reflection. Plane waves are incident on a glass/water interface from beyond. \mathbf{k}' and \mathbf{k}'_r : wave vectors of incident and totally reflected waves, respectively; \mathbf{k} and \mathbf{k}_r : wave vectors of incident and refracted waves, respectively; θ : incidence angle of totally reflected wave; θ_c : critical angle; θ_1 : incidence angle of refracted wave; θ_2 : angle of refraction; I : intensity; I_0 : intensity at $z = 0$.

When light traverses an interface between two media with different refractive indices, n_1 and

n_2 , it is refracted according to Snell's law (see Fig. 5.1)

$$n_1 \sin \theta_1 = n_2 \sin \theta_2. \quad (5.1)$$

For a plane wave that is incident from the optically denser medium at the interface, ($n_1 > n_2$), the refracted wave travels parallel to the interface for an angle of incidence θ_c , given by

$$\sin \theta_c = \frac{n_2}{n_1} \quad (5.2)$$

For angles $\theta_1 > \theta_c$ the incident wave is reflected back into the denser medium. This effect, called *total internal reflection* builds the basis for light guidance in optical fibers and waveguides. Solving the Maxwell equations for this case shows that the z component of the wave vector for the refracted beam becomes imaginary. The intensity is therefore not zero inside the medium with refractive index n_2 but decays exponentially with the distance, z , to the interface.

$$I(z) = I(0)e^{-z/d} \quad (5.3)$$

The characteristic decay length, d , at which the intensity decays by a factor $1/e$ is dependent on the wavelength in vacuum, λ_0 , refractive indices, n_1 and n_2 and incidence angle θ :

$$d = \frac{\lambda_0}{4\pi} (n_1^2 \sin^2 \theta - n_2^2)^{-1/2}. \quad (5.4)$$

The light field in the medium with refractive index n_2 is called the *evanescent field*, or *evanescent wave*. The intensity distribution of the evanescent wave is confined to the close proximity of the interface; d is typically smaller than the wavelength, except for $\theta_1 \approx \theta_c$ where d diverges (see Fig. 5.2). This electromagnetic field is capable of exciting fluorescent molecules close to the interface. In fact, the excitation of fluorescence was used as an early proof for the existence of the evanescent field [81].

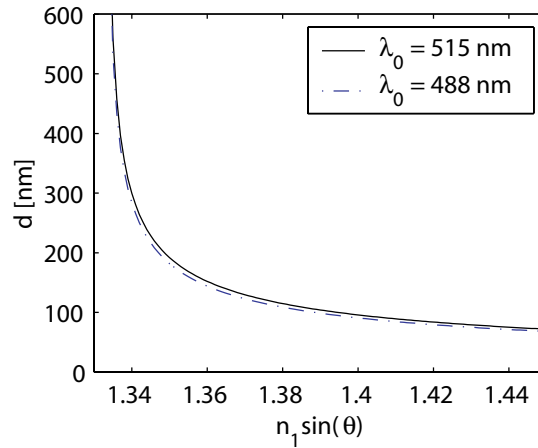


Figure 5.2: The penetration depth of the evanescent field, d , as a function of $\varrho \equiv n_1 \sin(\theta)$. Two plots are shown, for two wavelengths (in vacuum), which correspond to the main lines of an argon-ion laser. The function $d(\varrho)$ is plotted for angles bigger than the critical angle ($\varrho = 1.33$) at which d becomes infinite. The upper limit in this graph corresponds to the theoretical limit of the incidence angle in an objective-type TIRF setup using a 1.45 NA objective (see below).

Solving the Maxwell equations for a plane wave undergoing total internal reflection at a

solid/liquid interface ($\theta > \theta_c$) yields the amplitude components of the electric field at $z = 0$ [22]

$$E_x = \left(\frac{2 \cos \theta \sqrt{\sin^2 \theta - n^2}}{\sqrt{n^4 \cos^2 \theta + \sin^2 \theta - n^2}} \right) A_{\parallel} e^{-i(\delta_{\parallel} + \pi/2)}, \quad (5.5)$$

$$E_y = \left(\frac{2 \cos \theta}{\sqrt{1 - n^2}} \right) A_{\perp} e^{-i\delta_{\perp}}, \quad (5.6)$$

$$E_z = \left(\frac{2 \cos \theta \sin \theta}{\sqrt{n^4 \cos^2 \theta + \sin^2 \theta - n^2}} \right) A_{\parallel} e^{-i\delta_{\parallel}}. \quad (5.7)$$

The amplitude components of the magnetic field read

$$H_x = \left(\frac{2 \cos \theta \sqrt{\sin^2 \theta - n^2}}{\sqrt{1 - n^2}} \right) A_{\perp} e^{-i(\delta_{\perp} - \pi)}, \quad (5.8)$$

$$H_y = \left(\frac{2n^2 \cos \theta}{\sqrt{n^4 \cos^2 \theta + \sin^2 \theta - n^2}} \right) A_{\parallel} e^{-i(\delta_{\parallel} - \pi/2)}, \quad (5.9)$$

$$H_z = \left(\frac{2 \cos \theta \sin \theta}{\sqrt{1 - n^2}} \right) A_{\perp} e^{-i\delta_{\perp}}. \quad (5.10)$$

The relative refractive index is given by $n \equiv n_2/n_1$ and A_{\parallel} and A_{\perp} are the amplitude components of the incident electric field vector, parallel (p-polarized) and perpendicular (s-polarized) to the plane of incidence, respectively. The phases δ_{\perp} and δ_{\parallel} are defined as

$$\delta_{\parallel} \equiv \arctan \left(\frac{\sqrt{\sin^2 \theta - n^2}}{n^2 \cos \theta} \right), \quad (5.11)$$

$$\delta_{\perp} \equiv \arctan \left(\frac{\sqrt{\sin^2 \theta - n^2}}{\cos \theta} \right). \quad (5.12)$$

The energy flux, given by the real part of the Poynting vector, ($\mathbf{S} = c/(4\pi)\mathbf{E} \times \mathbf{H}$) is parallel to the interface and to the plane of incidence. Interestingly, if the field is not s-polarized, the electric field has a non-vanishing longitudinal component. As a consequence, \mathbf{E} is elliptically polarized in the plane of incidence.

Given the electromagnetic field at $z = 0$, one can calculate the intensity $I_0 = 1/2\epsilon_0 c n_2 |\mathbf{E}|^2$, where ϵ_0 is the permittivity of free space and c the velocity of light. The intensity is the sum of intensity contributions from the parallel and vertical polarized fields $I_0 = I_0^{\parallel} + I_0^{\perp}$, which are

$$I_0^{\parallel} = \mathcal{I}_{\parallel} \frac{4 \cos^2 \theta (2 \sin^2 \theta - n^2)}{n^4 \cos^2 \theta + \sin^2 \theta - n^2}, \quad (5.13)$$

$$I_0^{\perp} = \mathcal{I}_{\perp} \frac{4 \cos^2 \theta}{1 - n^2}, \quad (5.14)$$

$$(5.15)$$

with $\mathcal{I} = \mathcal{I}_{\parallel} + \mathcal{I}_{\perp}$ denoting the incident intensity and $\mathcal{I}_{\parallel, \perp} = |A_{\parallel, \perp}|^2$. Figure 5.3 shows the dependence of I_0 as a function of the incidence angle for s- and p-polarized incident fields. Remarkably, I_0 exceeds the intensity of the incident field by a factor of one to five in a range of about 15° from the critical angle.

The idea of TIR-FCS consists in decreasing the axial extent of the observation volume by exciting fluorescence by means of an evanescent field. This idea was successfully applied in very

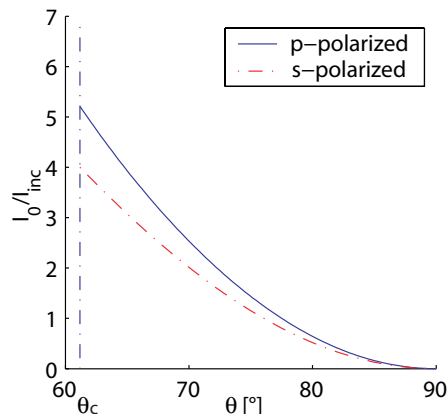


Figure 5.3: Intensities of the evanescent fields at a solid/liquid interface for s- and p-polarized incident fields, respectively. Intensities are normalized with respect to the intensities of the incoming wave. Refractive indices are $n_1 = 1.33$ (water) and $n_2 = 1.518$ (glass), implying a critical angle of $\theta_c = 61.2^\circ$. I_{inc} : intensity of incident wave; I_0 : intensity of the evanescent field at the interface ($z = 0$); θ : incidence angle in degrees; θ_c : critical angle.

early FCS experiments [26, 27], in fact it was the natural way to get a small observation volume before the adaption of the confocal principle. Evanescent wave excitation is further the base of a whole domain in microscopic imaging, known as *total internal reflection fluorescence microscopy* (TIRF microscopy, or TIRFM)

5.2 Total internal reflection fluorescence microscopy (TIRFM)

TIRF microscopy is a powerful method to image cell membranes. With this approach the region of contact between living cells and the substrate on which they grow can be selectively imaged. The cell surface is central to a huge number of chemical and physical processes and phenomena including triggering of cellular activities upon binding of hormones, neurotransmitters and antigens; electron transport to the mitochondrial region; diffusion and aggregation of membrane-bound receptors; phase separation and generation of rafts.

An interesting application of TIR in this context is the direct observation of exocytosis in living cells. *Exocytosis*, as part of the cellular metabolism, is the transport mechanism of substances from the inside to the outside of the cell. The substances to be expelled are transported by means of vesicles towards the cell membrane. After contact the vesicles merge with the membrane and release their cargo to the cells environment. By using sensitive CCD cameras with high time resolution, the movement of the vesicles containing fluorescently labeled cargo as well as the process of merging can be monitored [82]. Because of the fast decay of the excitation intensity, the brightness of the vesicles vary with their distance to the surface. Monitoring the brightness allows for very accurate measurements of their z positions. In this way, the distance to the surface can be measured with about 2 nm precision, which is far beyond the resolution limit of a light microscope [25].

Applications are not restricted to the imaging of cell surfaces. Processes at solid/liquid interfaces are central to several industrial and medical applications, e.g. detection of genes or serum antibodies by means of microarrays.

Moreover, the excellent signal to noise ratio that can be obtained in TIRF microscopy allowed for the first direct observation of the catalytic activity of a single enzyme molecule. In [40] T. Funatsu et al. showed the feasibility of monitoring single adenine tri-phosphate (ATP)

turnovers of the enzyme myosin. *Myosin* is a member of the *P-loop NTPases* superfamily. Proteins of this family are capable of converting chemical energy in the form of ATP into mechanical work. Such proteins bear for this reason the name *molecular motors* and are responsible for muscle contraction, cargo transport inside the cell and cellular movement. Myosin e.g. moves along filaments of the protein actin and thereby causes muscle contraction.

In the cited experiment, biotinylated myosin was attached to a streptavidin coated quartz slide. ATP, labeled with the dye Cy3 was freely diffusing above the slide. When ATP bound to a myosin molecule, this became visible as a bright spot on an image obtained by means of a CCD camera. Using a single photon avalanche diode, Funatsu et al. were further able to record time-traces of single enzyme turn-overs.

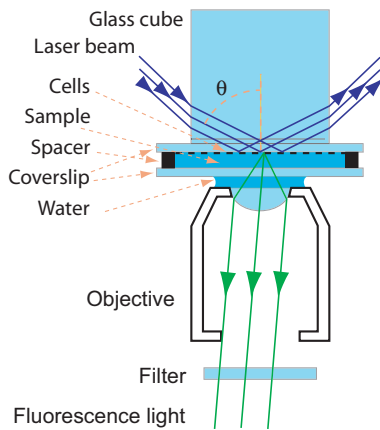


Figure 5.4: Illustration of excitation and light collection for prism-type TIRF microscopy. The glass cube is optically connected to the upper cover slide by means of immersion oil. A water-immersion objective is used to collect fluorescence.

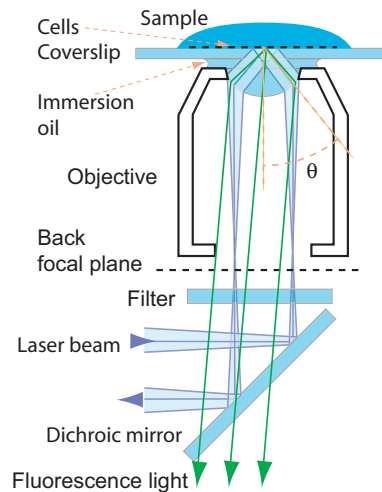


Figure 5.5: Excitation and light collection for objective-type TIRF microscopy. A high NA oil-immersion objective is used to excite fluorescence and to collect emitted light

There exist two main configurations of TIRF microscopy, called prism-type TIRFM and objective-type TIRFM. Two representative setups are shown in Figs. 5.4 and 5.5. In the case of prism-type TIRF microscopy (Fig. 5.4) a glass-slide is optically connected to the lower side of a prism by means of immersion oil. The studied molecular system is attached to the lower surface of the glass-slide. The sample, which consists of an aqueous solution and the molecular system is sandwiched between two glass slides. A water-film separates the lower glass slide from a water immersion objective. A laser beam traveling inside the prism is used to generate an evanescent wave at the interface between the upper glass-slide and the sample, exciting the emission of fluorescence. The objective images the glass/sample interface onto a CCD camera.

Objective type TIRFM uses an oil-immersion objective with a $NA \geq 1.4$ to excite fluorescence and to collect the emitted light. Here, a laser beam is focused onto the back focal plane of the objective, which causes the beam to emerge collimated from the objective. The beam is focused off-axis onto the back focal plane, therefore it emerges under a certain angle $\theta > 0$ from the objective. If this angle is large enough the beam is totally reflected at the cover slide/water interface and an evanescent field builds up at the surface. Light is collected by the same objective. The emitted light traverses a dichroic mirror, used to separate the excitation-path from the detection-path, and an emission filter, which rejects scattered excitation light and auto-fluorescence excited in the objective, cover slide and buffer. The interface is finally imaged onto a CCD camera.

These are the most common configurations, both were successfully applied to image single fluorescent molecules. Several variations of the shown setups exist, including configurations that allow to use a conventional light source instead of a laser, or a waveguide instead of a prism to generate an evanescent field.

Both setups have their advantages and disadvantages. The most important characteristics which have to be considered when choosing a particular configuration are discussed below.

5.2.1 Background

In prism-type TIRFM, the excitation path and the detection path are decoupled. This can in principle lead to a reduced background since a laser beam that traverses objective, immersion oil and cover slide excites autofluorescence in those components. As another consequence, no reflected laser light travels in the direction of the CCD camera. Moreover, the incidence angle, θ , of the laser beam can take any value in between θ_c and $\pi/2$. A higher angle will, according to Eq. 5.4, result in a smaller field depth, which will result in a smaller background.

In objective-type TIRFM, the angle is limited by the NA of the used objective. Most common are objectives with an NA of 1.45, which limits θ to $\theta_{max} \equiv \arcsin \text{NA}/n_2$. The maximum angle when using a glass cover slide is approximately $\theta_{max} \approx 75^\circ$.

In objective-type TIRFM, the back-reflected laser beam travels in direction of the CCD camera. Because the laser beam is focused onto the back focal plane of the objective, there exists an efficient way to reject the reflected light by applying a spatial filter. The reflected beam is again focused onto the back focal plane. One can introduce an optical obstacle, e.g. an opaque disk with a diameter comparable to the diameter of the laser focus in the back focal plane or an equivalent plane to block the reflected light. The amount of blocked fluorescence is negligible, since the surface of the disk can be small compared to the intersection of the back focal plane with a beam emerging from a point source at the glass/water surface. However, tests in our laboratory showed that the contribution of reflected light to the background is quite small, provided that an optimal set of fluorescence filters is employed. The gain in the signal to background ratio was approximately 15%.

5.2.2 Collection efficiency

One major disadvantage of the prism-type excitation is a lower collection efficiency. In objective-type TIRFM a high NA objective is used that collects, by its nature light efficiently. This is further amplified by the fact that the emission of a (randomly oriented) fluorophore becomes highly anisotropic when it comes close to a dielectric interface. Emission into the medium with higher refractive index, glass in our case, is favored and in addition most of the energy emitted into the glass propagates at an angle close to θ_c . It was shown [29] that the fraction of collected power can exceed 60% in this configuration (see also chapter 6).

It is disadvantageous to use a high NA oil immersion objective for prism-type TIRFM. The working distance is very short (0.11 mm for a cover slide thickness of 0.17 mm for the Zeiss α -Plan Fluor, used in our experiments), which, if a prism-type configuration is used, limits the sample thickness to very low values. Furthermore, these objectives are designed to work with high refractive index media. Focusing into an aqueous solution introduces aberrations that impair the collection efficiency of high NA oil-immersion objectives [19]. However, the special geometry in prism-type TIRFM requires focusing into an aqueous solution.

5.2.3 Handling

In objective-type TIRFM the sample access is not hindered by the presence of a prism, in contrast to prism-type TIRFM. This facilitates sample handling in general and allows for easy solution change and electrophysiology studies.

Chapter 6

Objective-type TIR-FCS

6.1 Motivation

As already pointed out before, FCS experienced a substantial increase in popularity with the adaption of the confocal principal. This development resulted in a reduced observation volume, an increased signal to background ratio and in the possibility to observe single molecule events. Before the advent of confocal FCS, the natural way to confine the observation volume was by using an evanescent field for fluorescence excitation. This method was first introduced by Thompson et al. [26, 27, 83]. In 1981, the authors proposed the adaption of a prism-type TIRFM setup for FCS measurements, which could be used to study adsorption of rhodamine labeled immunoglobulin on quartz [27]. In [26] they presented the theoretical framework for *total internal reflection FCS* (TIR-FCS) and also FRAP applied to measure adsorption, and binding of fluorescently labeled ligands to receptors immobilized at a glass surface. Shortly later, the possibility to obtain surface binding rates of non-fluorescent molecules by means of TIR-FCS was theoretically shown. Although the theoretical framework for TIR-FCS was already established in the beginning of the 1980's, the technique was rarely applied in the following years. Other publications that showed experimentally the applicability of the method to different fields in life science followed only in the late 1990's. 1998 Hansen et al. [84] investigated reversible adsorption kinetics of the cationic dye Rh6G to modified silica surfaces. In [85] the same group showed that the surface concentration of bound fluorophores can be determined by means of TIR-FCS. TIR-FCS was further used to determine local diffusion coefficients of the antibody immunoglobulin G (IgG) adjacent to phospholipid bilayers [86] or to study the association of IgG to receptors [87]. In the latter experiment the authors were able to determine average surface densities of bound IgG, local concentrations of IgG in solution, as well as the diffusion and dissociation rate of the protein. TIR-FCS was also used to investigate molecular transport in thin sol-gel (porous silicon oxide) films [88].

The number of successful applications was though limited. Besides inherent complexity of biochemistry on surfaces this may be due to the fact that the signal to noise ratio in FCS is inevitably lower for measurements on a solid/liquid interface than in solution. Unfortunately, to the authors knowledge, there exists no publication that investigates the question of signal-strength and signal to background ratio in TIR-FCS. In experiments performed in our laboratory the signal to background ratio in TIR-FCS measurements on diffusing molecules using a prism-type setup was too low to obtain reliable estimates. Especially count rates per molecule were far beyond what is standard in confocal FCS.

Comparable count rates would make TIR-FCS the method of choice for many applications at solid/liquid interfaces [89]. In chapter 5 the advantages of the TIR- with respect to the confocal excitation scheme were briefly discussed. Confining the excitation field to the studied region can

reduce background and unwanted signals from freely diffusing ligands.

In order to increase the performance of TIR-FCS in terms of signal strength per molecule, we developed a setup based on objective-type TIRF. The following chapter is intended to give a detailed technical description of the objective-type TIR-FCS setup used for our experiments.

6.2 Description of the setup

A brief description of the setup is given in paper II and paper III. Figure 6.1 shows a detailed

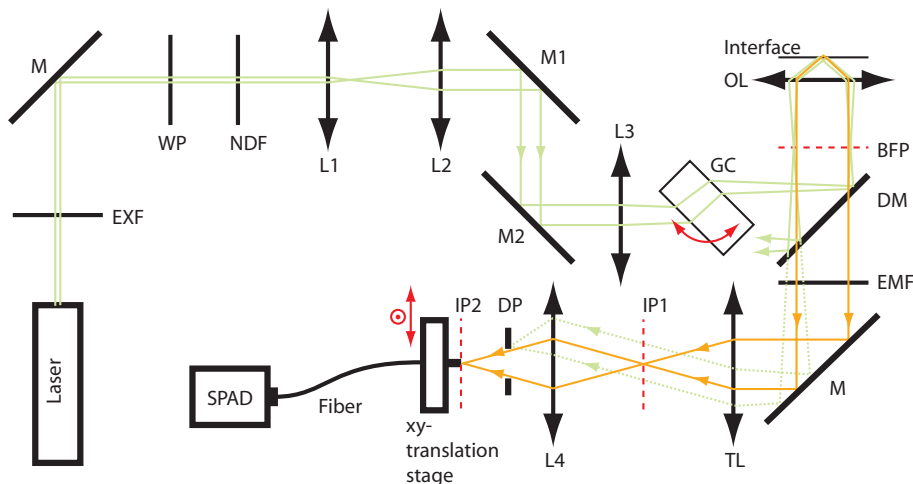


Figure 6.1: Detailed scheme of objective-type TIR-FCS. For discussion of the setup, see text. EXF: excitation filter; M: mirror; WP: $\lambda/4$ waveplate; ND: neutral density filter; L1-L4: lenses; GC: tiltable glass cube; BFP: back focal plane of objective; OL: objective lens; EMF: emission filter; TL: tube lens; IP1: first image plane; DP: diaphragm; IP2: second image plane.

scheme of the optical configuration. To excite fluorescence, we used an argon ion laser (model 2214-25ML, Cyonics, Sunnyvale, CA), which has two main emission lines at 488 nm and 515 nm, providing a maximum power 18 mW and 25 mW, respectively. Interference filters placed immediately after the laser were used to select either of the two lines. Interference effects due to the filter observed at the glass/water interface (cover slide surface) could be minimized by slightly inclining the filter with respect to the optical axis. A $\lambda/4$ waveplate was used to transform the originally linear polarization of the laser beam to circular polarization. This optical element was introduced to omit a selective excitation of fluorophores that was undesirable for most of our experiments. The beam was enlarged by means of a Kepler telescope formed by lenses L1 (with focal length $f_1 = 19$ mm) and L2 ($f_2 = 150$ mm). The diameter of the collimated beam was roughly 1 cm. Aligning of the laser to the optical axis of the inverted microscope (IX70, Olympus, Tokyo, Japan) was conveniently done using a periscope with movable mirrors (M1 and M2). To focus the laser beam onto the back focal plane of our objective, we used an achromat (L3) with focal length $f_3 = 300$ mm. Before entering the microscope body, the beam traversed a glass cube (thickness $d = 10$ mm) mounted on a rotation table. Tilting the glass cube allowed for a precise lateral shift of the laser beam and therefore of the incidence angle on the glass/water interface. The laser beam was reflected at a dichroic mirror into the objective (α -Plan-Fluar, 1.45 NA, 100 \times , Carl Zeiss Jena GmbH, Jena, Germany). By adjusting the tilt of the glass cube, we were able to achieve total internal reflection at the interface of the sample and a standard glass cover slide (thickness 150 μ m), optically connected to the objective by means of immersion oil.

Emitted light was collected by the same objective. Elastic and inelastic scattered excitation light as well as light reflected at the glass/sample interface was efficiently rejected by a dichroic mirror and an interference filter. Fluorescence was imaged onto a fiber-end situated at the image plane in front of the microscope's side-port (IP1, configuration not shown in the figure). We used in general a multimode fiber with a core diameter of $50\ \mu\text{m}$. The fiber-end, which ensured a lateral confinement of the observation volume was mounted onto a motorized xy -scanning stage. This allowed for automatized lateral scanning of the fluorescence image and rapid detection of surface binding sites (see chapter 8). The fiber-end was coupled to a SPAD (SPCM-AQR-13-FC, PerkinElmer, Wellesley, MA), which detects single photons in the wavelength region of interest ($500\ \text{nm} < \lambda < 600\ \text{nm}$) with single photon detection efficiencies of 50% - 68%. The output signal was split and further processed by a hardware correlator and a single photon counting module (SPCM, SPC-630, Becker & Hickl GmbH, Berlin, Germany) used as a multichannel scaler. Data was stored on two personal computers and further analyzed by in-house build software.

In some of our experiments we introduced a lens (L4) of focal length $f_4 = 70\ \text{mm}$ positioned at a distance of $2f_4$ after the image plane to produce a second image of the same size. Fluorescence was again detected using a fiber-coupled SPAD with the free fiber-end situated in the second image plane (IP2). This configuration offers the interesting possibility of spatial filtering of the laser beam reflected at the glass/water interface.

A cooled CCD camera (DV434-BV, Andor Technology, Belfast, Northern Ireland) was mounted at a second camera port of the Olympus microscope. By switching between camera ports, the setup could be quickly transformed into a standard TIRF microscope and back. The CCD camera was e.g. used to find and image single bio-molecules or binding sites on the surface (see chapter 8 and 9).

6.2.1 Fluorescence excitation

A very precise alignment of the excitation path was crucial in order to produce a neat evanescent field. In particular slight soiling in form of dust particles or condense water on the lower surface of the cover slide was sufficient to impair the generation of an evanescent field. The field quality could be easily judged by observing the diffusion of fluorescent latex beads (with a diameter of $170\ \mu\text{m}$) above the surface. When the objective was focused onto the cover slide surface the beads appeared as short, point-shaped flashes. Almost no lateral movement and no blurred beads were observed, which was quite different from the case of bright-field illumination.

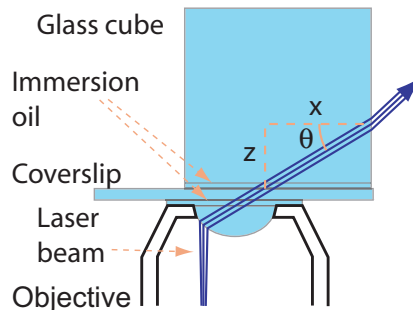


Figure 6.2: Scheme of a configuration for measuring the incidence angle, θ , by outcoupling of the laser beam using a prism.

The evanescent field depth was determined in two different ways, by FCS measurements on dye molecules above the surface and by measuring the angle at which the laser beam is incident

on the cover slide surface. This was done by bringing a glass cube into optical contact with the cover slide by means of immersion oil. In this way, the beam was outcoupled (see Fig. 6.2) and the angle could be determined. To be precise, the emerging beam is slightly divergent ($\sim 5^\circ$); so we measured a distribution of angles rather than a precise value. The mean value of this distribution, which we will simply call the incidence angle in the following, was typically 71° . Using Eq. 5.4 the evanescent field depth was calculated to equal 72 nm and 84 nm for the blue line (488 nm) and the green line (515 nm), respectively. This was in excellent agreement with sizes inferred from FCS measurements (see chapter 7).

To determine the intensity at the glass/water interface, the fluorescence of rhodamine 6G (Rh6G) dye molecules diffusing above the cover slide surface, was imaged onto a CCD camera. The intensity distribution is Gaussian on the surface and has almost rotational symmetry. From the camera image, the radius of this distribution, r_E , (half of the FWHM) was estimated to be in the order of $7.5 \mu\text{m}$. Given r_E , the intensity in the center of the distribution and therefore inside the observation volume (optimal positioning of the fiber-end presumed) can be obtained by using the relationship between total power, P , and intensity, $I(r)$:

$$P = \int_0^{2\pi} d\phi \int_0^\infty \mathcal{I}(r)r dr, \quad (6.1)$$

where P is the incident power and $\mathcal{I}(r)$ the incident intensity at the interface in the lower half-space. Assuming that the intensity distribution on the surface is given by

$$I(r) = I_0 \exp\left(\frac{-r^2}{2\sigma^2}\right), \quad (6.2)$$

and using $\sigma = r_E/\sqrt{2\ln 2}$, we get

$$I_0 = \alpha \frac{P \ln 2}{r_E^2 \pi}. \quad (6.3)$$

The factor α is defined as $\alpha \equiv I_0/\mathcal{I}(0)$. For an incidence angle of $\theta \approx 70^\circ$ it follows that the incident intensity is 'amplified' by a factor of $\alpha \approx 2$. We measured a loss in the whole excitation path i.e. a ratio between the intensity after the laser and the intensity after the objective for an incidence angle set to 0, of about 50%. Given these values, we estimate $I_0 \approx 8 \mu\text{W} \mu\text{m}^{-2}$ per mW applied laser power (measured right after the laser). This is low compared to what is normally used in confocal FCS experiments. One could increase this value by narrowing the distribution. This can be done by changing the magnification of the telescope or the focal length of lens L3.

Theoretically it is possible to change the evanescent field depth by tilting the glass cube. Given a NA of 1.45, the possible incidence angles for total internal reflection are approximately $62^\circ < \theta < 73^\circ$. We experienced that the range of accessible angles is almost zero, presumably due to the finite size of the laser beam inside the objective.

6.2.2 Fluorescence detection

The main advantage of the objective-type configuration with respect to the prism-type configuration is a higher collection efficiency. This is due to an altering of the emission properties of fluorophores, when they come close to the cover slide surface [90, 91, 92, 93]. Characteristics of fluorescence emission close to an interface between dielectric media can be derived by modeling the fluorophore by a classical dipole. For a randomly oriented dipole near an interface separating two dielectric half-spaces the radiated power is canalized along the critical angle and emission into the medium with higher refractive index is favored. This is illustrated in Fig. 6.3,

which shows polar-coordinate plots for the power $S(\Omega, z)$ radiated by a dipole into a differential angle $d\Omega$ about Ω .¹ Plots are drawn for two (in this case oriented) dipoles at different distances from the surface. Most of the power is emitted into the lower halfspace. A substantial portion is emitted in directions corresponding to angles higher than the critical angle if the dipole is situated at the surface.

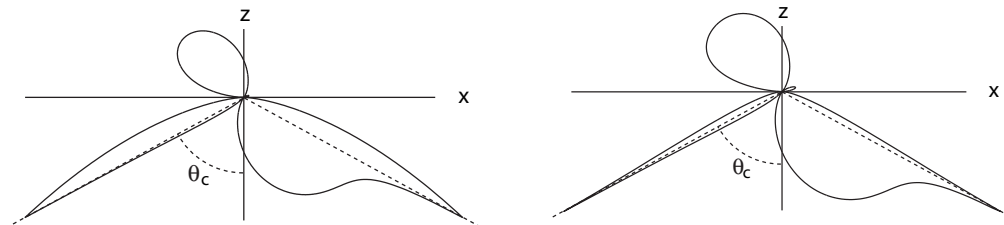


Figure 6.3: Normalized radiated power for dipoles close to a dielectric interfaces represented a polar-coordinate plots. Left: the dipole is situated at the interface ($z = 0$). Refractive indices for the half-space above and below the interface are $n_2 = 1.33$ (water) and $n_1 = 1.52$ (glass), respectively. The dipole axis is located in the xz -plane and inclined 45° with respect to the vertical. Right: As above but for a dipole at a distance $z = 100$ nm from the surface. θ_c : critical angle.

The emission profiles were calculated using a formalism proposed by J. Mertz [90]. This simple 'input-output' formalism is based on the Lorentz reciprocity theorem [94]. According to classical electrodynamics, the polarization \mathcal{P} of the dipole is related to a driving electromagnetic field \mathbf{E}_d by

$$\mathcal{P} = \epsilon_0 \mathcal{A} \mathbf{E}_d, \quad (6.4)$$

where ϵ_0 is the free-space permittivity and \mathcal{A} the generalized polarizability of the dipole, depending on its distance and orientation relative to the interface. The driving field is a linear transformation of the incoming field \mathbf{E}_{in} :

$$\mathbf{E}_d = \mathcal{K}(\theta) \mathbf{E}_{\text{in}}, \quad (6.5)$$

where the transfer matrix $\mathcal{K}(\theta)$ for the angle of incidence θ is a function of the Fresnel coefficients (definitions of angles are as in Fig. 5.1). The field emitted by the dipole, \mathbf{E}_{out} , into a differential solid angle $d\Omega$ about Ω depends on the dipoles polarization in a similar way as the driving field depends on the incoming field:

$$\mathbf{E}_{\text{out}} \propto \mathcal{K}'(\Omega) \mathcal{P}, \quad (6.6)$$

In order to derive \mathbf{E}_{out} one has to calculate the linear transfer matrix $\mathcal{K}'(\Omega)$, which according to the Lorentz reciprocity theorem is related to $\mathcal{K}(\theta)$ by a simple linear transformation. In particular $\mathcal{K}'(\Omega) = \mathcal{K}^T(\theta)$, where the subscript T denotes matrix transpose, if Ω is in the plane of incidence. Given \mathbf{E}_{out} , we can calculate the fraction of power, $P(z)$, radiated by a dipole at a distance z from the interface and collected by the microscope objective. The function $P(z)$ describes the net effect of the dielectric interface on the collection efficiency. If light is collected from beyond (for a situation as in Fig. 5.1), we have for a randomly oriented dipole

$$P(z) = 2\pi \int_0^{\theta_m} S(\theta, z) \sin \theta d\theta, \quad (6.7)$$

¹The polar-coordinate plots are to be interpreted as follows: For each point on the drawn curve, the length of the corresponding position vector is proportional to the differential power emitted into the direction of the position vector.

where $\theta_m = \arcsin(\text{NA}/n_1)$ and $S(\theta, z) = \frac{1}{2}\epsilon_0 c n_1 r^2 |\mathbf{E}_{\text{out}}|^2$ is the radiative power carried in the differential solid angle $d\Omega$ about Ω . Here, we averaged over all possible dipole positions. The symbol r denotes the far-field distance from the origin and c is the velocity of light. If light is collected from above, integration is carried out in the limits $[\theta_m, \pi]$ and n_2 replaces n_1 .

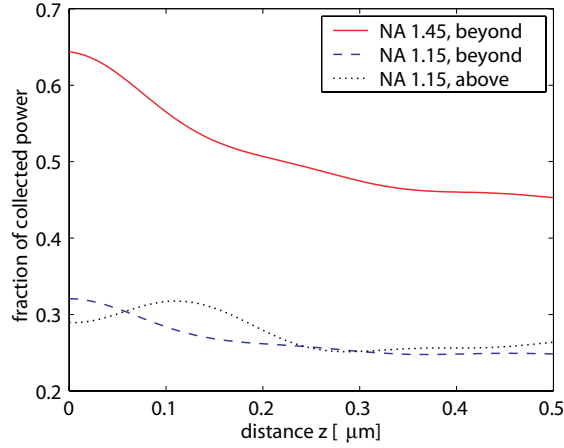


Figure 6.4: Fraction of power emitted by a randomly oriented dipole in water above a glass slide into a solid angle “seen” by the microscope objective. Solid angle given by $\theta < \theta_{max}$, where $\theta_{max} = \arcsin(\text{NA}/n_1)$ for collection from beyond the slide and $\theta > \pi - \theta_{max}$, for detection from above the slide. Numerical results are shown for three different configurations. Solid line: collection with a 1.45 NA oil-immersion objective from beyond (objective-type TIRF); dashed line: collection with a 1.15 NA water-immersion objective from beyond (confocal); dotted line: collection with a 1.15 NA water-immersion objective from above (prism-type TIRF).

The function $P(z)$ is represented in Fig. 6.4. Three basic configurations, prism-type, confocal and objective-type are shown. The numerical apertures of the microscope objectives were assumed to equal 1.45 for objective-type and 1.15 (water-immersion) for the other configurations. The collection efficiency for the objective-type configuration close to the interface exceeds 60%, which is about two times higher than for the other configurations. This theoretical result shows clearly one main advantage of the objective-type TIR configuration.

6.2.3 Background suppression

Although modern dichroic mirrors and interference filter suppress background very efficiently, a small fraction of excitation light will still reach the detector. In objective-type TIR-FCS as well as in confocal FCS, when applied to measure on a glass surface, the incident beam is back-reflected towards the detector. To completely suppress the back-reflected light we introduced a lens L4 at a distance $2f$ after the microscopes image plane (see Fig. 6.1). As before, light emitted from a point-source in the object plane is efficiently focused onto the second image plane, IP2, and collected. Because the reflected beam is not collimated after traversing the objective, the focus of the reflected light is situated at some distance in front of the plane IP2. By introducing an optical obstacle at this focus position, the portion of reflected light that traverses the emission filter and dichroic mirror can be efficiently suppressed. The size of the optical obstruction can be in the order of the focus diameter. Because the beam diameter of fluorescence light is wide in the plane where the obstruction is situated, the collection efficiency remains almost unaltered.

We used a cover slide with a localized circular metal-coating of about 0.5 mm diameter as a spatial filter. The filter was mounted on a xy -translation table with 10 μm precision for superimposing the obstruction with the coating. To estimate the influence on the collection

efficiency, FCS measurements on a 50 nM solution of Rh6G in water were performed and the count rates per molecule (CPM) calculated using $\text{CPM} = \langle R \rangle / \langle N \rangle$, where $\langle R \rangle$ is the mean total count rate and $\langle N \rangle$ the mean number of molecules in the observation volume. Measurements were performed for the same sample in the two different configurations (fiber-end in plane IP1 and in plane IP2). No influence of the additional optical elements on the CPM could be observed. To estimate the effect on the background we performed measurements on pure (double-distilled) water in the two configurations. We determined a gain in the signal-to-background ratio in the order of 15%. We concluded that the main contribution to the background was due to Raman scattered light and probably most important, autofluorescence of optical components. Therefore, in most of our experiments, we did not make use of spatial background filtering.

6.2.4 Molecule detection efficiency

In paper III, the results from numerical calculations of the molecular detection efficiency for confocal FCS and objective-type TIR-FCS are presented. The influence of the dielectric interface was approximately taken into account by multiplying the collection efficiency function, $\text{CEF}(\mathbf{r})$, with a function $P(z)$. This function is the fraction of power emitted by a randomly oriented dipole into the solid angle seen by the objective, discussed above. The modified CEF therefore reads (compare with Eq. 4.6):

$$\text{CEF}(\mathbf{r}) = \frac{P(z)}{\Delta} \int_S \text{circ}(\mathbf{r}'/\rho) \text{PSF}(\mathbf{r} - \mathbf{r}', z) dx dy, \quad (6.8)$$

Definitions of the symbols are provided in the discussion of Eq. 4.6. The PSF was calculated according to the approach of B. Richards and E. Wolf [95], where we averaged over all possible dipole orientations. The CEF was used to calculate the MDE according to Eq. 4.5 with $I(z)$ given by Eq. 5.3, where we assumed a penetration depth of $d = 72$ nm (see above). The MDE for TIR-FCS obtained for a pinhole diameter of $50 \mu\text{m}$ is shown in Fig. 6.5.

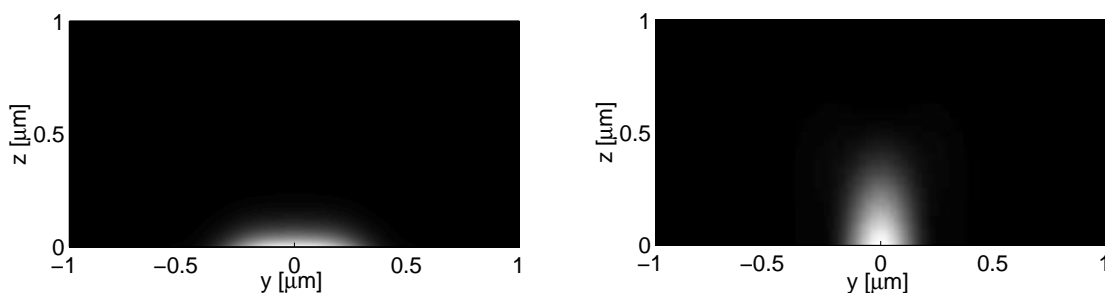


Figure 6.5: The MDEs for objective-type TIR-FCS (left) and confocal FCS (right). The observation volume for objective-type TIR-FCS is confined to the surface, whereas it reaches far into the solution for the confocal configuration. For details on the calculations see text.

We compared this function to the MDE obtained for confocal FCS, where we assumed the use of a $40\times$ water immersion objective with 1.15 NA (Fig. 6.5, right side). In this case the intensity distribution was approximated by the PSF of the optical detection system for the excitation wavelength (here, 488 nm).

In the limit of a point shaped pinhole ($a \rightarrow 0$) we have $\text{MDE} \propto \text{PSF}^2$ for confocal FCS whereas in the case of TIR-FCS, at least at the surface, $\text{MDE}|_{z=0} \propto \text{PSF}|_{z=0}$. For this reason it is no surprise that the lateral confinement is higher for the confocal configuration than for the TIR-FCS configuration. In TIR-FCS, the larger lateral extend of the MDE is more than

compensated by the smaller axial extend and the size of the observation volume is about a factor of 1.5 smaller as is shown below.

We calculated the size of the observation volume in terms of the W_1 and the effective volume by numerically integrating the MDEs. We obtained

$$\begin{aligned} W_1^C &= 26 \text{ al} & V_{eff}^C &= 134 \text{ al} \\ W_1^T &= 17 \text{ al} & V_{eff}^T &= 57 \text{ al} \end{aligned}$$

The subscripts C and T denote the confocal case and the TIRF case respectively. The difference in the size of the observation volumes is not large and does on its own not constitute a big benefit when using the objective-type TIR approach. The advantage of TIR-FCS is rather related to the difference in the shapes of the MDEs. As is evident from Fig. 6.5, TIR-FCS favors the detection of signals originating at the surface, which is an incontestable advantage if the studied biomolecular system is confined to the surface.

For the purpose of deriving analytical autocorrelation functions we approximate the MDE by

$$\text{MDE}(\mathbf{r}) = \text{MDE}(0) \exp\left(-\frac{2\rho^2}{\omega_{xy}^2}\right) \exp\left(-\frac{z}{h}\right), \quad (6.9)$$

where $\rho = \sqrt{x^2 + y^2}$. The real ρ -dependence is given by an airy function and the above approximation may appear quite rough. However, the autocorrelation functions that were derived using the above approximation were successfully used to analyze real data sets, which justifies this choice (see 7).

In FCS there is some arbitrariness in defining the number of molecules in the observation volume, since this volume (or the MDE) is actually not limited in space but extends to infinity. Here and in the following we define $\langle N \rangle$ as the number of molecules in the W_1 volume. As was shown in chapter 4, the zero time correlation is related to the mean concentration, $\langle C \rangle$ by

$$G(0) - 1 = \frac{\gamma}{\langle N \rangle}, \quad (6.10)$$

where $\langle N \rangle$ is the mean number of molecules in the observation volume. This definition differs from the common definition, where the observation volume is defined to equal the effective volume, V_{eff} . A particular choice obviously does not influence the estimates of most of the physically relevant parameters, e.g. concentration, diffusion time or triplet time. The proposed definition, however, leads to an estimate of the maximum count rate per molecule, CPM, which can be easily seen by considering that the CPM for a molecule at position \mathbf{r} is

$$\text{CPM}(\mathbf{r}) = a \frac{\sigma \Phi_F \text{MDE}(\mathbf{r})}{\hbar \nu}. \quad (6.11)$$

Here, σ denotes the excitation cross section, Φ_F the fluorescence quantum yield of the fluorophore, ν the frequency of the emitted light and a is a constant. The mean total fluorescence count rate $\langle R \rangle$ is given by

$$\langle R \rangle = a \langle C \rangle \frac{\sigma \Phi_F}{\hbar \nu} \int_V \text{MDE}(\mathbf{r}) d^3r \quad (6.12)$$

If $\langle N \rangle$ is defined as the mean number of molecules in the W_1 volume, $\langle N \rangle \equiv W_1 \langle C \rangle$, than

$$\frac{\langle R \rangle}{\langle N \rangle} = \frac{a \sigma \Phi_F \text{MDE}(0)}{\hbar \nu} = \text{CPM}(0). \quad (6.13)$$

This is the maximum CPM, reached by fluorophores residing at the surface, in the center of the observation volume. The maximal CPM has in the present context more significance than an

average value. That's because for investigations of single molecule kinetics of binding molecules, proper alignment of the fiber-end presumed, the signal providing fluorophores are supposed to be situated where the MDE has its maximum, hence the observed CPM is anyway maximal.

For this definition of $\langle N \rangle$, the correction factor equals $\gamma = W_2/W_1$, which follows from Eqs. 6.10, 4.4 for $\tau = 0$ and 4.10. By substituting 6.9 into equation 4.10 we get $\gamma = 1/4$ for this particular setup. In the case of confocal FCS, γ equals $1/2^{3/2}$ in theory.

Chapter 7

Diffusion studies

As a first application we used objective-type TIR-FCS to measure diffusion of dye molecules. The intention of these measurements was not to investigate the process of diffusion but rather to use it as a tool to investigate the characteristics of the TIR-FCS system. In particular we could estimate the evanescent field-depth and the count rates per molecule in this way (see section 7.2). In order to analyze the autocorrelation data quantitatively, we derived the theoretical form of the autocorrelation function $G(\tau)$ for objective-type TIR-FCS, assuming single-component diffusion combined with triplet-kinetics. The concise derivation will be presented in the following.

7.1 Derivation of the autocorrelation function for diffusion

We assume that the diffusing particles do not bind to the surface, or in other words, that the flux normal to the interface equals zero at the interface. This derivation of the autocorrelation function differs from a derivation in [96] as here we take triplet kinetics into account, the molecular detection efficiency (MDE) function is modeled as a Gauss function in the xy -plane, but binding to the surface is not considered. It appeared to be necessary to include the first two considerations when deriving $G(\tau)$ in order to meet our experimental conditions.

From Eq. 4.4 we get

$$G(\tau) = 1 + \frac{\int_{\Omega} \int_{\Omega} \text{MDE}(\mathbf{r}) \text{MDE}(\mathbf{r}') \phi(\mathbf{r}, \mathbf{r}', \tau) d^3r d^3r'}{(\langle C \rangle \int_{\Omega} \text{MDE}(\mathbf{r}) d^3r)^2}, \quad (7.1)$$

with $\phi(\mathbf{r}, \mathbf{r}', \tau) \equiv \langle \delta C(\mathbf{r}, \tau) \delta C(\mathbf{r}', 0) \rangle$ as before and $\delta C(\mathbf{r}, \tau) \equiv \langle C \rangle - C(\mathbf{r}, \tau)$, where $C(\mathbf{r}, \tau)$ is the concentration of fluorophores that are not in the triplet state.

The symbol Ω stands for the positive half-space $z \geq 0$. As in chapter 4 we assume that the mean concentration, $\langle C \rangle$, is independent from \mathbf{r} .

To simplify the following calculations, we will first consider 'pure' diffusion, that is to say we assume that no molecules are in the triplet state. The Einstein diffusion equation written for the concentration fluctuations reads

$$\frac{\partial}{\partial \tau} \phi(\mathbf{r}, \mathbf{r}', \tau) = D \nabla_{\mathbf{r}}^2 \phi(\mathbf{r}, \mathbf{r}', \tau) \quad (7.2)$$

with the initial condition

$$\phi(\mathbf{r}, \mathbf{r}', 0) = \langle C \rangle \delta(\mathbf{r} - \mathbf{r}'). \quad (7.3)$$

For finite \mathbf{r}' and τ the boundary conditions are

$$D \left[\frac{\partial}{\partial z} \phi(\mathbf{r}, \mathbf{r}', \tau) \right]_{z=0} = 0 \quad \text{and} \quad [\phi(\mathbf{r}, \mathbf{r}', \tau)]_{|\mathbf{r}| \rightarrow \infty} = 0. \quad (7.4)$$

The above set of equations describes diffusion in the positive half-space, for $z, z' \geq 0$. The first boundary condition states that the component of the particle flux, $\mathbf{j}(\mathbf{r}, \tau) = D\nabla C(\mathbf{r}, \tau)$, normal to the interface is zero at $z = 0$. This is equivalent to state that molecules do not bind to the surface or in other words that no sinks or sources are found at the surface.

The solution is given by a convolution of the Green's function (Eq. 4.18) with the initial conditions, as is explained in chapter 4. In the present case, initial conditions are only defined in the positive half-space. This gives us the liberty to introduce a further constraint for $\tau = 0$ in the negative half-space in order to match the boundary condition at $z = 0$. The condition that does the trick equals Eq. 7.3 with z substituted by $-z$. Convoluting the $\phi_G(\mathbf{r}, \mathbf{r}', \tau)$ with the initial conditions yields

$$\begin{aligned} \phi(\mathbf{r}, \mathbf{r}', \tau) &= \frac{\langle C \rangle}{(4\pi D\tau)^{3/2}} \exp\left(-\frac{|\boldsymbol{\rho} - \boldsymbol{\rho}'|^2}{4D\tau}\right) \\ &\times \left[\exp\left(-\frac{(z - z')^2}{4D\tau}\right) + \exp\left(-\frac{(z + z')^2}{4D\tau}\right) \right]. \end{aligned} \quad (7.5)$$

Vectors in a plane $z = \text{const.}$ are denoted by $\boldsymbol{\rho}$.

Substituting the analytical expression for the MDE given by Eq. 6.9 and the solution 7.5 into equation 7.1 and integrating yields

$$G(\tau) = 1 + \frac{\gamma}{\langle N \rangle} \left(1 + \frac{\omega^2 \tau}{\tau_z}\right)^{-1} \left[\left(1 - \frac{\tau}{2\tau_z}\right) w\left(i\sqrt{\frac{\tau}{4\tau_z}}\right) + \sqrt{\frac{\tau}{\pi\tau_z}} \right]. \quad (7.6)$$

The function w is the complex generalization of the error function, which is defined as

$$w \equiv \exp(x^2) \operatorname{erfc}(-ix), \quad (7.7)$$

where erfc is the complementary error function. The axial diffusion time τ_z is related to the diffusion coefficient D by $\tau_z = h^2/(4D)$. The parameter h describes the axial extent of the MDE (Eq. 6.9). ω denotes the structure parameter, defined as $\omega \equiv h/\omega_{xy}$. If in the above equation $\omega \rightarrow \infty$, we recover the limiting result for pure diffusion presented by Starr et al. in [96].

In order to derive an autocorrelation function that takes intersystem crossing (triplet kinetics) into account, we proceed in the same way as outlined in chapter 4. We find

$$\begin{aligned} G_T(\tau) &= 1 + \frac{\gamma}{\langle N \rangle} \left[1 + \frac{p}{1-p} \exp\left(-\frac{\tau}{\tau_T}\right) \right] \\ &\times \left(1 + \frac{\omega^2 \tau}{\tau_z}\right)^{-1} \left[\left(1 - \frac{\tau}{2\tau_z}\right) w\left(i\sqrt{\frac{\tau}{4\tau_z}}\right) + \sqrt{\frac{\tau}{\pi\tau_z}} \right]. \end{aligned} \quad (7.8)$$

7.2 Measurements and data analysis

In order to test the applicability of our setup and our model for $G(\tau)$ we performed measurements for dye molecules diffusing above a microscope cover slide. The measurements described in the following are summarized in papers II and III. Preliminary measurements using a rhodamine dye (rhodamine green) produced unsatisfactory results because rhodamine dyes are prone to stick to the cover slide surface. This problem was solved by using the dye fluorescein. However, the count-rate per molecule that could be obtained with this fluorophore was relatively low, which resulted in a low signal to background ratio. For this reason, the used concentration had to be higher than 5 nM. An upper limit for the usable concentration of about 1 μM existed for our setup. This was due to a sinusoidal variation of the laser output intensity of about 50 Hz with

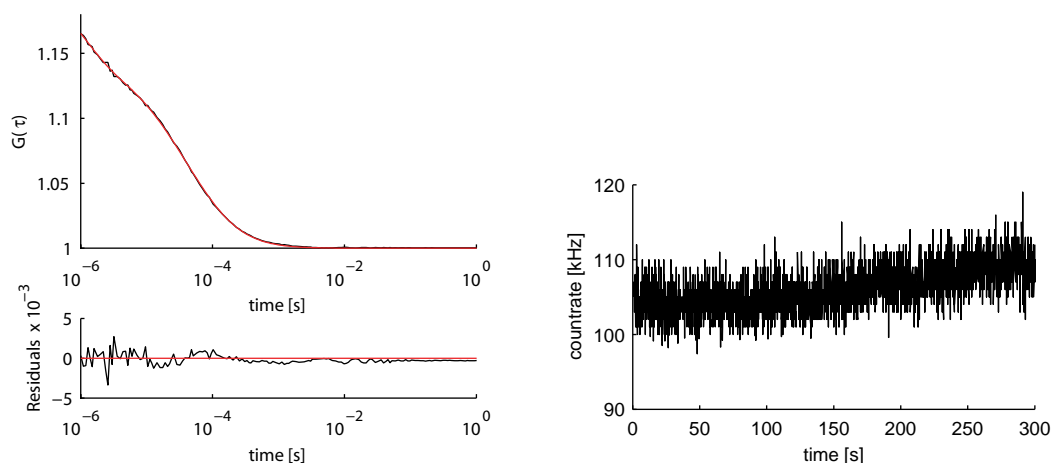


Figure 7.1: Left: FCS curve for freely diffusing fluorophores. Estimated parameters: $N = 1.67$, $\tau_z = 4.89 \mu\text{s}$, $p = 28.7\%$, $\tau_T = 1.08 \mu\text{s}$, $\omega = 0.197$. Right: corresponding time trace.

a modulation depth of 5%. For high fluorophore concentration the correlation of the sinusoidal intensity variation becomes the dominant contribution in the FCS curve.

Figure 7.1 shows a typical autocorrelation curve and time trace obtained for the dye carboxy fluorescein (10 nM in buffer, pH 8), and a measurement time of 5 min. Fluorescence was excited using the blue line (at 488 nm) of the argon laser. We estimated the intensity in water, at the interface to equal $60 \mu\text{W}$. The fit was performed with a MATLAB routine based on a global search algorithm, using the model presented in Eq. 7.8. An analysis of the residuals shows that the autocorrelation decreases below 1 for large correlation times. This is due to an increase of the overall fluorescence intensity with measurement time. Most probably the increase in intensity is caused by evaporation of the buffer solution during the 5 min measurement time resulting in a rise of the fluorophore concentration. In the interval $[10^{-2}\text{s}, 5 \times 10^{-2}\text{s}]$ a sinusoidal oscillation is discernable, which is caused by the modulation of the laser intensity. A further deviation of the model can be observed for smaller times. We assume that the deviations are due to some adsorption of the dyes to the surface, an effect that is not accounted for by our model.

In general, reasonable parameter estimates could be obtained for concentration, N , diffusion time, τ_z , structure parameter, ω , triplet fraction, p , and triplet time, τ_T without the need of fixing any of those parameters. In a series of 10 measurements (10s measurement time each), we obtained the following estimates with corresponding standard deviation, s ,

$$\begin{aligned}
 \bar{\omega} &= 0.19 & s_{\omega} &= 0.04 \\
 \bar{\tau}_z &= 5.39 \mu\text{s} & s_{\tau_z} &= 0.98 \mu\text{s} \\
 \bar{\tau}_T &= 0.84 \mu\text{s} & s_{\tau_T} &= 0.17 \mu\text{s} \\
 D &= (1.90 \pm 0.12) \times 10^{-6} \text{ cm}^2 \text{ s}^{-1}
 \end{aligned}$$

The estimation of the structure parameter is in good agreement with the value obtained by alternative means¹. The diffusion coefficient D derived from the mean diffusion time $\bar{\tau}_z$ using

¹For comparison we derived ω from the numerically calculated MDE and obtained a structure parameter of $\omega = 0.17$. In the calculations we used an estimated evanescent field depth, obtained by measuring the incidence angle. In this way we obtained a field depth $d = 72 \text{ nm}$. The MDE was then calculated using the derived d . By measuring the positions at which the MDE drops to e^{-2} and e^{-1} for ω and z , respectively, the structure parameter was obtained. The uncertainty in ω stems mainly from an uncertainty in the measurement of the angle; the maximal error $\Delta\omega/\omega$ was estimated to equal approximately 10%.

$D = h^2/(4\tau_z)$, where h is the distance at which the MDE drops to e^{-1} , is in good agreement with previously published values [97]. The error in D is a lower bound, derived from the variance in τ_z and the estimated error in deriving h . The uncertainty in deriving h was estimated from the error in measuring the angle of incidence at the cover slide. However, other sources that may increase the uncertainty in h , as e.g. light scattering at the interface, have not been considered.

To show the performance of the present system in terms of count rate per molecule and signal-to-background ratio we realized diffusion measurements for the dye Rh6G. Results are discussed in detail for a typical measurement in paper III. These measurements were performed at the maximal available laser power of our system (20 to 22 mW) at a still tolerable fraction of molecules in the triplet state ($p < 17\%$). A very high count rate of 1.8 MHz and a signal to background ratio of 39 could be inferred from the data.

The experiments presented above were performed with a fiber core diameter of 50 μm . Several measurement series were performed for different fiber core diameters (see paper III), for two reasons. Firstly, to determine the optimal configuration in terms of signal-to-background ratio. Secondly, to check if our approximation of the MDE used for the derivation of $G(\tau)$ considerably affects the estimation of parameters. For increasing pinhole diameters the intersection of the MDE with the xy -plane tends towards a rectangular shape and the approximation by a Gauss function becomes less valid (see Fig. 7.2). In conclusion, parameter estimates were in a reasonable

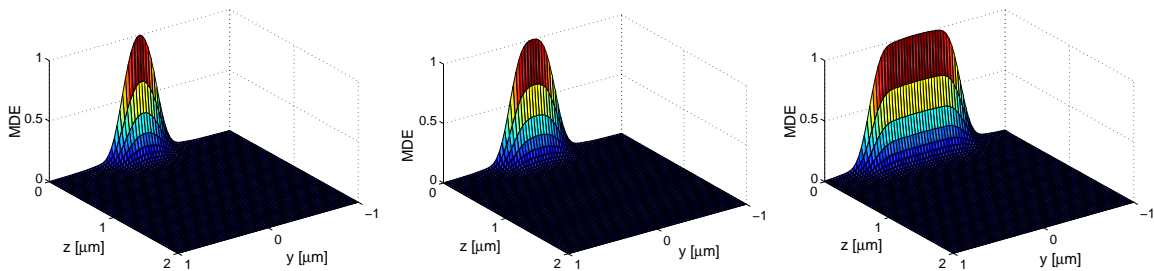


Figure 7.2: The MDEs for three different pinhole diameters. Left: 37.5 μm ; middle: 50 μm ; right: 100 μm .

range using fiber core diameters of 37.5 μm , 50 μm and 100 μm . Only when using a pinhole diameter of 100 μm in which case the approximation for the MDE becomes apparently bad (see Fig. 7.2), the estimate for τ_z changed by $\sim 20\%$ (see paper III). In principle τ_z should of course not change because the pinhole diameter has no influence on h .

diam. [μm]	γ	W_1 [al]	N	C [nM]	CPM [kHz]	b [kHz]	SBR
37.5	0.2551	11.9	4.06 ± 0.21	599 ± 31	39.1 ± 1.3	2.0	19.55 ± 0.65
50	0.2942	16.9	6.51 ± 0.23	640 ± 23	48.1 ± 1.1	3.3	14.44 ± 0.32
100	0.3917	57.3	30.2 ± 6.3	932 ± 195	47.4 ± 5.3	12.2	3.87 ± 0.43

Table 7.1: Parameter estimates for measurements with different pinhole diameters (first column). The values for γ and W_1 were obtained by numerical integration of the MDE. (MDE calculated in the range $0 \leq r \leq 1 \mu\text{m}$, $0 \leq z \leq 2 \mu\text{m}$ on a grid of 257×257 points.) The estimate of the concentration, C , is given by $C = N/W_1$. Mean values were obtained from three measurements, each recorded for a measurement time of thirty seconds. Errors are standard deviations of the mean.

Using a smaller pinhole diameter resulted in a higher signal to background ratio, where signal is understood as count rate per molecule and background as the mean count-rate when pure buffer was used instead of a fluorophore solution. The signal to background ratio could be increased by approximately 30% when using a 37.5 μm instead of a 50 μm fiber core. Mea-

surement results are summarized in table 7.1. Here, the concentrations were calculated using the listed γ -factors. With increasing pinhole diameter, this parameter comes close to the value calculated from the analytical approximation of the MDE (see Eq. 6.9), which equals $1/4$. Other aspects of the same series of measurements are discussed in paper III.

Chapter 8

Binding studies

The signaling processes of cells are mediated by the interaction of ligands (e.g. neurotransmitters or hormones) with receptors on the cell membrane or within the cytoplasm or the nucleus [98]. The sensitivity and specificity of the initiation of signaling cascades depends primarily on the equilibrium strength of the associated ligand-receptor interaction. It has been hypothesized that for a lot of cellular signaling processes the average lifetime of the receptor-ligand compound or the compounds dissociation rate may moreover play a role [99, 100]. In order to better understand and dissect the different factors influencing the efficiency of cellular signaling it is important to be able to accurately measure the association and dissociation rates for receptor-ligand interaction. A. Lieto et al. [87] showed that TIR-FCS is an excellent tool to measure dissociation rates. Other groups were successful in measuring kinetic rates for adsorption and desorption [84, 101] using TIR-FCS. These promising results and the idea to improve the sensitivity of the existing technology became strong motivations to develop objective-type TIR-FCS. During the development process, the question arose if our technique is sensitive enough to investigate molecular kinetics and dynamics on a real single molecule level. That is to say, can we obtain the autocorrelation for successive events (e.g. binding and release) stemming from one and the same immobilized (receptor) molecule? Preliminary measurements on diffusing molecules showed indirectly that the obtainable signal to background ratio should be high enough (see chapter 7). In this chapter experimental results will be presented that evidence directly the applicability of objective-type TIR-FCS for investigating binding kinetics on a single molecule level. To quantitatively analyze the data obtained in such a kind of experiments the autocorrelation function, $G(\tau)$, for combined diffusion and binding to a single, localized receptor was derived. The derivation of $G(\tau)$ was carried out for the case of TIR-FCS and its special observation volume, but the result can be easily generalized to hold for different observation volumes and in particular for confocal FCS.

8.1 Derivation of the autocorrelation function for binding kinetics

T.E. Starr et al. [96] derived the exact form of the autocorrelation function for TIR-FCS in the case of combined diffusion and reversible binding. However, in their work they considered a homogeneous surface such that ligands can bind everywhere with association and dissociation constants that are independent of position. Hence, their model covers rather situations of unspecific adsorption to the surface and desorption.

The autocorrelation function presented in the following corresponds to a situation where a single, small receptor is located at position \mathbf{r}_0 . To simplify matters we assume that \mathbf{r}_0 is

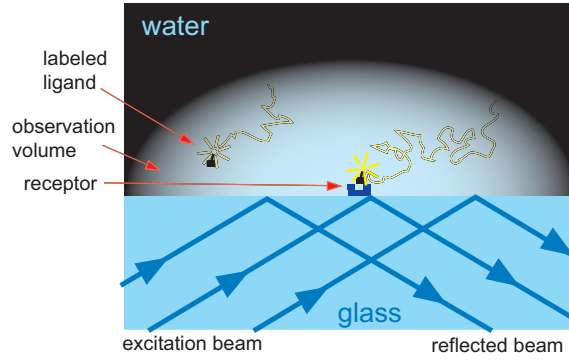


Figure 8.1: Scheme explaining the physical model that constitutes the base for the derivation of $G(\tau)$. Fluorescently labeled ligands diffuse through the observation volume, which is large compared to a receptor immobilized on the surface in the center of the MDE (on the optical axis). Binding may occur at the receptor but not elsewhere (reflective boundary conditions at the surface, at $\mathbf{r} \neq 0$).

situated at the center of the observation volume, that is to say $\mathbf{r}_0 = 0 = (0, 0, 0)$, (see Fig. 8.1). The model can be easily generalized for several receptors at different locations. To get a simple analytical form of $G(\tau)$ we considered only the case where the association and dissociation rates are small compared to the inverse diffusion time. This condition is satisfied for many interesting receptor-ligand systems. In contrast to the work of Starr et al., triplet kinetics and the finite lateral extend of the observation volume is taken into account in the present derivation.

The differential equations describing this situation are

$$\frac{\partial}{\partial t} C(\mathbf{r}, t) = D \nabla^2 C(\mathbf{r}, t) - \delta(\mathbf{r}) \frac{d}{dt} n(t), \quad (8.1)$$

$$\frac{d}{dt} n(t) = k_+ C(0, t) [1 - n(t)] - k_- n(t). \quad (8.2)$$

We disregard triplet kinetics at present. The rate constants for association and dissociation are k_+ and k_- , respectively. The probability that the receptor is occupied at time t or in other words the fractional occupancy is denoted by $n(t)$; $C(\mathbf{r}, t)$ is the local concentration of free ligands. The presence of the receptor results in a source term localized at $\mathbf{r} = 0$. Instead of explicitly stating reflective boundary conditions at the surface for $\mathbf{r} \neq 0$, we extend the domain of the differential equations to the lower half-space $z < 0$ and modify the MDE (from Eq. 6.9), to read

$$\text{MDE}(\mathbf{r}) = \text{MDE}_0 \exp\left(-2 \frac{x^2 - y^2}{\omega_{xy}^2}\right) \exp\left(-\frac{|z|}{h}\right). \quad (8.3)$$

The reflective boundary conditions discussed in chapter 7 (Eq. 7.4) assure that every particle arriving at $z = 0$ is immediately reflected back into the upper half-space. In the above approach the observation volume is reflected at $z = 0$ instead, which is mathematically equivalent.

By taking the average of Eq. 8.2 we derive the equilibrium condition

$$k_+ \langle C \rangle (1 - \langle n \rangle) = k_- \langle n \rangle. \quad (8.4)$$

Here, we used that $\langle n \rangle$ and $\langle C \rangle$ are independent of time. It was further used that the concentrations for bound and free molecules are uncorrelated at the same time. After rewriting the differential equations for the deviations from the mean values, $\delta C(\mathbf{r}, t)$ and $\delta n(t) = n(t) - \langle n \rangle$, making use of the equilibrium condition and neglecting terms that are second order in δn or δC ,

we obtain the following set of equations [63]

$$\frac{\partial}{\partial t} \delta C(\mathbf{r}, t) = D \nabla^2 \delta C(\mathbf{r}, t) - \delta(\mathbf{r}) \frac{d}{dt} \delta n(t), \quad (8.5)$$

$$\frac{d}{dt} \delta n(t) = -R \delta n(t) + k_+(1 - \langle n \rangle) \delta C(0, t). \quad (8.6)$$

The factor R is called the *reaction rate* and is defined as: $R \equiv \langle C \rangle k_+ + k_-$. Instead of trying to solve this system of differential equations in real space, we will Fourier transform the equations with respect to spatial coordinates and Laplace transform with respect to time. The transformed equations are

$$\delta \tilde{n}(s) = \frac{1}{s + R} \left[\delta n(0) + k_+(1 - \langle n \rangle) \delta \tilde{C}(\mathbf{r} = 0, s) \right], \quad (8.7)$$

$$\delta \tilde{C}(\mathbf{q}, s) = \frac{1}{s + \mathbf{q}^2 D} \left[\delta \tilde{C}(\mathbf{q}, t = 0) + \frac{\delta n(0)}{(2\pi)^{3/2}} - \frac{s \delta \tilde{n}(s)}{(2\pi)^{3/2}} \right]. \quad (8.8)$$

The tilde indicates a Laplace and/or Fourier transformed function. The position vector in Fourier space is denoted by \mathbf{q} and the variable in Laplace space is s . The Laplace transform leads directly to the general solution in terms of the initial values $\delta n(0)$ and $\delta \tilde{C}(\mathbf{q}, t = 0)$. At present, however, we still need to express the function $\delta \tilde{C}(\mathbf{r} = 0, s)$ in terms of the initial values. This is realized by taking the inverse Fourier transform of Eq. 8.8 and setting $\mathbf{r} = 0$. By proceeding as stated we get

$$\delta \tilde{C}(\mathbf{r} = 0, s) = \Theta(s) - [s \delta \tilde{n}(s) - \delta n(0)] \Sigma(s), \quad (8.9)$$

with

$$\Theta(s) \equiv \frac{1}{(2\pi)^{3/2}} \int_{\tilde{\Omega}} \frac{\delta \tilde{C}(\mathbf{q}, t = 0)}{s + \mathbf{q}^2 D} d^3 q, \quad (8.10)$$

$$\Sigma(s) \equiv \frac{1}{(2\pi)^{3/2}} \int_{\tilde{\Omega}} \frac{d^3 q}{s + \mathbf{q}^2 D}. \quad (8.11)$$

The function $\Sigma(s)$ is infinite for all $s < \infty$. This is due to the interpretation of the receptor as a point source, or in other words, the delta function in Eq. 8.1. A physical receptor has some non-zero size, say a diameter $a > 0$. In a simplified picture, every ligand that approaches the receptor to a distance $|\mathbf{r}| \leq a$ binds to the receptor. This can be taken into account by integrating in Eqs. 8.10 and 8.11 not over the whole space $\tilde{\Omega}$ but to some large, but finite radius $\Lambda \sim 1/a$ [63]. As here we are not interested in dynamic or kinetic processes taking place on time-scales much smaller than the diffusion time through the observation volume, τ_z , we do not need to consider frequencies $s \gg 1/\tau_z$. In fact, the contribution of large s to $G(\tau)$ for $\tau > \tau_z$ is negligible; in other words, when calculating $\delta n(t)$ and $\delta C(\mathbf{r}, t)$ from Eqs. 8.7 and 8.8 we can cut the inverse Laplace transform at some maximum $s_{max} \sim 1/\tau_z$. Because $\tau_z = h^2/(4D)$ and $a \ll h$ frequencies in the range of interest satisfy $s < s_{max} \ll 4D/a^2$. As a consequence we may approximate $\Sigma(s)$ by $\Sigma(0)$. This can be seen by explicitly calculating the integral in Eq. 8.11 in the limit $|\mathbf{q}| \leq 1/a$. We can rewrite Eq. 8.7 to get

$$\delta \tilde{n}(s) = \frac{1}{s + R'} [\delta n(0) + \alpha \Theta(s)], \quad (8.12)$$

where we introduced a new reaction rate, R' , and a constant α defined as

$$R' \equiv \frac{R}{[1 + k_+(1 - \langle n \rangle) \Sigma(0)]} \quad \text{and} \quad (8.13)$$

$$\alpha \equiv \frac{k_+(1 - \langle n \rangle)}{1 + k_+(1 - \langle n \rangle) \Sigma(0)} \quad (8.14)$$

Like already stated in chapter 4, the autocorrelation function is a sum of auto- and cross-correlation terms of different species. In the present case these are bound and freely diffusing molecules. Rewriting Eq. 4.4, using that the concentration of bound molecules is just $\delta(\mathbf{r}) n(t)$ and assuming that the molecular brightness does not change upon binding yields

$$G(\tau) = 1 + \sum_{k=0}^1 \sum_{l=0}^1 \frac{G'_{kl}(\tau)}{(\langle C \rangle W_1 + \langle n \rangle)^2}. \quad (8.15)$$

The $G'_{kl}(\tau)$ written in terms of the transformed functions $\delta\tilde{n}$ and $\delta\tilde{C}$ read

$$G'_{00}(\tau) = \mathcal{L}^{-1} \{ \langle \delta\tilde{n}(s) \delta n(0) \rangle \} (\tau), \quad (8.16)$$

$$G'_{01}(\tau) = \int_{\Omega'} \text{MDE}(\mathbf{r}') \mathcal{L}^{-1} \{ \langle \delta\tilde{n}(s) \delta C(\mathbf{r}', 0) \rangle \} (\tau) d^3 r', \quad (8.17)$$

$$G'_{10}(\tau) = \int_{\Omega} \text{MDE}(\mathbf{r}) \mathcal{F}^{-1} \left\{ \mathcal{L}^{-1} \{ \langle \delta\tilde{C}(\mathbf{q}, s) \delta n(0) \rangle \} (\tau) \right\} (\mathbf{r}) d^3 r, \quad (8.18)$$

$$G'_{11}(\tau) = \int_{\Omega} \int_{\Omega'} \text{MDE}(\mathbf{r}) \text{MDE}(\mathbf{r}') \mathcal{F}^{-1} \left\{ \mathcal{L}^{-1} \{ \langle \delta\tilde{C}(\mathbf{q}, s) \delta C(\mathbf{r}', 0) \rangle \} (\tau) \right\} (\mathbf{r}) d^3 r d^3 r'. \quad (8.19)$$

The above equations are easily obtained by using Eq. 4.4, taking into account that the bound ligands are localized at $\mathbf{r} = 0$. We used further that the inverse Laplace- or Fourier transformation (denoted by \mathcal{L}^{-1} and \mathcal{F}^{-1} , respectively) can be interchanged with the operation of taking the average. It appears that we take the average of the product of two functions, which, at a first glance, may look like a pointlessness. However, one should keep in mind that the $\delta\tilde{n}(s)$ and $\delta\tilde{C}(\mathbf{q}, s)$ are the general solutions of the differential equations Eqs. 8.8 and 8.12. Actually, the initial values $\delta C(\mathbf{r}, 0)$ and $\delta n(0)$ are not fixed but interpreted as random variables. Therefore, the operation $\langle \cdot \rangle$ in Eqs. 8.16 to 8.19 does not act on analytical functions with fixed parameters, which indeed would be pointless, but on the random initial values.

At present, we still lack the auto- and cross-correlations of the concentration fluctuations at time $\tau = 0$ in order to obtain $G(\tau)$ in a closed, analytical form. Auto- and cross-correlations for diffusing molecules are easily obtained by assuming ideality of the solution, following the argumentation in chapter 4. The autocorrelation of $n(0)$ at $\tau = 0$ is the variance of a random variable that take values 1 and 0 with probabilities $\langle n \rangle$ and $(1 - \langle n \rangle)$, respectively. Using basic statistical mathematics we obtain

$$\langle \delta n(0) \delta n(0) \rangle = \langle n \rangle (1 - \langle n \rangle), \quad (8.20)$$

$$\langle \delta n(0) \delta C(\mathbf{r}, 0) \rangle = \langle \delta C(\mathbf{r}, 0) \delta n(0) \rangle = 0, \quad (8.21)$$

$$\langle \delta C(\mathbf{r}, 0) \delta C(\mathbf{r}', 0) \rangle = \langle C \rangle \delta(\mathbf{r} - \mathbf{r}'). \quad (8.22)$$

Hereafter we will refer to this set of equations as the initial conditions.

We will now investigate the different functions G'_{kl} one by one beginning by G'_{00} . Substituting $\delta\tilde{n}(s)$ from Eq. 8.12 into Eq. 8.16 and making use of the initial conditions we obtain after inverse Laplace transformation

$$G'_{00} = \langle n \rangle (1 - \langle n \rangle) e^{-R' \tau}. \quad (8.23)$$

Interestingly, the deviation from equilibrium does not relax with the reaction rate but with R' . The modification in the relaxation rate is a direct consequence of the discreteness of the binding site and stems mathematically from the localization of the source term in Eq. 8.1. This constitutes the main difference to the case of unspecific adsorption as e.g. treated in [96, 26]. In this simplified description we are not able to derive the exact relationship between R and R' but we are able to give a first approximation. Carrying out the integration in Eq. 8.10 up

to the radius Λ , we obtain $\Sigma(0) = 4\pi/(aD)$. This is of course a crude approximation for $\Sigma(0)$, which depends on the exact geometry of the binding site. It can further be shown that for an absorbing disk of radius a the association rate is related to the diffusion coefficient by $k_+ = 4Da$ [102, 103]. Using this relation and inserting the approximation for $\Sigma(0)$ into the definition of R' (Eq. 8.13) we get a R' that is smaller than R but in the same order. However, the difference may not be negligible.

We proceed in the derivation of $G(\tau)$ and calculate the cross-correlation terms $G'_{01}(\tau)$ and $G'_{10}(\tau)$. Using the initial conditions we get

$$\begin{aligned} \left\langle \delta\tilde{C}(\mathbf{q}, t=0) \delta C(\mathbf{r}', 0) \right\rangle &= \mathcal{F}\{\delta(\mathbf{r} - \mathbf{r}')\}(\mathbf{q}') \\ &= \frac{e^{-i\mathbf{q}\cdot\mathbf{r}'}}{(2\pi)^{3/2}}. \end{aligned} \quad (8.24)$$

By inserting $\delta\tilde{n}(s)$ from Eq. 8.12 into Eq. 8.15 and using Eq. 8.24 we derive

$$G'_{01}(\tau) = \langle C \rangle \frac{\alpha}{(2\pi)^{3/2}} \mathcal{L}^{-1} \left\{ \frac{1}{s + R'} \int_{\tilde{\Omega}} \frac{\widetilde{\text{MDE}}(\mathbf{q})}{s + \mathbf{q}^2 D} d^3q \right\}(\tau). \quad (8.25)$$

The integration is again carried out over the whole space $\tilde{\Omega}$. We do not need to cut the integral (which stems from the term $\Theta(s)$ in Eq. 8.12) at the radius Λ because the integral has anyway almost no contribution for large $|\mathbf{q}|$ due to the very localized $\widetilde{\text{MDE}}(\mathbf{q})$. By making use of the convolution theorem for Laplace transformation

$$\mathcal{L}^{-1}\{\tilde{f}(s)\tilde{g}(s)\}(t) = \int_0^\tau f(t-t')g(t')dt' \quad (8.26)$$

and after carrying out the inverse Laplace transform in Eq. 8.25 we can rewrite $G'_{01}(\tau)$ as

$$G'_{01}(\tau) = \frac{\alpha\langle C \rangle}{(2\pi)^{3/2}} \int_0^\tau e^{-R'(\tau-t)} \int_{\tilde{\Omega}} \widetilde{\text{MDE}}(\mathbf{q}) \exp(-\mathbf{q}^2 Dt) d^3q dt. \quad (8.27)$$

By proceeding in a similar way for $G'_{10}(\tau)$ it is possible to show that

$$G'_{10}(\tau) \equiv G'_{01}(\tau). \quad (8.28)$$

Given our initial assumption, $R \ll D/\omega_{xy}^2$, the integral over $\tilde{\Omega}$ vanishes very fast with time, t , compared to the variation of $\exp(R't)$. Hence, we approximate

$$G'_{01}(\tau) \approx \frac{\alpha\langle C \rangle}{(2\pi)^{3/2}} e^{-R'\tau} \int_{\tilde{\Omega}} \widetilde{\text{MDE}}(\mathbf{q}) \int_0^\tau \exp(-\mathbf{q}^2 Dt) dt d^3q. \quad (8.29)$$

We will now estimate the maximum of $G'_{01}(\tau)$. By carrying out the integral over t in 8.29 we derive

$$G'_{01}(\tau) < \frac{\alpha\langle C \rangle}{(2\pi)^{3/2}} e^{-R'\tau} \int_{\tilde{\Omega}} \frac{\widetilde{\text{MDE}}(\mathbf{q})}{\mathbf{q}^2 D} d^3q. \quad (8.30)$$

Fourier transforming Eq. 8.3 yields

$$\begin{aligned} \widetilde{\text{MDE}}(\mathbf{q}) &= \frac{\pi\omega_{xy}^2}{h(1/h^2 + q_z^2)} \exp\left[-\frac{1}{8}\omega_{xy}^2(q_x^2 + q_y^2)\right] \\ &< \pi\omega_{xy}^2 h \exp\left[-\frac{1}{8}\omega_{xy}^2(q_x^2 + q_y^2)\right]. \end{aligned} \quad (8.31)$$

Inserting the right-hand side of this inequality into 8.29 and integrating yields

$$G'_{01}(\tau) < \alpha \langle C \rangle \pi^2 \frac{\omega_{xy} \hbar}{D} e^{-R'\tau}. \quad (8.32)$$

This upper limit can be compared with the term G'_{00} , which has the same temporal behavior. With Eq. 8.23 we get easily

$$G'_{01}(\tau) < \pi^2 R' \frac{\omega_{xy} \hbar}{D} G'_{00}(\tau). \quad (8.33)$$

In the present setup we have approximately $\tau_{xy} \equiv \omega_{xy}^2 / (4D) \approx \omega_{xy} \hbar / D$. Provided that our assumption holds, that is to say $R' \ll 1/\tau_{xy}$, we can neglect the cross-correlation term.

To calculate the last term, $G'_{11}(\tau)$, we insert $\delta\tilde{C}(\mathbf{q}, s)$ from Eq. 8.8 in Eq. 8.19. After some rewriting, using Eqs. 8.20 to 8.22 we get

$$G'_{11}(\tau) = \mathcal{L}^{-1} \left\{ \int_{\tilde{\Omega}} \frac{\widetilde{\text{MDE}}^2(\mathbf{q})}{s + \mathbf{q}^2 D} d^3q \right\}(\tau) - G''_{11}(\tau) \quad \text{with} \quad (8.34)$$

$$G''_{11}(\tau) = (2\pi)^{-3/2} \mathcal{L}^{-1} \left\{ \int_{\Omega'} \int_{\tilde{\Omega}} \widetilde{\text{MDE}}(\mathbf{q}) \widetilde{\text{MDE}}(\mathbf{r}') \frac{s}{s + \mathbf{q}^2 D} \langle \delta\tilde{n}(s) \delta C(\mathbf{r}', 0) \rangle d^3q d^3r' \right\}(\tau). \quad (8.35)$$

With the convolution theorem and Eq. 8.17 we derive

$$\begin{aligned} G''_{11}(\tau) &= (2\pi)^{-3/2} \int_0^\tau G'_{01}(\tau - t') \int_{\tilde{\Omega}} \widetilde{\text{MDE}}(\mathbf{q}) \mathcal{L}^{-1} \left\{ \frac{s}{s + \mathbf{q}^2 D} \right\}(t') d^3q dt'. \\ &= (2\pi)^{-3/2} \left[G'_{01}(\tau) - \int_0^\tau G'_{01}(\tau - t') \int_{\tilde{\Omega}} \widetilde{\text{MDE}}(\mathbf{q}) \exp(-\mathbf{q}^2 D t') d^3q dt' \right]. \end{aligned} \quad (8.36)$$

With the same arguments we used for estimating an upper bound for $G'_{01}(\tau)$ we can derive an upper bound for $G''_{11}(\tau)$. Using that $G'_{01}(\tau) \propto \exp(-R'\tau)$ changes slowly with time compared to the integral over $\tilde{\Omega}$ we can show that

$$\begin{aligned} G''_{11}(\tau) &= (2\pi)^{-3/2} G'_{01}(\tau) \int_{\tilde{\Omega}} \widetilde{\text{MDE}}(\mathbf{q}) \exp(-\mathbf{q}^2 D \tau) d^3q \\ &< G'_{01}(\tau). \end{aligned} \quad (8.37)$$

Hence, if $G'_{01}(\tau)$ is negligible, the same holds for $G''_{11}(\tau)$. Neglecting $G''_{11}(\tau)$ we get from Eq. 8.34

$$G'_{11}(\tau) = \int_{\tilde{\Omega}} \widetilde{\text{MDE}}^2(\mathbf{q}) \exp(-\mathbf{q}^2 D \tau) d^3q. \quad (8.38)$$

This can be easily integrated to give a function that is found to be proportional to the autocorrelation function in chapter 7, derived for free diffusion. Carrying out the integration yields

$$G'_{11}(\tau) = \left(1 + \frac{\omega^2 \tau}{\tau_z} \right)^{-1} \left[\left(1 - \frac{\tau}{2\tau_z} \right) w \left(i \sqrt{\frac{\tau}{4\tau_z}} \right) + \sqrt{\frac{\tau}{\pi\tau_z}} \right]. \quad (8.39)$$

So far we got analytical solutions for all terms that constitute $G(\tau)$. With Eq. 8.15 we get as the final result

$$\begin{aligned} G(\tau) &= 1 + \frac{\langle n \rangle (1 - \langle n \rangle)}{(N + \langle n \rangle)^2} e^{-R'\tau} \\ &+ \frac{\gamma N}{(N + \langle n \rangle)^2} \left(1 + \frac{\omega^2 \tau}{\tau_z} \right)^{-1} \left[\left(1 - \frac{\tau}{2\tau_z} \right) w \left(i \sqrt{\frac{\tau}{4\tau_z}} \right) + \frac{2}{\sqrt{\pi}} \sqrt{\frac{\tau}{\tau_z}} \right]. \end{aligned} \quad (8.40)$$

The form of the derived autocorrelation is fairly simple. Note however that N and $\langle n \rangle$ are not independent; both depend on the concentration $\langle C \rangle$. It is easy to see that this function reduces to the autocorrelation for free diffusion (Eq. 7.6) for $k_+ \rightarrow 0$.

In [96] Starr et al. showed that the very general $G(\tau)$ they derived for adsorption can be approximated by quite simple analytical expressions if the diffusion through the observation volume is fast compared to the reaction rate. In order to classify their approximations the authors introduced different rates, namely the *diffusion rate*, $R_d \equiv D/h^2$, the *reaction rate*, R , and the *transportation rate* $R_t \equiv D[C/(\beta C_o)]^2$. Here, C_o denotes the surface concentration of occupied binding sites. The parameter $\beta \equiv (S - C_o)/S$ is the fraction of unoccupied binding sites, where S is the total surface concentration of binding sites. For $\omega \rightarrow 0$ and if $R_r \ll R_t$ and in addition $R_r \ll R_d$, their result becomes similar to $G(\tau)$ given by Eq. 8.40. Differences exist in the weights assigned to the two terms $G'_{00}(\tau)$ and $G'_{11}(\tau)$ in Eq. 8.40 and in the decay rate of $G'_{00}(\tau)$, which is R in the cited case and R' in our case. Note, that R' becomes R in the limit $a \rightarrow \infty$ (but holding k_+ constant) or in other words if we drop the idea of a localized binding site.

So far, the influence of triplet kinetics on the autocorrelation function has been neglected. To take account of triplet kinetics we proceed similar as in chapter 4. We write the differential equations for combined intersystem crossing, diffusion and binding:

$$\frac{\partial}{\partial t} C_i(\mathbf{r}, t) = D \nabla^2 C_i(\mathbf{r}, t) - \delta(\mathbf{r}) \frac{d}{dt} n_i(t) + \sum_{j=0}^1 K_{ij} C_j(\mathbf{r}, t), \quad (8.41)$$

$$\frac{d}{dt} n_i(t) = k_+[1 - n(t)]C_i(0, t) - k_-n_i(t) + \sum_{j=0}^1 K_{ij} n_j(\mathbf{r}, t). \quad (8.42)$$

The subscripts take values 0 and 1 for the dark state and the bright state, respectively. Here and below we refer to the model described in chapter 4. The K_{ij} are given by Eq. 4.25. We introduce the concentration correlations

$$\phi_{ij}^{CC}(\mathbf{r}, \mathbf{r}', t) = \langle \delta C_i(\mathbf{r}, t) \delta C_j(\mathbf{r}', 0) \rangle, \quad (8.43)$$

$$\phi_{ij}^{nn}(\mathbf{r}, \mathbf{r}', t) = \delta(\mathbf{r}) \delta(\mathbf{r}') \langle \delta n_i(t) \delta n_j(0) \rangle, \quad (8.44)$$

$$\phi_{ij}^{Cn}(\mathbf{r}, \mathbf{r}', t) = \delta(\mathbf{r}') \langle \delta C_i(\mathbf{r}, t) \delta n_j(0) \rangle, \quad (8.45)$$

$$\phi_{ij}^{nC}(\mathbf{r}, \mathbf{r}', t) = \delta(\mathbf{r}) \langle \delta n_i(t) \delta C_j(\mathbf{r}', 0) \rangle. \quad (8.46)$$

By making use of the equilibrium conditions that is to say $k_+(1 - \langle n \rangle) \langle C_i \rangle = k_- \langle n_i \rangle$ and $\sum_{j=0}^1 K_{ij} \langle n_j \rangle = \sum_{j=0}^1 K_{ij} \langle C_j \rangle = 0$ and after linearizing we get

$$\frac{\partial}{\partial t} \phi_{ij}^{CC}(\mathbf{r}, \mathbf{r}', t) = D \nabla^2 \phi_{ij}^{CC}(\mathbf{r}, \mathbf{r}', t) - \frac{d}{dt} \phi_{ij}^{nC}(\mathbf{r}, \mathbf{r}', t) + \sum_{k=0}^1 K_{ik} \phi_{kj}^{CC}(\mathbf{r}, \mathbf{r}', t), \quad (8.47)$$

$$\frac{\partial}{\partial t} \phi_{ij}^{nn}(\mathbf{r}, \mathbf{r}', t) = -R \phi_{ij}^{nn}(\mathbf{r}, \mathbf{r}', t) - k_+(1 - \langle n \rangle) \phi_{ij}^{Cn}(\mathbf{r}, \mathbf{r}', t) + \sum_{k=0}^1 K_{ik} \phi_{kj}^{nn}(\mathbf{r}, \mathbf{r}', t), \quad (8.48)$$

$$\frac{\partial}{\partial t} \phi_{ij}^{Cn}(\mathbf{r}, \mathbf{r}', t) = D \nabla^2 \phi_{ij}^{Cn}(\mathbf{r}, \mathbf{r}', t) - \frac{d}{dt} \phi_{ij}^{nn}(\mathbf{r}, \mathbf{r}', t) + \sum_{k=0}^1 K_{ik} \phi_{kj}^{Cn}(\mathbf{r}, \mathbf{r}', t), \quad (8.49)$$

$$\frac{\partial}{\partial t} \phi_{ij}^{nC}(\mathbf{r}, \mathbf{r}', t) = -R \phi_{ij}^{nC}(\mathbf{r}, \mathbf{r}', t) - k_+(1 - \langle n \rangle) \phi_{ij}^{CC}(\mathbf{r}, \mathbf{r}', t) + \sum_{k=0}^1 K_{ik} \phi_{kj}^{nC}(\mathbf{r}, \mathbf{r}', t). \quad (8.50)$$

The initial conditions are

$$\phi_{ij}^{CC}(\mathbf{r}, \mathbf{r}', 0) = \delta_{ij} \langle C_j \rangle \delta(\mathbf{r} - \mathbf{r}'), \quad (8.51)$$

$$\phi_{ij}^{nn}(\mathbf{r}, \mathbf{r}', 0) = \delta_{ij} \delta(\mathbf{r}) \delta(\mathbf{r}') \langle n_j \rangle (1 - \langle n_j \rangle), \quad (8.52)$$

$$\phi_{ij}^{Cn}(\mathbf{r}, \mathbf{r}', 0) = \phi_{ij}^{nC}(\mathbf{r}, \mathbf{r}', 0) = 0. \quad (8.53)$$

We make the ansatz $\phi_{ij}^{\xi\zeta}(\mathbf{r}, \mathbf{r}', t) = g_{ij}(t) \phi^{\xi\zeta}(\mathbf{r}, \mathbf{r}', t)$ with $\xi, \zeta \in \{C, n\}$. The functions $g_{ij}(t)$ are given in chapter 4 and the $\phi^{\xi\zeta}(\mathbf{r}, \mathbf{r}', t)$ are the solutions for the case where no intersystem crossing is present. That is to say, $K_{ij} = 0$ and all molecules are in the bright state. It is easy to verify that this ansatz satisfies the above equations. We derive again $G_t(\tau) = 1 + g_{11}(\tau) [G(\tau) - 1]$. With Eqs. 4.31 and 8.40 we get as the final result

$$\begin{aligned} G_T(\tau) = 1 + & \left[1 + \frac{p}{1-p} \exp\left(-\frac{\tau}{\tau_t}\right) \right] \left\{ \frac{\langle n \rangle (1 - \langle n \rangle)}{(N + \langle n \rangle)^2} e^{-R'\tau} \right. \\ & \left. + \frac{\gamma N}{(N + \langle n \rangle)^2} \left(1 + \frac{\omega^2 \tau}{\tau_z} \right)^{-1} \left[\left(1 - \frac{\tau}{2\tau_z} \right) w\left(i\sqrt{\frac{\tau}{4\tau_z}}\right) + \frac{2}{\sqrt{\pi}} \sqrt{\frac{\tau}{\tau_z}} \right] \right\}. \end{aligned} \quad (8.54)$$

The way how $G(\tau)$ depends on its different parameters suggests that it should in principle be possible to obtain estimates for all of them by fitting one data set, provided that γ and $\Sigma(0)$ are known. Practically, apart from the difficulty to know $\Sigma(0)$ a priori, it is almost impossible to exactly situate the binding site at the center of the observation volume. It is easy to see that the position of the receptor will change the magnitudes of the summands in 8.40. Therefore, if the exact position of the receptor is not known, no information about $\langle n \rangle$ and $\langle N \rangle$ can be deduced from $G(\tau)$. A workaround would be to do a global fit on measurement sets for different ligand concentrations.

8.2 Measurements and data analysis

Several measurements for combined diffusion and binding were performed by means of objective-type TIR-FCS. The intention of these measurements was twofold. Firstly, we aimed to demonstrate the applicability of the present method to single molecule binding kinetics. Secondly, we purposed to get a direct measure of the obtainable count rate per molecule and the signal to background ratio by investigating high resolution time traces for single adsorbing fluorophores.

8.2.1 Adsorption and desorption

Free rhodamine 6G (Rh6G) molecules in aqueous solution are prone to undergo adsorption on glass surfaces. Adsorption of the dye to the microscope cover slide in our TIR-FCS setup becomes apparent as an increase of the correlation time when compared to pure diffusion. Furthermore, photon bursts become visible in the intensity time trace in the case that the concentration is low enough. A typical time trace obtained for a 1 nM solution of Rh6G in buffer at a laser power of about 20 to 22 mW is shown in Fig. 8.2 (data recorded by means of a TCSPC card). Similar data as well as the experimental conditions for this study are discussed in detail in paper III. We will though present a summary of the results below.

The observed bursts have different heights, depending on the position inside the observation volume where the fluorophore binds to the surface. Several bursts which may be due to binding as well as single molecules diffusing through the observation volume last shorter than the binning time. In this case the burst height depends not only on the fluorophores position but also on its length of stay inside the observation volume. The burst width is a random variable with

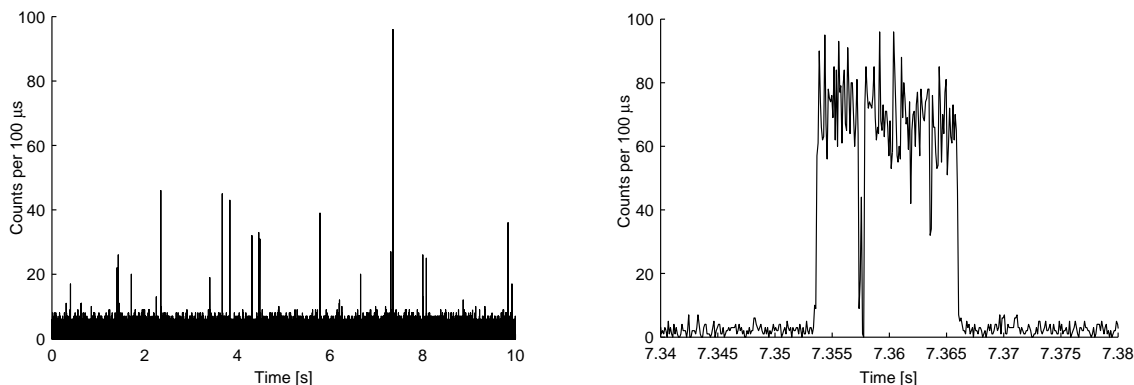


Figure 8.2: Left: high resolution time trace for Rh6G molecules subject to adsorption and desorption on a microscope cover slide. Right: a detail of the time trace shown left.

a mean value depending on the dissociation rates. Since the excitation intensity applied in this experiment was very high the width is further influenced by photobleaching. The burst statistics and the on/off character of several very wide and large bursts as e.g. shown in Fig. 8.2 leads us to interpret them as single molecule events. The arguments are discussed in detail in paper III. Single molecule events with count rates per molecule as high as 700 kHz and a signal to background ratio of 35 could be observed in different time traces. This should be regarded as a lower bound for the maximal obtainable count rate under the present conditions. The maximum would be obtained for a fluorophore binding exactly in the center of the observation volume.

As described in chapter 7 and in paper III a count rate per molecule of ~ 1.8 MHz could be inferred from measurements on diffusing Rh6G molecules. This discrepancy with respect to the result discussed above could not be completely explained. However, several reasons can be imagined that lead to a smaller estimate in the present case: The intensity on the surface of the cover slide depends critically on the alignment of the optical excitation path. In particular, a change in the incidence angle leads to a different intensity on the glass surface, which influences the count rate per molecule. The position of the pinhole in the image plane determines further what excitation intensity is actually seen. The measurements were not performed at the same day and at least the angle and the pinhole position were readjusted before each measurement series. Therefore, a difference in the excitation intensity can be expected. This explanation is further supported by the fact that the background for the diffusion measurement was higher, too, such that the measured signal-to-background ratio was 39, which is close to the value inferred from the measurements discussed above. Furthermore, the count rate per molecule depends critically on the objective's focus position relative to the glass surface. The optimal position was in general found by changing the axial position of the objective until the amplitude of the correlation curve was maximal. This is easily done for high fluorophore concentrations but difficult when the concentration is low and the fluorophores are reversibly adsorbing to the surface. In this case, the amplitude of the correlation curve fluctuates strongly during the first seconds of data acquisition, allowing only for an approximate alignment. At last, the count rate inferred from the experiments on binding molecules are lower bounds as explained above.

As a matter of fact, the signal strength and the signal to background-ratio for adsorbing Rh6G in the objective-type setup is high enough to conveniently observe single molecules by the eye through the microscopes ocular. We observed single molecules appearing in the field of few and sticking to the surface for several seconds before disappearing again, presumably because of photo-bleaching. Others appeared as short-lived flashes when they diffused through

the evanescent field or adsorbed to the surface before they desorbed again after a very short time. Even rare events of molecules 'rolling' over the surface could be observed that way.

8.2.2 Binding to a single binding site

We had no biological receptor ligand system at our disposition. As an alternative we observed binding of dye molecules to single binding sites on specially prepared microscope cover slides. The experimental conditions were as follows: The glass slides (thickness $150\ \mu\text{m}$) were carefully rinsed using double-distilled water. Afterwards, they were cleaned in a solution of 2% Helmanex for 15 min in an ultrasonic bath at room temperature. After rinsing with double-distilled water, they were dried under nitrogen. Finally they were treated with oxygen plasma for 10 min and stored in double-distilled water until use.

The sample consisted of 10 nM Rh6G in potassium phosphate buffer (pH 7). This solution was applied to the cleaned microscope cover slide. Fluorescence excitation was realized with the green line of the argon-ion laser, at an output power of 22 mW, which implies an intensity at the surface of about $180\ \mu\text{W}\ \mu\text{m}^{-1}$.

When the glass slides are prepared according to the protocol described above, adsorption is efficiently reduced. For Rh6G applied in solution on the glass-slide, the measured correlation time was reduced and the autocorrelation data could be fitted by a single-component diffusion model in a satisfactory manner. However, by laterally scanning the pinhole through the image plane, individual locations were found where the correlation time was orders of magnitude larger. At such particular positions, the intensity time traces showed sequences of photon bursts as observed for adsorption on a cover slide not specially prepared. Few spots that were continuously blinking at 'very high' frequencies could be observed through the microscope's ocular. The effect was interpreted as being due to single molecules binding and releasing from a single binding site.

As a matter of fact, in this kind of experiment we do not have a real control over the nature of the investigated binding sites. It should be understood as a hypothesis that we deal with molecular binding sites, which bind only one molecule at a time. From TIRF pictures obtained with a CCD camera we can at least infer that the binding sites are not bigger than the observation volume. Fluorophores binding locally give rise to bright spots with a FWHM that equals approximately the theoretical diffraction limit times the magnification of the optical system (see Fig. 8.3).

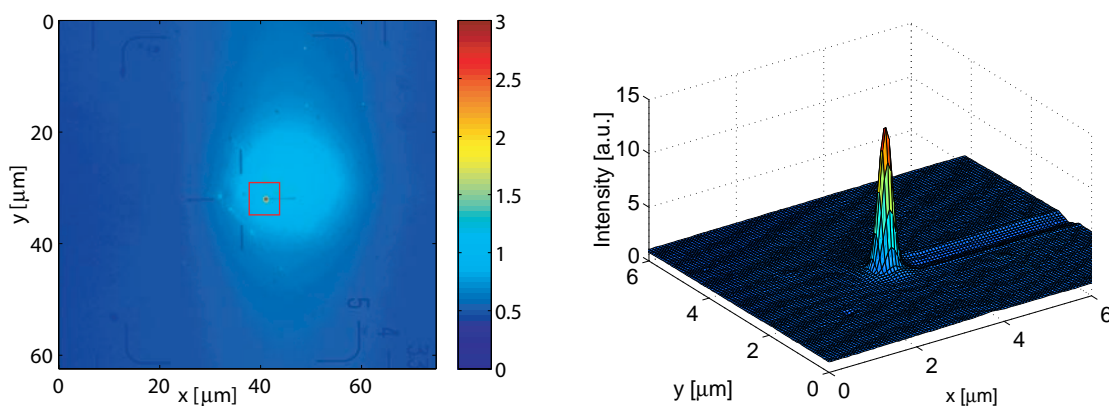


Figure 8.3: The left picture shows the cover slide surface in contact with a 10 nM Rh6G solution imaged with a CCD camera. The pixel size corresponds to $61\ \text{nm} \times 72\ \text{nm}$ in the sample space. The red rectangle indicates the borders of the detail shown in the right picture. Integration time was 10 s for an applied laser power of 10 – 15 mW.

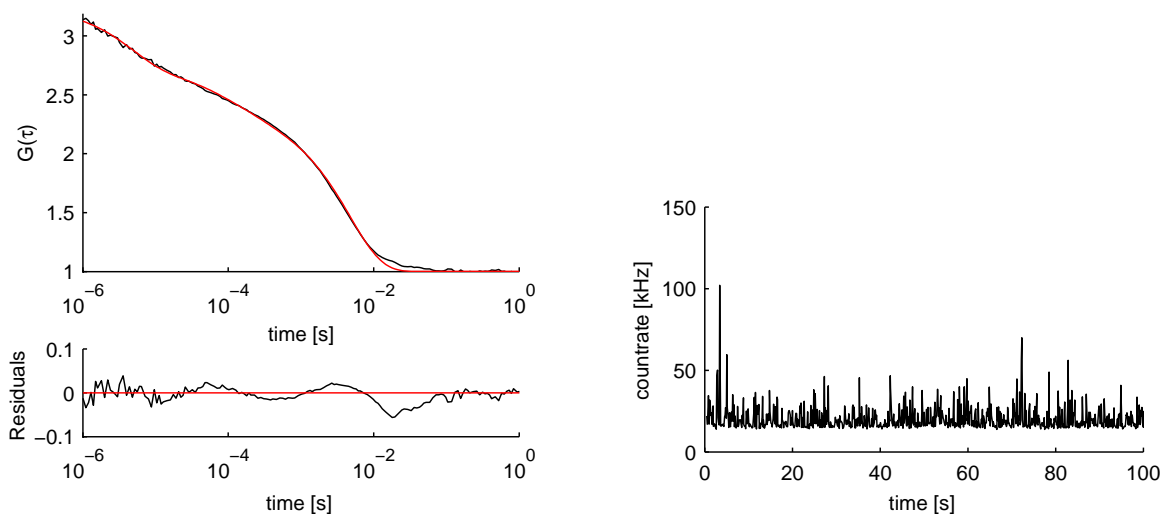


Figure 8.4: An autocorrelation curve for Rh6G reversibly binding to a single binding site (left) and the corresponding time trace (right) is shown. Fitting $G(\tau)$ from Eq. 8.54 to the data yielded the following parameter estimates: $R' = 206.2 \text{ s}^{-1}$; $\tau_z = 12.8 \text{ } \mu\text{s}$; $p = 20.7\%$; $\tau_T = 4.5 \text{ } \mu\text{s}$; $\omega = 0.18$ (fixed parameter).

Figure 8.4 shows a typical autocorrelation curve and the corresponding time-trace for Rh6G binding to such a localized site. The data was obtained in the following way: The CCD camera was used to position the cover slide with respect to the illuminated region in such a way that only one bright spot was visible in the field of view. (Figure 8.3 shows the corresponding camera image). After positioning the cover slide, the fiber-end was moved to the conjugated position of the binding site. To accurately superimpose the image of the spot and the fiber-end, the image plane was scanned in $50 \text{ } \mu\text{m}$ steps. The step motors were commanded by a Lab-View program and the output signal of the SPAD was acquired by the TCSPC card. The automatized scanning stopped when the photon count rate exceeded a certain threshold. In the given example this happened only at one position, which constitutes an indirect proof that this position was really conjugate to the bright spot observed in Fig. 8.3.

The detected signal was hardware correlated and the model given by Eq. 8.54 was used to fit the data by means of a global search routine. Parameter estimates are given in the figure caption. The estimates are reasonable, especially the diffusion time corresponds to values obtained from other measurements.

The obtained experimental results lead to the conclusion that it is in principal possible to measure binding rates of receptor-ligand systems on a single molecule basis by means of objective-type TIR-FCS. The investigation of intensity time traces for single molecules undergoing adsorption and desorption on a glass slide showed that objective-type TIR-FCS features a signal to background ratio high enough to allow for single molecule measurements. The last measurements showed that measuring the parameter R' is possible for a system that shares several characteristics with a biomolecular receptor, namely reversible binding and (at least a certain degree) of localization.

Chapter 9

Studying the enzymatic activity of horseradish peroxidase

Within the context of this doctoral thesis we performed preliminary investigations of enzymatic reactions on a single molecule level by means of objective-type TIR-FCS. Results obtained in the course of experiments described hereafter were in accordance with previously published results [32]. In the following chapter preliminary results are presented and experimental difficulties are discussed.

9.1 Motivation

It seems that Aristotle's famous statement: "The whole is more than the sum of its parts" holds even on the molecular level. In particular proteins are not only a set or sequence of amino-acids but their function depends on their molecular structure in a sensitive manner. After translation and before a protein becomes functional it folds into a particular structure or conformation. As was shown by theory, simulations and experiments, this process is rather complex and involves many intermediate steps, which leads to many slightly different conformations [98, 32]. Static structures of proteins and in particular enzymes are nowadays routinely determined by X-ray diffraction on crystallized proteins and nuclear magnetic resonance (NMR) measurements. Conformational changes in already folded proteins are less investigated although theory, simulations and several experiments indicate that thermodynamical fluctuations leading to conformational changes play an important role in protein function [30, 31]. Dynamic structural changes at equilibrium can be directly monitored by single molecule techniques but are not visible in ensemble measurements. Another question that can not be answered by ensemble averaged measurements is about homogeneity or heterogeneity in enzyme populations. If measurement on an ensemble shows that a particular characteristic of an enzyme has a certain distribution it is a priori not clear if all enzymes are equal in average and the distribution is due to the change within time of individual molecules (the homogeneous case) or if the species are different (the heterogeneous case). Single molecule techniques offer the possibility to address this question.

The first successful detection of a single molecule under biologically relevant conditions was reported in the 70s by T. Hirschfeld. He showed the detection of a single antibody labeled with 80 to 100 fluorophores. In 1990, E.B. Shera et al. [10] reported the detection of a single fluorophore under physiological conditions. Few years later, single immobilized fluorophores could be observed using a CCD camera in a wide-field TIRFM and epi-illumination configuration. By this technique, the group of T. Yanagida could observe single enzymatic turnovers of ATP molecules by myosin (T. Funatsu et al. [40]). In the late 1990s several studies have been

carried out in the group of R. Rigler to address the question of heterogeneity in a population of DNA molecules (with equal sequence). In these experiments the dye tetramethylrhodamine was attached through a 6-carbon-atom linker to the DNA molecule. Two states were observed, one where the dye was close to a guanine molecule and one where it was far. The two states can be distinguished because guanine efficiently quenches the fluorescence of tetramethylrhodamine. FCS measurements on diffusing DNA strands were successfully fitted by a stretched exponential function $\sim \exp[-(kt)^\beta]$, which indicates that the transition was not governed by one reaction rate but by a distribution of rates. Further measurements on immobilized, single DNA strands indicated the existence of subpopulations that undergo conformational transitions according to a single exponential law ($\beta = 1$), each with a different reaction rate. After Funatsu et al., several groups were successful in monitoring enzyme catalysis on a single molecule level [104, 105, 32, 106, 107].

Our motivation to perform FCS measurements on single immobilized horseradish peroxidase molecules stems from experiments performed by L. Edman et al. [32]. Horseradish peroxidase in the presence of hydrogen peroxide (H_2O_2) catalyzes the oxidation of the non-fluorescent substrate dihydrorhodamine 6G to the highly fluorescent dye rhodamine 6G. After termination of the catalytic step the complex enzyme - rhodamine 6G persists for a moment and can be observed by means of fluorescence spectroscopy. In the reported experiments, horseradish peroxidase molecules were immobilized on a microscope cover slide and confocal FCS was performed on single enzymes in the presence of the substrate and H_2O_2 . The recorded single molecule intensity time traces showed photon bursts of varying width, which are attributed to the enzyme-product complex and dark periods. Because the rhodamine dye is released quickly after product formation and continually replaced, the measurement time is not limited by photobleaching but only by the lifetime of the enzyme. The measurement time was virtually unlimited and although the signal-to-background ratio was very low ($\text{SBR} \approx 1$) valuable FCS data could be obtained by these measurements. The FCS data showed a stretched exponential behavior, which was attributed to a distribution of reaction rates. According to the authors, the enzyme undergoes conformational changes while it catalyzes the oxidation of dihydrorhodamine 6G. The distribution of rates arises if one assumes that the rate constants for substrate binding, product formation and reduction of hydrogen peroxide differ from one conformational state to the other.

From measurements on diffusing and binding dyes in our lab, we expected a signal-to-background ratio that should be about a factor 35 higher when using objective-type TIR-FCS to study the described molecular system. The questions we asked ourselves in this context were, firstly, if we would observe the same autocorrelation functions and, secondly, if we would be able to resolve individual conformations by reducing the integration time for recording an autocorrelation function.

9.2 Horseradish peroxidase

Peroxidases are heme¹ proteins that catalyze a large variety of different substrates by reduction of H_2O_2 . Models for the catalytic reaction cycle of horseradish peroxidase are shown in Fig. 9.1. The enzyme in its pentavalent state (of the heme group) turns over a substrate molecule into a product and is reduced to the tetravalent state. After a second turnover, where the enzyme is reduced to the trivalent state it is oxidized by H_2O_2 and returns to the pentavalent state, ready to start a new cycle.

¹A *heme* is an iron-containing cofactor made up of a large organic ring, the porphyrin and an iron atom in its center. The heme is a constituent of e.g. hemoglobin or myoglobin where it is responsible for the retention of O_2 . In general, the main role of the heme is to catalyze the oxidation of a substrate by changing its own oxidation state.

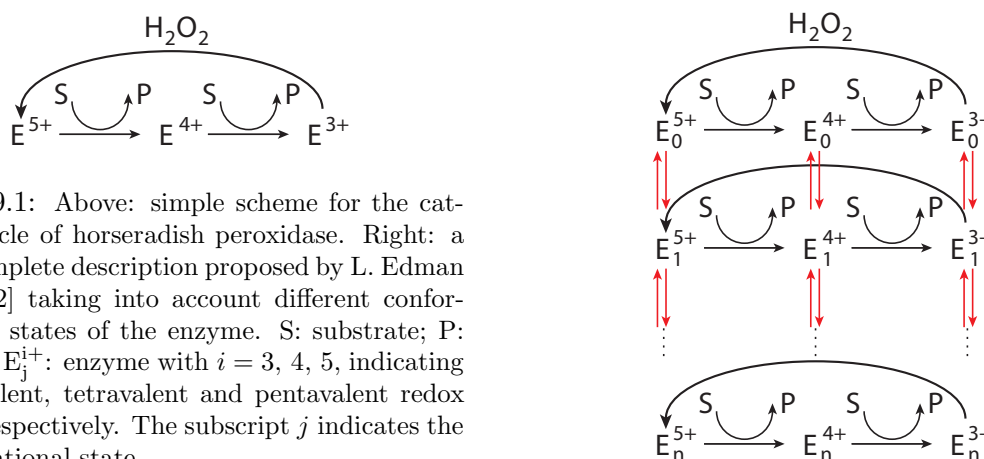


Figure 9.1: Above: simple scheme for the catalytic cycle of horseradish peroxidase. Right: a more complete description proposed by L. Edman et al. [32] taking into account different conformational states of the enzyme. S: substrate; P: product; E_j^{i+} : enzyme with $i = 3, 4, 5$, indicating the trivalent, tetravalent and pentavalent redox states, respectively. The subscript j indicates the conformational state.

In the case of horseradish peroxidase catalyzing the oxidation of dihydrorhodamine 6G, we are able to directly observe two states by means of fluorescence measurements: a bright state, or the enzyme-product complex and a dark state. The for FCS measurements relevant kinetic model is therefore simply



which describes the transition between the dark state or all states where no product is bound (E) and the bright state or the enzyme-product complex (EP).

We adapt the model proposed by L. Edman et al., which states that many different pathways with different associated rate constants, k_j with $j = 2, 3, 4 \dots$, lead to the formation of the enzyme-product complex. In other words, product formation is a process with a whole distribution of rates $\{k_j\}$. According to [32] there is only one rate constant for dissociation, k_{-1} , in contrast to product formation. From this model, the authors derived the following autocorrelation function

$$G(\tau) = 1 + A_1 \exp(-k_{-1}\tau) + A_2 \exp[-(k_1\tau)^\beta] + A_3 G_D(\tau), \quad (9.2)$$

where A_1 to A_3 are constants, $G_D(\tau)$ is the autocorrelation function for diffusion (without triplet-kinetics), k_1 is a mean product formation rate and β is the stretched parameter. The stretched parameter is a measure for the width of the distribution of $\{k_j\}$. The smaller β , (with $0 \leq \beta \leq 1$) the wider is the distribution of the rates.

9.3 Materials and Methods

9.3.1 Optical setup

All the objective-type TIR-FCS measurements were carried out with the setup explained in chapter 6 using the 515 nm line of the argon-ion laser and adequate interference filters. The applied laser power was typically ~ 3 mW in order to minimize the probability of photobleaching of the enzyme-bound product.

Several control measurements were performed on a commercial confocal FCS setups (ConfoCor 1, Carl Zeiss GmbH, Jena, Germany), using the 515 nm line of an argon-ion laser.

9.3.2 Chemicals

Biotinylated horseradish peroxidase was dissolved in phosphate buffered saline (PBS) buffer (10 mM phosphate, 100 mM NaCl, pH 7.4) before incubation. Dihydrorhodamine 6G and hydrogen peroxide were dissolved in di-potassium hydrogen phosphate buffer (100 mM K_2HPO_4 , pH 7.0). Samples used for measurements with immobilized enzymes were kept on ice before application.

9.3.3 Surface preparation

Biotinylated horseradish peroxidase was immobilized on microscope cover slides (typically 150 μm thick, 22 mm in diameter) using the following protocol: Coverslips were rinsed 10 times under double distilled water, before and after washing them in an ultrasonic bath. Washing in the ultrasonic bath was carried out at room-temperature, for 15 minutes in a solution of 2% Helmanex in double distilled water. After drying with nitrogen, the slides were treated for 10 min with oxygen plasma and stored in PBS buffer. These steps were all carried out in a 250 ml teflon vessel, carrying about 30 slides.

In first experiments we used slides incubated with a solution of biotinylated bovine-serum-albumin (BSA) in order to immobilize the enzyme. FCS measurements with rhodamine 6G dye on the BSA coated slides showed a considerable increase of the correlation time, which indicated an increase in surface binding of the dye. In order to get rid of as far as possible all kinetic processes contributing to the autocorrelation other than the enzyme kinetic we changed the protocol and used biotinylated polylysine-polyethylenglycol linker (PLL-g-PEGbiotin). Coverslips were coated with PLL-g-PEGbiotin and incubated with streptavidin. After removing excess streptavidin, 150 μl of 5 nM or 10 nM horseradish peroxidase was applied on each slide and incubated for 1 h at 4°C.

After incubation, the slides were rinsed with buffer and mounted on a slide holder. A teflon ring, pressed from above onto the prepared cover slide defined a recipient for the sample and prevented it from spreading over the hydrophilic surface. During all steps, much care was taken to prevent the surface with the immobilized enzyme from drying up.

9.3.4 Data acquisition and analysis

Autocorrelation data acquired by means of the objective-type setup was analyzed using the model represented in Eq. 9.2. For fitting of the data we fixed the structure parameter, $\omega = 0.17$.

Measurements obtained with the Confocor 1 were analyzed by means of the in-build data analysis software.

9.4 Results

9.4.1 Activity of horseradish peroxidase in solution

In order to check that the biotinylated enzyme is active, we monitored the fluorescence emission of solutions containing 50 nM substrate, 5 nM enzyme and 1 mM cosubstrate as a function of time. Far from the interface, during a measurement time of 5 min an increase of fluorescence intensity from typically 300 kHz to 1 MHz was observed. The sample was measured immediately after preparation. For comparison, for a solution of 50 nM dihydrorhodamine 6G in buffer a count rate of ~ 20 kHz was typically observed.

9.4.2 Measurements on the substrate in the absence of the enzyme

Neither the enzyme without H_2O_2 nor the cosubstrate without the enzyme could cause an oxidation of dihydrorhodamine 6G. FCS measurements using the Confocor 1 were performed for solutions of 50 nM substrate, and 5 nM enzyme or 1 mM cosubstrate. No visible rise of the intensity during measurement times of typically 30 s could be observed. From FCS measurements on Rh6G and dihydrorhodamine 6G solutions of equal concentrations we could infer that the relative portion of oxidized dye in our samples was always less than 5%. These measurements were performed far from the interface.

9.4.3 Measurements on the immobilized enzyme

For the measurements described hereafter, we incubated the slides with 10 nM enzymes in solution. We applied samples containing different concentrations of H_2O_2 and substrate in buffer. To find single, immobilized enzymes we scanned the fiber-end through the image plane of the microscope. The scanning was performed semi-automatically. That is to say the fiber-end moved in $50 \mu\text{m}$ steps, over the image of the illuminated area, the time-trace was continually monitored and the scanning interrupted or the pinhole position stored if the time-trace showed a sequence of intensity bursts. The position of the pinhole was fine-adjusted to maximize burst heights and the amplitude of the autocorrelation curve before performing measurements at the particular spot. Control measurement were taken at distances $\geq 100 \mu\text{m}$ of the fiber-end beside the image of the presumable enzyme.

Figure 9.2 shows an example for a measurement for a substrate concentration of $\sim 100 \mu\text{M}$. Fitting the data with the model given by Eq. 9.2 yielded satisfactory results, which are similar to values obtained in [32] with exception of k_1 (about a factor of ten smaller in the present case). The stretched parameter was in all measurements < 0.5 , which indicates a widespread distribution of rate constants.

Figure 9.3 shows a autocorrelation curve and time-trace recorded at a fiber-end position $100 \mu\text{m}$ below the previous position. A similar short correlation time and small count rates were observed everywhere while scanning to find spots with characteristic long correlation times and time-traces that should indicate the presence of an active enzyme. Sites with characteristic time-traces and correlation curves were rare and their surface concentration did not exceed $1/5 \mu\text{m}^{-2}$. The observed correlation time is longer as should be observed for pure diffusion of Rh6G, which was explained by an interaction of the fluorophore with the surface. For comparison, the data was fitted with the model for enzyme kinetics. The rate constant k_1 for the data in 9.3 is substantially increased and the amplitude A_1 is almost zero, indicating the absence of slow kinetic processes.

A widespread distribution of rates is also obvious from high resolution time-traces recorded at the same pinhole position as for the measurement on the presumable enzyme. A typical time-trace and a detailed view are shown in Fig. 9.4. We observe the existence of periods with very few 'activity' (low average count rate and short bursts) and with high 'activity' (high average count rate) as for instance interval [29 s, 31 s] and [31 s, 31.5 s], respectively. In periods like in interval [31 s, 31.5 s] fluctuations are too high to be simply explained by shot noise. Furthermore, the calculation of the correlation curves for such intervals showed that the fluctuations are correlated. Thus, kinetics on at least two different time-scales can be observed. One, that results in an alternation of 'active' and less 'active' states and another that results in fast fluctuations that are manifest during 'active' states as e.g. in interval [31 s, 31.5 s]. Starting from the assumption that the observed fluctuations are the manifestation of the catalytic process of a single horseradish peroxidase molecule, it seems if the enzyme would change the intensity of its catalytic activity in a periodic manner. This supports the hypothesis stated in [32] that

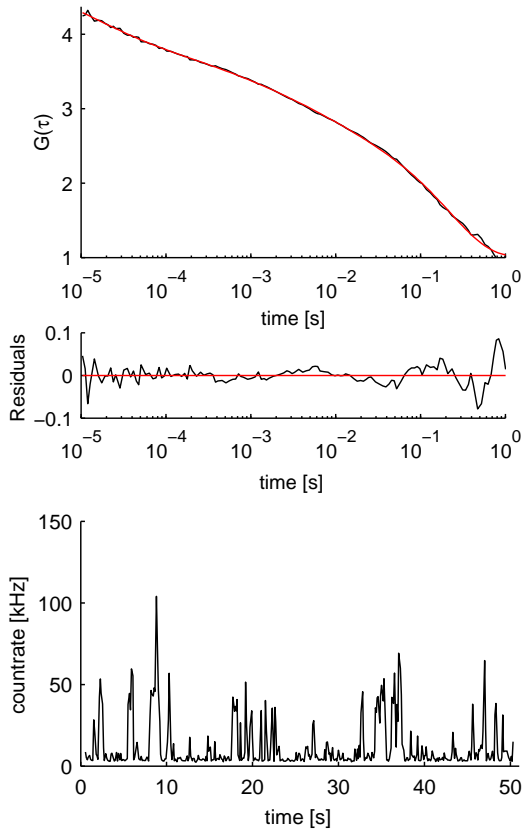


Figure 9.2: Autocorrelation curve and time-trace. Parameter estimates: $A_1 = 1.27$; $A_2 = 1.85$; $k_{-1} = 3.9 \text{ s}^{-1}$; $k_1 = 144 \text{ s}^{-1}$; $\beta = 0.34$; $A_3 = 0.75$; $\tau_z = 1.3 \mu\text{s}$. The structure parameter was fixed to $\omega = 0.17$.

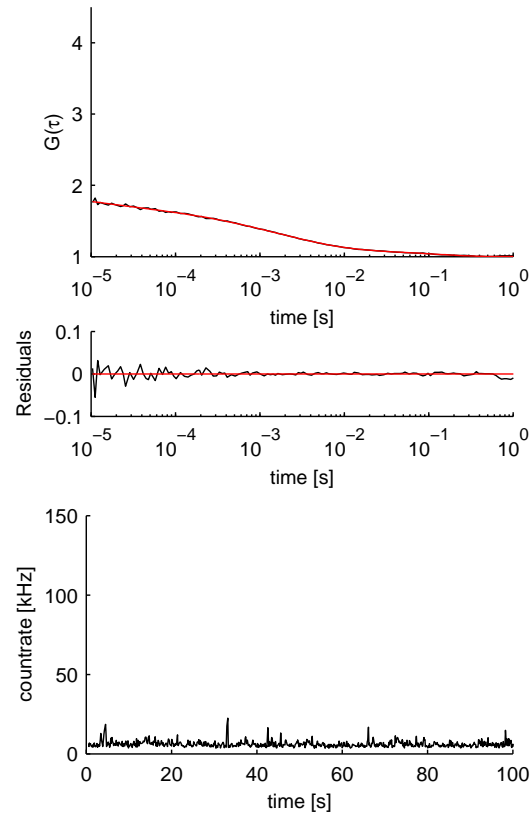


Figure 9.3: Autocorrelation curve and time-trace after moving the fiber-end $100 \mu\text{m}$ with respect to the measurement position in Fig. 9.2. Parameter estimates: $A_1 = 0.08$; $A_2 = 0.63$; $k_{-1} = 7.4 \text{ s}^{-1}$; $k_1 = 547 \text{ s}^{-1}$; $\beta = 0.55$; $A_3 = 0.16$; $\tau_z = 1.9 \mu\text{s}$; $\omega = 0.17$ (fixed)

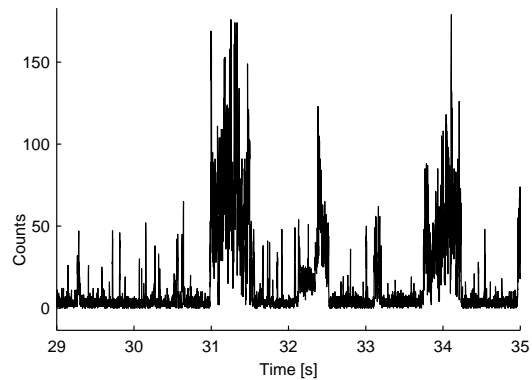
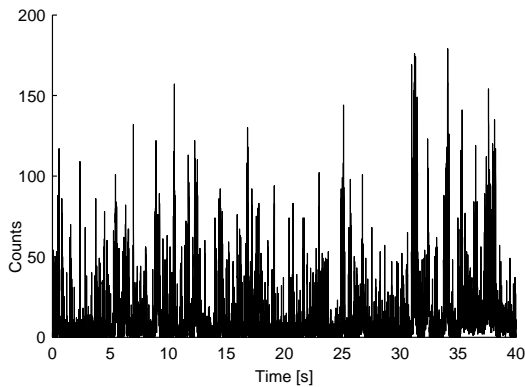


Figure 9.4: Time-trace for a measurement time of 40 s with 1 ms binning time (left). A detail of this time-trace is shown on the right.

horseradish peroxidase changes its conformation leading to a fluctuation in the enzymes activity. However, we were not able to rule out the possibility that the observed intensity fluctuations were due to binding of Rh6G, that inevitably contaminates the sample. The question of the presence of artifacts will be discussed in the following section.

9.4.4 Control Measurements

Negative control measurements were realized on cover slides prepared as explained in section 9.3 but without performing the last step, the incubation with biotinylated enzyme. Sample solutions of dihydrorhodamine 6G and H_2O_2 in buffer were applied to the prepared cover slides. The fiber-end was then scanned in the microscopes image-plane as was done in the presence of enzyme. These measurements were performed on different slides for different substrate and cosubstrate concentrations. As for the measurements described above, on several discrete spots sequences of bursts could be observed in the intensity time-traces. On these spots autocorrelations and high-resolution time-traces were recorded.

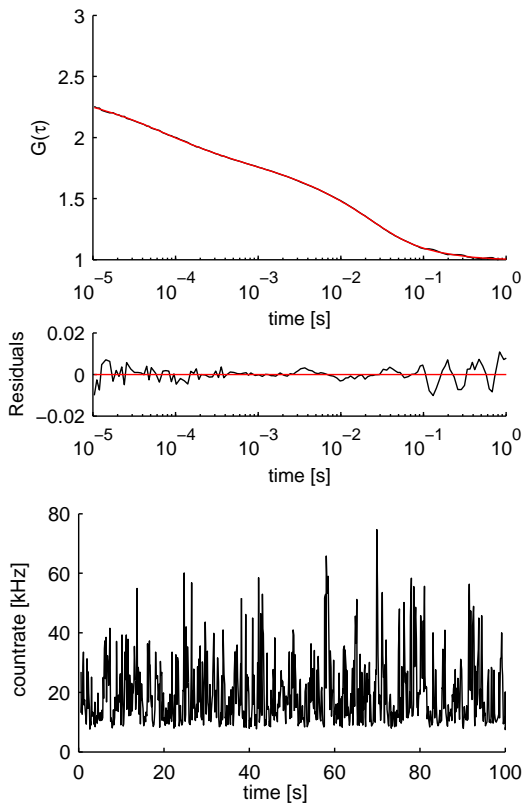


Figure 9.5: Autocorrelation curve and detail of a time-trace for a control measurement. Parameter estimates: $A_1 = 0.20$; $A_2 = 0.68$; $k_{-1} = 39.3 \text{ s}^{-1}$; $k_1 = 60.0 \text{ s}^{-1}$; $\beta = 0.40$; $A_3 = 0.43$; $\tau_z = 6.2 \mu\text{s}$. The structure parameter was fixed to $\omega = 0.17$.

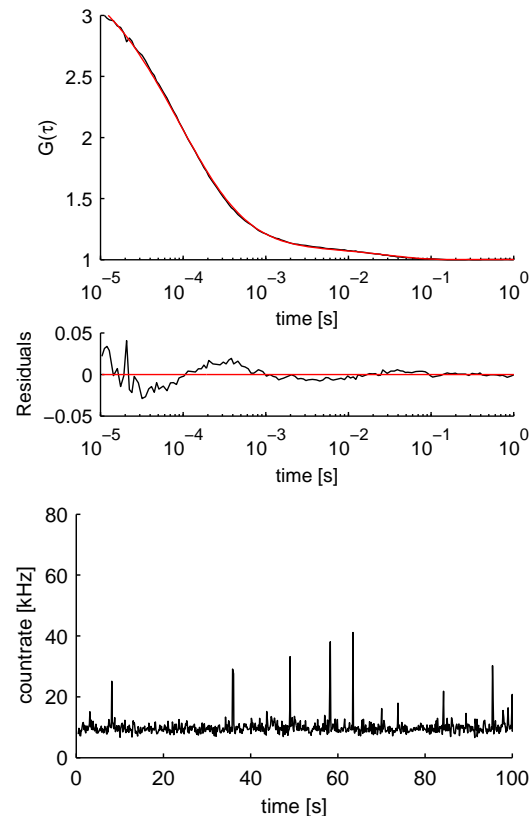


Figure 9.6: Autocorrelation curve and detail of a time-trace obtained for a different fiber-end position. Other parameters as for the measurement represented in Fig. 9.5 Parameter estimates: $A_1 = 0.09$; $A_2 = 0.00$; $k_{-1} = 29.83 \text{ s}^{-1}$; $\beta = 0.001$; $A_3 = 2.3$; $\tau_z = 9.7 \mu\text{s}$.

Figures 9.5 and 9.6 show examples for autocorrelation functions obtained for a substrate concentration of 50 nM and a cosubstrate concentration of 1 mM. The measurement time was 180s in both cases. Although a difference was always observable between correlation curves obtained on surfaces incubated with and without horseradish peroxidase, the differences were

not significant. In particular, the correlation time was shorter for measurements in absence of the enzyme but the difference was often small given that substrate and cosubstrate concentrations were the same. Likewise, no conclusion about the origin from the intensity fluctuations can be drawn from the inspection of high resolution time-traces (see Fig. 9.7).

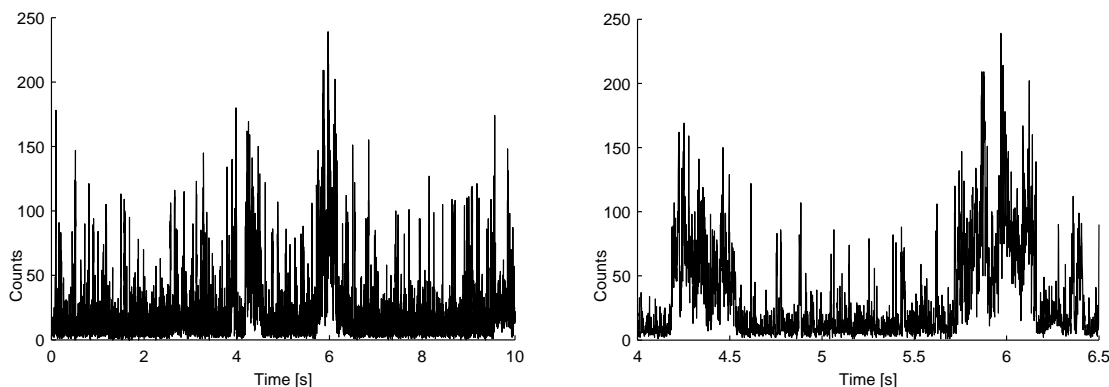


Figure 9.7: Time-trace for a negative control (left). Binning time is 1 ms . A detail of this time-trace is shown on the right.

We interpret the broad shape of the correlation curves visible for some control measurements as being due to binding of Rh6G molecules to the surface. From the presented measurements one can draw the conclusions, that either binding and enzyme catalysis are not (or not easily) distinguishable by means of the intensity fluctuation autocorrelation and / or the data obtained on slides incubated with the enzyme shows simply binding of Rh6G to the surface. The limiting problem is obviously the interaction between rhodamine 6G and the glass surface. This interaction is not homogeneous but as is also evident from measurements described in chapter 8 more pronounced on discrete spots. Even if the preparation of the slides was done very carefully the surface density of these spots is not a reproducible parameter, which jeopardizes the attempt to distinguish enzymatic reactions and binding by statistical means.

The obtained results suggest several solutions. Alternative surface preparation protocols have to be considered in order to further reduce the interaction of the dye Rh6G with the surface. However, since the origin of the interactions is unknown, finding a more appropriate protocol is not straight forward. Labeling of the enzyme can be considered which would allow to find the enzyme on the surface before initiating the catalysis by adding the substrate and / or cosubstrate. This task could be simplified if we were able to align the fiber-end with the image of a particular position in the sample using the TIRFM camera image. This necessitates that the mapping between positions in the camera image and positions in the plane of the fiber-end is known. Alignment can be achieved in principle by using a mask situated in an intermediate image-plane between the objective and the beam-splitter dividing the detection path into two paths leading to the SPAD and the camera, respectively.

Chapter 10

Conclusions and outlook

A novel method to perform FCS measurements on surfaces, called objective-type TIR-FCS, has been developed. Here, total internal reflection achieved by means of an objective-type TIRFM setup is used in order to excite fluorescence inside an evanescent field close to the surface of a microscope coverslip.

A thorough characterization of this method has been performed on a theoretical as well as an experimental level. The proposed setup features an observation volume that is confined to the proximity of the surface. Numerical calculations showed that the axial extent of the observation volume is typically smaller than $100\ \mu\text{m}$, a value that is in good agreement with results obtained from diffusion measurements. The confinement of the observation volume to the surface constitutes a real advantage if the studied molecular system is bound to the surface. This advantage consists mainly in smaller background (relative to the signal) from freely diffusing fluorescent molecules and from scattered light.

Excellent performance in terms of signal strength and signal-to-background ratio has been demonstrated by diffusion measurements and measurements on molecules binding to the surface of a microscope cover slide. Very high photon count rates per molecule could be obtained in experiments on diffusing and binding fluorophores. The high count rates are mainly due to the well known modification of the fluorescence radiation pattern occurring for fluorophores close to an interface between dielectric media. This fact is harnessed by the use of a high NA oil-immersion objective in an objective-type configuration, resulting in a collection efficiency that is about two times higher when compared to common FCS methods.

The autocorrelation function of fluorophores diffusing and binding to a single, localized binding site has been derived. This function at hand, binding rates can be obtained by means of FCS measurements for ligands binding to a single receptor. Experiments on diffusing and binding molecules showed the applicability of the derived mathematical models. Results for diffusion measurements, in particular diffusion times and the structure parameter were in accordance with theory. Experiments on binding molecules showed the applicability of our method to investigate binding kinetics on a single molecule level.

Several measurements have been performed in order to investigate enzymatic turnover on a single molecule level. Important steps were undertaken towards this goal. Limitations were identified and solutions proposed.

Furthermore, a novel method to perform fluorescence lifetime imaging based on multiplexed imaging combined with TCSPC was proposed. A theoretical investigation, which shows advantages and limitations of the proposed method was performed.

We showed that objective-type TIR-FCS is a powerful alternative to the well-established confocal FCS if the studied molecular system is bound to a surface. The application of this method to measure binding rates on a single molecule level of biologically relevant receptor-

ligand systems will constitute the next step in our research. We believe that the exact knowledge of the average lifetime of receptor-ligand complexes as well as of the binding rates will allow to better understand and dissect the different factors influencing the efficiency of cellular signaling.

Furthermore we want to improve our approach of measuring the catalytic turnover of single enzymes. In order to avoid artifacts due to dye molecules binding to the surface we have to improve the protocol for the immobilization of the enzymes. We hope that by changing the protocol we will be able to reduce unspecific binding of dye molecules to the surface. To get a better knowledge of the surface density and the localization of immobilized enzymes we will label the enzymes with fluorophores. A TIRF image taken prior to adding the substrate will provide information about density and localization of enzymes and will enable us to exclude that more than one enzyme is present inside the observation volume. A synchronization between the position of the fiber-end within the image plane and coordinates on the TIRF images will be realized. This will allow to position the fiber-end with respect to the TIRF image and simplify the alignment of the fiber-end with the image of a single enzyme. At last, changing concentrations of the substrate as well as the cosubstrate will be simplified by using a flow cell. These improvements will enable us to perform measurements on single enzymes under perfectly controlled conditions.

Some more research work will be done in order to improve fluorescence excitation and light collection. For several applications we consider to replace the focusing of the laser beam onto the back focal plane by a ring illumination of the back focal plane. The ring has to be large enough so that at the interface all rays are incident at angles larger than the critical angle. If the beam is further collimated when passing the back focal plane, the lateral extent of the observation volume may be decreased. This will in any case reduce the lateral extent of the illuminated area, which is an advantage when using this method to measure surface diffusion, e.g. inside an immobilized membrane. A reduced size of the illuminated area will lead to a reduction of photobleaching and hence increase the time for which surface-bound fluorophores are observable.

Finally, objective-type TIR-FCS simplifies the realization of two-color fluorescence cross-correlation spectroscopy (FCCS), where two excitation wavelengths and two emission wavelengths are used. Compared to confocal FCS, the alignment of the setup becomes easier. In objective-type TIR-FCS the exciting light fields are automatically aligned since both are situated at the surface. Therefore, only the two detectors or fiber-ends have to be aligned with respect to each other. Preliminary experiments in our laboratory showed that objective-type TIR-FCS can be used to perform FCCS.

Bibliography

- [1] H. Schneckenburger, H. K. Seidlitz, and J. Eberz. New trends in photobiology (invited review) - time-resolved fluorescence in photobiology. *Journal of Photochemistry and Photobiology B-Biology*, 2(1):1–19, 1988.
- [2] J. M. Beechem and L. Brand. Time-resolved fluorescence of proteins. *Annual Review of Biochemistry*, 54:43–71, 1985.
- [3] R. Cubeddu, D. Comelli, C. D’Andrea, P. Taroni, and G. Valentini. Time-resolved fluorescence imaging in biology and medicine. *Journal of Physics D-Applied Physics*, 35(9):R61–R76, 2002.
- [4] E. A. J. Reits and J. J. Neefjes. From fixed to FRAP: measuring protein mobility and activity in living cells. *Nature Cell Biology*, 3(6):E145–E147, 2001.
- [5] R. Rigler and E. L. Elson. *Fluorescence Correlation Spectroscopy: Theory and Applications*. Springer, Berlin, 2001.
- [6] K. Palo, L. Brand, C. Eggeling, S. Jager, P. Kask, and K. Gall. Fluorescence intensity and lifetime distribution analysis: Toward higher accuracy in fluorescence fluctuation spectroscopy. *Biophysical Journal*, 83(2):605–618, 2002.
- [7] P. Kask, R. Gunther, and P. Axhausen. Statistical accuracy in fluorescence fluctuation experiments. *European Biophysics Journal with Biophysics Letters*, 25(3):163–169, 1997.
- [8] P. Kask, K. Palo, D. Ullmann, and K. Gall. Fluorescence-intensity distribution analysis and its application in biomolecular detection technology. *Proceedings of the National Academy of Sciences of the United States of America*, 96(24):13756–13761, 1999.
- [9] P. R. Selvin. Fluorescence resonance energy-transfer. In *Biochemical Spectroscopy*, volume 246 of *Methods in Enzymology*, pages 300–334. Academic Press Inc, San Diego, 1995.
- [10] E. B. Shera, N. K. Seitzinger, L. M. Davis, R. A. Keller, and S. A. Soper. Detection of single fluorescent molecules. *Chemical Physics Letters*, 174(6):553–557, 1990.
- [11] N. J. Dovichi, J. C. Martin, J. H. Jett, and R. A. Keller. Attogram detection limit for aqueous dye samples by laser-induced fluorescence. *Science*, 219(4586):845–847, 1983.
- [12] D. C. Nguyen, R. A. Keller, and M. Trkula. Ultrasensitive laser-induced fluorescence detection in hydrodynamically focused flows. *Journal of the Optical Society of America B-Optical Physics*, 4(2):138–143, 1987.
- [13] S. Weiss. Fluorescence spectroscopy of single biomolecules. *Science*, 283(5408):1676–1683, 1999.

- [14] S. Weiss. Measuring conformational dynamics of biomolecules by single molecule fluorescence spectroscopy. *Nature Structural Biology*, 7(9):724–729, 2000.
- [15] D. Magde, W. W. Webb, and E. Elson. Thermodynamic fluctuations in a reacting system - measurement by fluorescence correlation spectroscopy. *Physical Review Letters*, 29(11):705–708, 1972.
- [16] D. Magde, E. L. Elson, and W. W. Webb. Fluorescence correlation spectroscopy .2. experimental realization. *Biopolymers*, 13(1):29–61, 1974.
- [17] E. L. Elson and D. Magde. Fluorescence correlation spectroscopy .1. conceptual basis and theory. *Biopolymers*, 13(1):1–27, 1974.
- [18] D. E. Koppel. Statistical accuracy in fluorescence correlation spectroscopy. *Physical Review A*, 10(6):1938–1945, 1974.
- [19] O. Krichevsky and G. Bonnet. Fluorescence correlation spectroscopy: the technique and its applications. *Reports on Progress in Physics*, 65(2):251–97, 2002.
- [20] R. H. Webb. Confocal optical microscopy. *Reports on Progress in Physics*, 59(3):427–471, 1996.
- [21] J. B. Pawley, editor. *Handbook of Biological Confocal Microscopy*. Plenum Press, New York, 1995.
- [22] D. Axelrod, T. P. Burghardt, and N. L. Thompson. Total internal-reflection fluorescence. *Annual Review of Biophysics and Bioengineering*, 13:247–268, 1984.
- [23] D. Axelrod. Total internal-reflection fluorescence microscopy. *Methods in Cell Biology*, 30:245–270, 1989.
- [24] D. Axelrod, Edward H. Hellen, and Robert M. Fulbright. Total internal reflection fluorescence. In J. R. Lakowicz, editor, *Topics in Fluorescence Spectroscopy: Biochemical Applications*, volume 3. Plenum Press, 1992.
- [25] D. Axelrod. Total internal reflection fluorescence microscopy in cell biology. *Traffic*, 2(11):764–774, 2001.
- [26] N. L. Thompson, T. P. Burghardt, and D. Axelrod. Measuring surface dynamics of biomolecules by total internal- reflection fluorescence with photobleaching recovery or correlation spectroscopy. *Biophysical Journal*, 33(3):435–454, 1981.
- [27] N. L. Thompson and D. Axelrod. Total internal reflection-fluorescence correlation spectroscopy study of antibody surface binding-kinetics. *Biophysical Journal*, 33(2):A183–A183, 1981.
- [28] A. L. Stout and D. Axelrod. Evanescent field excitation of fluorescence by epi-illumination microscopy. *Applied Optics*, 28(24):5237–5242, 1989.
- [29] J. Enderlein, T. Ruckstuhl, and S. Seeger. Highly efficient optical detection of surface-generated fluorescence. *Applied Optics*, 38(4):724–732, 1999.
- [30] R. H. Austin, K. W. Beeson, L. Eisenstein, H. Frauenfelder, and I. C. Gunsalus. Dynamics of ligand-binding to myoglobin. *Biochemistry*, 14(24):5355–5373, 1975.

- [31] N. Alberding, S. S. Chan, L. Eisenstein, H. Frauenfelder, D. Good, I. C. Gunsalus, T. M. Nordlund, M. F. Perutz, A. H. Reynolds, and L. B. Sorensen. Binding of carbon-monoxide to isolated hemoglobin chains. *Biochemistry*, 17(1):43–50, 1978.
- [32] L. Edman, Z. Foldes-Papp, S. Wennmalm, and R. Rigler. The fluctuating enzyme: a single molecule approach. *Chemical Physics*, 247(1):11–22, 1999.
- [33] Bernard Valeur. *Molecular Fluorescence*. WILEY-VCH, Weinheim, 2002.
- [34] Y. Sako, S. Minoghchi, and T. Yanagida. Single-molecule imaging of EGFR signalling on the surface of living cells. *Nature Cell Biology*, 2(3):168–172, 2000.
- [35] M. Goulian and S. M. Simon. Tracking single proteins within cells. *Biophysical Journal*, 79(4):2188–2198, 2000.
- [36] J. R. Lakowicz. *Principles of Fluorescence Spectroscopy*. Kluwer Academic / Plenum Publishers, New York, 1999.
- [37] N. L. Thompson. Fluorescence correlation spectroscopy. In J. R. Lakowicz, editor, *Topics in Fluorescence Spectroscopy*, volume 1. Plenum Press, New York, 1991.
- [38] R. A. Keller, W. P. Ambrose, P. M. Goodwin, J. H. Jett, J. C. Martin, and M. Wu. Single molecule fluorescence analysis in solution. *Applied Spectroscopy*, 50(7):A12–A32, 1996.
- [39] M. J. Marton, J. L. DeRisi, H. A. Bennett, V. R. Iyer, M. R. Meyer, C. J. Roberts, R. Stoughton, J. Burchard, D. Slade, H. Y. Dai, D. E. Bassett, L. H. Hartwell, P. O. Brown, and S. H. Friend. Drug target validation and identification of secondary drug target effects using DNA microarrays. *Nature Medicine*, 4(11):1293–1301, 1998.
- [40] T. Funatsu, Y. Harada, M. Tokunaga, K. Saito, and T. Yanagida. Imaging of single fluorescent molecules and individual ATP turnovers by single myosin molecules in aqueous-solution. *Nature*, 374(6522):555–559, 1995.
- [41] R. D. Vale, T. Funatsu, D. W. Pierce, L. Romberg, Y. Harada, and T. Yanagida. Direct observation of single kinesin molecules moving along microtubules. *Nature*, 380(6573):451–453, 1996.
- [42] H. Szmazinski and J. R. Lakowicz. Optical measurements of Ph using fluorescence lifetimes and phase-modulation fluorometry. *Analytical Chemistry*, 65(13):1668–1674, 1993.
- [43] H. J. Lin, H. Szmazinski, and J. R. Lakowicz. Lifetime-based Ph sensors: Indicators for acidic environments. *Analytical Biochemistry*, 269(1):162–167, 1999.
- [44] M. E. Lippitsch, J. Pusterhofer, M. J. P. Leiner, and O. S. Wolfbeis. Fibre-optic oxygen sensor with the fluorescence decay time as the information carrier. *Analytica Chimica Acta*, 205(1-2):1–6, 1988.
- [45] H. Szmazinski and J. R. Lakowicz. Sodium green as a potential probe for intracellular sodium imaging based on fluorescence lifetime. *Analytical Biochemistry*, 250(2):131–138, 1997.
- [46] D. Phillips; D. V. O'Connor. *Time-correlated Single Photon Counting*. Academic Press, London, 1984.

- [47] T. Neumann. *Strategies for detecting DNA hybridization using surface plasmon fluorescence spectroscopy*. PhD thesis, Johannes Gutenberg University, 2001.
- [48] J. H. Jett, R. A. Keller, J. C. Martin, B. L. Marrone, R. K. Moyzis, R. L. Ratliff, N. K. Seitzinger, E. B. Shera, and C. C. Stewart. High-speed DNA sequencing - an approach based upon fluorescence detection of single molecules. *Journal of Biomolecular Structure & Dynamics*, 7(2):301–309, 1989.
- [49] S. Bambot, J. R. Lakowicz, and G. Rao. Potential applications of life-time-based, phase-modulation fluorometry in bioprocess and clinical monitoring (vol 13, pg 106, 1995). *Trends in Biotechnology*, 13(5):195–195, 1995.
- [50] M. Kollner and J. Wolfrum. How many photons are necessary for fluorescence-lifetime measurements? *Chemical Physics Letters*, 200(1-2):199–204, 1992.
- [51] J. Enderlein, P. M. Goodwin, A. VanOrden, W. P. Ambrose, R. Erdmann, and R. A. Keller. A maximum likelihood estimator to distinguish single molecules by their fluorescence decays. *Chemical Physics Letters*, 270(5-6):464–470, 1997.
- [52] J. Ricka. Evaluation of nanosecond pulse-fluorometry measurements - no need for the excitation-function. *Review of Scientific Instruments*, 52(2):195–199, 1981.
- [53] X. F. Wang, A. Periasamy, B. Herman, and D. M. Coleman. Fluorescence lifetime imaging microscopy (FLIM) - instrumentation and applications. *Critical Reviews in Analytical Chemistry*, 23(5):369–395, 1992.
- [54] R. Sanders, A. Draaijer, H. C. Gerritsen, P. M. Houpt, and Y. K. Levine. Quantitative Ph imaging in cells using confocal fluorescence lifetime imaging microscopy. *Analytical Biochemistry*, 227(2):302–308, 1995.
- [55] J. Siegel, D. S. Elson, S. E. D. Webb, K. C. B. Lee, A. Vlanclas, G. L. Gambaruto, S. Leveque-Fort, M. J. Lever, P. J. Tadrous, G. W. H. Stamp, A. L. Wallace, A. Sandison, T. F. Watson, F. Alvarez, and P. M. W. French. Studying biological tissue with fluorescence lifetime imaging: microscopy, endoscopy, and complex decay profiles. *Applied Optics*, 42(16):2995–3004, 2003.
- [56] P. J. Tadrous, J. Siegel, P. M. W. French, S. Shousha, E. N. Lalani, and G. W. H. Stamp. Fluorescence lifetime imaging of unstained tissues: early results in human breast cancer. *Journal of Pathology*, 199(3):309–317, 2003.
- [57] R. Cubeddu, A. Pifferi, P. Taroni, A. Torricelli, G. Valentini, F. Rinaldi, and E. Sorbellini. Fluorescence lifetime imaging: An application to the detection of skin tumors. *IEEE Journal of Selected Topics in Quantum Electronics*, 5(4):923–929, 1999.
- [58] H. C. Gerritsen, M. A. H. Asselbergs, A. V. Agronskaia, and Wgjh Van Sark. Fluorescence lifetime imaging in scanning microscopes: acquisition speed, photon economy and lifetime resolution. *Journal of Microscopy-Oxford*, 206:218–224, 2002.
- [59] X. F. Wang, T. Uchida, D. M. Coleman, and S. Minami. A 2-dimensional fluorescence lifetime imaging-system using a gated image intensifier. *Applied Spectroscopy*, 45(3):360–366, 1991.
- [60] K. Dowling, M. J. Dayel, M. J. Lever, P. M. W. French, J. D. Hares, and A. K. L. Dymoke Bradshaw. Fluorescence lifetime imaging with picosecond resolution for biomedical applications. *Optics Letters*, 23(10):810–812, 1998.

- [61] M. Harwit and N. J. A. Sloane. *Hadamard Transform Optics*. Academic Press, Inc., London, United Kingdom edition, 1979.
- [62] R. Kubo. Fluctuation-dissipation theorem. *Reports on Progress in Physics*, 29:255–284, 1966.
- [63] W. Bialek and S. Setayeshgar. Physical limits to biochemical signaling. *Proceedings of the National Academy of Sciences of the United States of America*, 102(29):10040–10045, 2005.
- [64] D. Axelrod, D. E. Koppel, J. Schlessinger, E. Elson, and W. W. Webb. Mobility measurement by analysis of fluorescence photobleaching recovery kinetics. *Biophysical Journal*, 16(9):1055–1069, 1976.
- [65] R. J. Cherry. Rotational and lateral diffusion of membrane-proteins. *Biochimica Et Biophysica Acta*, 559(4):289–327, 1979.
- [66] M. Eigen and G. G. Hammes. Kinetic studies of adp reactions with the temperature jump method. *Journal of the American Chemical Society*, 82(22):5951–5952, 1960.
- [67] M. Ehrenberg and R. Rigler. Rotational brownian-motion and fluorescence intensity fluctuations. *Chemical Physics*, 4(3):390–401, 1974.
- [68] S. Wennmalm, L. Edman, and R. Rigler. Conformational fluctuations in single DNA molecules. *Proceedings of the National Academy of Sciences of the United States of America*, 94(20):10641–10646, 1997.
- [69] L. Edman, S. Wennmalm, F. Tamsen, and R. Rigler. Heterogeneity in single DNA conformational fluctuations. *Chemical Physics Letters*, 292(1-2):15–21, 1998.
- [70] M. Kinjo and R. Rigler. Ultrasensitive hybridization analysis using fluorescence correlation spectroscopy. *Nucleic Acids Research*, 23(10):1795–1799, 1995.
- [71] P. Schwille, F. Oehlenschläger, and N. G. Walter. Quantitative hybridization kinetics of DNA probes to RNA in solution followed by diffusional fluorescence correlation analysis. *Biochemistry*, 35(31):10182–10193, 1996.
- [72] R. Rigler, U. Mets, J. Widengren, and P. Kask. Fluorescence correlation spectroscopy with high count rate and low-background - analysis of translational diffusion. *European Biophysics Journal with Biophysics Letters*, 22(3):169–175, 1993.
- [73] E. Haustein and P. Schwille. Ultrasensitive investigations of biological systems by fluorescence correlation spectroscopy. *Methods*, 29(2):153–166, 2003.
- [74] H. Qian and E. L. Elson. Analysis of confocal laser-microscope optics for 3-D fluorescence correlation spectroscopy. *Applied Optics*, 30(10):1185–1195, 1991.
- [75] M. Auer, K. J. Moore, F. J. Meyer-Almes, R. Guenther, A. J. Pope, and K. A. Stoekli. Fluorescence correlation spectroscopy: lead discovery by miniaturized HTS. *Drug Discovery Today*, 3(10):457–465, 1998.
- [76] S. Sterrer and K. Henco. Fluorescence correlation spectroscopy (FCS) - a highly sensitive method to analyze drug/target interactions. *Journal of Receptor and Signal Transduction Research*, 17(1-3):511–520, 1997.

- [77] S. R. Aragon and R. Pecora. Fluorescence correlation spectroscopy as a probe of molecular-dynamics. *Journal of Chemical Physics*, 64(4):1791–1803, 1976.
- [78] J. Widengren, U. Mets, and R. Rigler. Fluorescence correlation spectroscopy of triplet-states in solution - a theoretical and experimental-study. *Journal of Physical Chemistry*, 99(36):13368–13379, 1995.
- [79] Athanasios Papoulis and S. Unnikrishna Pillai. *Probability, Random Variables and Stochastic Processes*, volume 1. McGraw-Hill, New York, 4 edition, 2002.
- [80] S. T. Hess, S. H. Huang, A. A. Heikal, and W. W. Webb. Biological and chemical applications of fluorescence correlation spectroscopy: A review. *Biochemistry*, 41(3):697–705, 2002.
- [81] R.W. Woods. *Physical Optics*. Macmillan, New York, 3 edition, 1934.
- [82] J. Schmoranzner, M. Goulian, D. Axelrod, and S. M. Simon. Imaging constitutive exocytosis with total internal reflection fluorescence microscopy. *Journal of Cell Biology*, 149(1):23–31, 2000.
- [83] N. L. Thompson and D. Axelrod. Surface binding rates of non-fluorescent molecules may be obtained by total internal-reflection fluorescence correlation spectroscopy (TIR FCS). *Biophysical Journal*, 37(2):A355–A355, 1982.
- [84] R. L. Hansen and J. M. Harris. Measuring reversible adsorption kinetics of small molecules at solid/liquid interfaces by total internal reflection fluorescence correlation spectroscopy. *Analytical Chemistry*, 70(20):4247–4256, 1998.
- [85] R. L. Hansen and J. M. Harris. Total internal reflection fluorescence correlation spectroscopy for counting molecules at solid/liquid interfaces. *Analytical Chemistry*, 70(13):2565–2575, 1998.
- [86] T. E. Starr and N. L. Thompson. Local diffusion and concentration of IGG near planar membranes: Measurement by total internal reflection with fluorescence correlation spectroscopy. *Journal of Physical Chemistry B*, 106(9):2365–2371, 2002.
- [87] A. M. Lieto, R. C. Cush, and N. L. Thompson. Ligand-receptor kinetics measured by total internal reflection with fluorescence correlation spectroscopy. *Biophysical Journal*, 85(5):3294–3302, 2003.
- [88] K. S. McCain and J. M. Harris. Total internal reflection fluorescence-correlation spectroscopy study of molecular transport in thin sol-gel films. *Analytical Chemistry*, 75(14):3616–3624, 2003.
- [89] P. Schwille. TIR-FCS: Staying on the surface can sometimes be better. *Biophysical Journal*, 85(5):2783–2784, 2003.
- [90] J. Mertz. Radiative absorption, fluorescence, and scattering of a classical dipole near a lossless interface: a unified description. *Journal of the Optical Society of America B-Optical Physics*, 17(11):1906–1913, 2000.
- [91] J. Enderlein and M. Bohmer. Influence of interface-dipole interactions on the efficiency of fluorescence light collection near surfaces. *Optics Letters*, 28(11):941–943, 2003.

- [92] J. Enderlein. Fluorescence detection of single molecules near a solution/glass interface - an electrodynamic analysis. *Chemical Physics Letters*, 308(3-4):263–266, 1999.
- [93] E. H. Hellen and D. Axelrod. Fluorescence emission at dielectric and metal-film interfaces. *Journal of the Optical Society of America B-Optical Physics*, 4(3):337–350, 1987.
- [94] M. Nietovesperinas and E. Wolf. Generalized stokes reciprocity relations for scattering from dielectric objects of arbitrary shape. *Journal of the Optical Society of America a-Optics Image Science and Vision*, 3(12):2038–2046, 1986.
- [95] B. Richards and E. Wolf. Electromagnetic diffraction in optical systems .2. structure of the image field in an aplanatic system. *Proc.Roy.Soc.A*, 253(1274):358–379, 1959.
- [96] T. E. Starr and N. L. Thompson. Total internal reflection with fluorescence correlation spectroscopy: Combined surface reaction and solution diffusion. *Biophysical Journal*, 80(3):1575–1584, 2001.
- [97] C. T. Culbertson, S. C. Jacobson, and J. M. Ramsey. Diffusion coefficient measurements in microfluidic devices. *Talanta*, 56(2):365–373, 2002.
- [98] J. M. Berg, J. L. Tymoczko, and L. Stryer. *Biochemistry*. W. H. Freeman and Company, New York, 2002.
- [99] T. W. McKeithan. Kinetic proofreading in T-cell receptor signal-transduction. *Proceedings of the National Academy of Sciences of the United States of America*, 92(11):5042–5046, 1995.
- [100] W. S. Hlavacek, A. Redondo, H. Metzger, C. Wofsy, and B. Goldstein. Kinetic proofreading models for cell signaling predict ways to escape kinetic proofreading. *Proceedings of the National Academy of Sciences of the United States of America*, 98(13):7295–7300, 2001.
- [101] K. S. McCain, P. Schluesche, and J. M. Harris. Modifying the adsorption behavior of polyamidoamine dendrimers at silica surfaces investigated by total internal reflection fluorescence correlation spectroscopy. *Analytical Chemistry*, 76(4):930–938, 2004.
- [102] H. C. Berg and E. M. Purcell. Physics of chemoreception. *Biophysical Journal*, 20(2):193–219, 1977.
- [103] R. Zwanzig and A. Szabo. Time-dependent rate of diffusion-influenced ligand-binding to receptors on cell-surfaces. *Biophysical Journal*, 60(3):671–678, 1991.
- [104] H. P. Lu, L. Y. Xun, and X. S. Xie. Single-molecule enzymatic dynamics. *Science*, 282(5395):1877–1882, 1998.
- [105] U. Kettling, A. Koltermann, P. Schwille, and M. Eigen. Real-time enzyme kinetics monitored by dual-color fluorescence cross-correlation spectroscopy. *Proceedings of the National Academy of Sciences of the United States of America*, 95(4):1416–1420, 1998.
- [106] A. Krieg, T. Ruckstuhl, S. Laib, and S. Seeger. Real-time detection of polymerase activity using supercritical angle fluorescence. *Journal of Fluorescence*, 14(1):75–78, 2004.
- [107] O. Flomenbom, K. Velonia, D. Loos, S. Masuo, M. Cotlet, Y. Engelborghs, J. Hofkens, A. E. Rowan, R. J. M. Nolte, M. Van der Auweraer, F. C. de Schryver, and J. Klafter. Stretched exponential decay and correlations in the catalytic activity of fluctuating single lipase molecules. *Proceedings of the National Academy of Sciences of the United States of America*, 102(7):2368–2372, 2005.

Acknowledgements

It would not have been possible to accomplish this work without the help and support of many people.

First of all I would like to thank my supervisor Prof. Theo Lasser who gave me the opportunity to work in his laboratory and for his support.

I would like to thank all people who worked together with me on different research projects. Special thanks goes to Michael Gösch for his constant encouragement and never losing his humor. I would like to thank Per Rigler for the effort he put into the preparation of experiments related to the enzyme project. My special gratitude goes to Prof. Rudolf Rigler for showing me the beauty of FCS, for his (not too long) lessons on the history of single molecule detection and all his encouragement. I thank Tiemo Anhut, for supporting me in the beginning of my thesis work. I am indebted to Marcel Leutenegger and Ramachandra Rao who helped me with several numerical calculations or provided code. Special thanks goes to Marcel for having an answer to every question about informatics I could think of. I would like to thank Boris Karamata for showing me that statistical problems are best resolved in a bar with the help of several cold beer. Rainer Leitgeb for being the only person who agreed to perform the painful task of checking one of my 70 formulas long, handwritten mathematical derivations.

Many thanks to the EPFL students who worked with me on different projects. Special thanks goes to Andre Mercanzini and Patrick Servet for showing interest and motivation when realizing their semester project and diploma project, respectively.

I thank all actual and former members of the LOB for the nice time we had inside and especially outside the lab, above all: Antonio, for making many 'before-work ski-tours' to unforgettable events. Alexander Servov for the various GO games we played and the many beers he always provided at this opportunity. Markus Laubscher, Jelena Mitic, Ramachandra Rao and Ling Chin Hwang for organizing numerous evenings with a lot of good food and fun. Special thank goes to Adrian Bachman, Roland Michaely and all the members of our small running club (Yannick Fournier, Thomas Maeder, Caroline Jacq, Fabien Bourgeois, etc.) for providing a good reason to leave the lab on Wednesday noons to get some fresh air.

I would like to thank the secretaries of the Institute of Applied Optics, Judith Chaubert, Yvette Bernhard and Manuelle Borruat for helping me with administrative tasks.

My gratitude goes to all my mountaineering friends who had time to spend many nice days together with me in the alps of Switzerland and thus helped me to recharge my batteries after a long week in the lab. I would like to thank all other friends who have not been to the mountains with me (but there are few who have not) but made my live in Lausanne so enjoyable.

My acknowledgment goes to my family for their love and constant support.

Thanks to Franziska for her support and patience.

Publications

Paper I

Time-resolved Hadamard fluorescence imaging

Kai Hassler, Tiemo Anhut, and Theo Lasser

We present a new concept for fluorescence lifetime imaging (FLIM) based on time-resolved Hadamard imaging (HI). HI allows image acquisition by use of one single-point detector without requiring a moving scanning stage. Moreover, it reduces the influence of detector noise compared with raster scanning. By use of Monte Carlo simulations it could be confirmed that Hadamard transformation may decrease the error in lifetime estimation and in general in fluorescence parameter estimation when the signal-to-noise ratio is low and detector dark noise is high. This concept may find applications whenever the performance of FLIM or similar methods is limited by high dark-count rates and when the use of a single-point detector is preferable. © 2005 Optical Society of America

OCIS codes: 110.6980, 170.2520.

1. Introduction

In many applications of fluorescence spectroscopy, especially in medicine and biology, there is a need to localize specific fluorescent molecules in a given sample, which is achieved by the imaging of the emerging fluorescence emission. Moreover, if more than one fluorescent specimen is present, it is often necessary to distinguish between their fluorescence signals. The investigation of fluorescence spectra is sometimes insufficient for this purpose. Because fluorescence emission spectra are in general large, there may be spectral overlaps for different fluorophores. Furthermore, distinguishing between fluorescence signals by means of their spectra requires at least two different detection channels, which results in signal losses. Fluorescence lifetime imaging¹ (FLIM) that obtains localization and the individual fluorescence-decay times of the fluorescent specimen at the same time overcomes these problems. The measurement of the lifetime allows us to identify a fluorescent molecule, to identify a spurious background, and even to probe the microenvironment of a fluorescent molecule,^{2,3} as the lifetime may be influenced by pH,^{4,5} oxygen concentration,⁶ cation concentration,⁷ etc.

Since the first experiments that showed the technical feasibility of FLIM in the early 1990s,^{8–10} this technology has been applied to many different fields in the domain of medicine and biology. Applications include, among others, the monitoring of cell metabolism²; several fields in diagnostics, for instance, tumor detection^{11,12}; and detection of specific pathologies in ophthalmology.¹³ Recently FLIM has been used in biochip applications, for which additional information about the time behavior of fluorescence emission is used to discriminate against background fluorescence or to distinguish between different fluorophores. Several groups reported a remarkable increase in the signal-to-noise ratio (SNR) when using time-resolved imaging rather than conventional imaging in biochip reading.^{14,15}

FLIM is usually performed by time-resolved scanning¹⁶ of a sample or by parallel acquisition with an intensified CCD camera with high time resolution.^{10,17} We report a new approach, wherein a multiplexing technique based on Hadamard transformation is used to acquire a time-resolved fluorescence image. The resulting method, which we call Hadamard lifetime imaging (HLI), has in certain cases several advantages compared with the methods mentioned before. First, as for scanning, for HLI, only a single-point detector is needed. Second, HLI compared with single-point scanning increases the SNR in the different time channels of the decay histograms if the SNR is low and the detector dark noise is high. This translates to a significant reduction of uncertainty in fluorescence-lifetime estimation and in general in fluorescence parameter estimation. In this paper we show theoretically by using Monte Carlo simulations that

K. Hassler (kai.hassler@epfl.ch) and T. Lasser are with the Ecole Polytechnique Fédérale de Lausanne, Laboratoire d'Optique Biomédicale, CH-1015 Lausanne, Switzerland. T. Anhut is with the Fraunhofer Institut für Biomedizinische Technik, D-66386 St. Ingbert, Germany.

Received 19 April 2005; accepted 7 July 2005.

0003-6935/05/357564-09\$15.00/0

© 2005 Optical Society of America

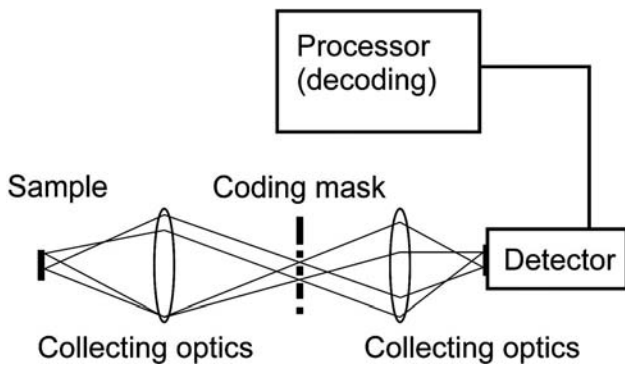


Fig. 1. Schematic representation of a HI device.

HLI outperforms the scanning method given the above-mentioned circumstances (low SNR, high detector dark noise). This makes it an interesting alternative to established FLIM techniques.

2. Theory

A. Hadamard Imaging

To perform imaging, detector arrays may be used in the visible or the near-infrared spectral region. Alternatively, if detector arrays are not available for the spectral region of interest, one can perform a raster scan of the sample by using a single-point detector. Hadamard imaging^{18,19} (HI) is a combination of these two techniques with the advantage that only a single-point detector is needed. Moreover, it may provide a multiplexing advantage compared with scanning, known as the Fellgett advantage,²⁰ which consists of a decrease of noise induced by the detector.

By raster scanning, small spatial regions of the sample are observed successively, each one corresponding to one pixel on the image finally obtained. In the case of HI a special weighing design is employed, whereby the signal from a spatial subset of pixels on the sample is measured. (To denote the preimage of a pixel, which is located on the sample, we use here and in the following discussion the same term: pixel.) The difference between signals from the subset and its complement are recorded equally well. This is realized by use of a mask or rather subsets of a mask, which are consecutively applied to block the light emitted from one subset of pixels and transmit the light from the complementary subset. Figure 1 shows a simple scheme for such an imaging system in which the mask is placed in the observation path.

Alternatively, a mask may be used to modulate the light in the illumination path, creating an illumination pattern on the sample. Measuring the difference of signals may be realized by use of two detectors and a mask that directs the signal emerging from one pixel to either the first or the second detector. Directing of light from one pixel to different detectors can be achieved by use of micromirror devices²¹ or similar spatial light modulators. As an alternative, one may use only one detector and measure the positive and negative signals at different times, in which case a

mask that is either blocking or transmitting light has to be used. This can be realized by use of moving mechanical masks, micromirror devices, or liquid-crystal arrays. No moving of the sample by means of a scanning stage or similar technology is needed in the latter cases. The subset to be taken for the j th measurement is defined by the rows of a Hadamard matrix \mathbf{H} or an S matrix.¹⁹ In what follows we restrict ourselves to the discussion of Hadamard matrices. A Hadamard matrix of the order of n is fully characterized by the following four properties¹⁸:

$$H_{ji} = \pm 1, \quad (1)$$

$$\sum_{i=1}^n H_{ji} = 0, \quad \forall j \neq 1, \quad (2)$$

$$\mathbf{H} = \mathbf{H}^T, \quad (3)$$

$$\mathbf{H}^{-1} = \frac{1}{n} \mathbf{H}, \quad (4)$$

where the H_{ji} are the components of \mathbf{H} and T denotes the transpose. A sufficient condition for \mathbf{H} to exist is that its order is 1, 2, or a multiple of 4. For two matrices \mathbf{H}_n and \mathbf{H}_m (where the subscripts refer to the order of the matrices) we can construct $\mathbf{H}_{n \times m}$ by replacing in \mathbf{H}_m positive entries with \mathbf{H}_n and negative entries with $-\mathbf{H}_n$. In this way all matrices of the order of $n = 2^k$, $k = 1, 2, 3, \dots$, can be constructed from

$$\mathbf{H}_2 = \begin{bmatrix} 1 & 1 \\ 1 & -1 \end{bmatrix}. \quad (5)$$

One row of \mathbf{H} (subscripts indicating the order will again be suppressed in the following) corresponds to one measurement and therefore to one subset of the mask, whereas each column corresponds to one pixel and the entry at this position tells us whether we have to subtract or add the signal emitted from this pixel for the current measurement. The j th measurement outcome y_j is thus a linear transformation of all signals x_{ij} , where

$$x_{ij} = \langle X_i \rangle + q_{ij}. \quad (6)$$

Here i is the pixel number, $\langle \rangle$ indicates the expected value, $\langle X_i \rangle$ is the expected value for the signal emerging from the i th pixel, and the q_{ij} are the corresponding statistical fluctuations, satisfying $\langle q_{ij} \rangle = 0$. In matrix notation, \mathbf{y} may be written as

$$\mathbf{y} = \text{diag}(\mathbf{H}\mathbf{x}), \quad (7)$$

where $\text{diag}(\)$ means the diagonal of the matrix. Because \mathbf{H} is invertible, another linear transformation allows us to recover estimates z_i for the original signals:

$$\mathbf{z} = \mathbf{H}^{-1}\mathbf{y} = \mathbf{H}^{-1} \text{diag}(\mathbf{H}\mathbf{x}). \quad (8)$$

Note that the simple raster scanning can be described in a similar way with the difference that the applied weighing design is defined by the identity matrix:

$$\mathbf{y} = \text{diag}(\mathbf{I}\mathbf{x}). \quad (9)$$

HI may be advantageous compared with scanning if noise induced by the detector is present. Let us consider an idealized situation with no other noise sources except the statistical nature of fluorescence emission and the detector. Both contribute noise that we suppose to be independent of signal strength and time. Let e_j denote the noise induced by the detector for the j th measurement satisfying $\langle e_j \rangle = 0$. The estimates \mathbf{z} are then given by

$$\mathbf{z} = \langle \mathbf{X} \rangle + \mathbf{H}^{-1} \text{diag}(\mathbf{H}\mathbf{q}) + \mathbf{H}^{-1}\mathbf{e}. \quad (10)$$

The variance in the case of Hadamard transformation reads

$$\sigma_h \circ \sigma_h = \langle [\mathbf{H}^{-1} \text{diag}(\mathbf{H}\mathbf{q}) + \mathbf{H}^{-1}\mathbf{e}] \circ [\mathbf{H}^{-1} \text{diag}(\mathbf{H}\mathbf{q}) + \mathbf{H}^{-1}\mathbf{e}] \rangle, \quad (11)$$

where \circ denotes elementwise multiplication. Assuming that the distributions for q_{ij} and e_j are the same for all measurements j , we write $\langle e^2 \rangle = \langle e_j^2 \rangle$. It turns out that the standard deviation is the same for all pixels i and we may write $\sigma_h = (\sigma_h)_i$. Using properties (1)–(4) and assuming further that all random variables q_{ij} and e_j are independent, we finally derive

$$\sigma_h = \frac{1}{\sqrt{n}} \sqrt{\langle \text{diag}(\mathbf{q}) \cdot \text{diag}(\mathbf{q}) \rangle + \langle e^2 \rangle}. \quad (12)$$

A scanning of the sample yields the estimates

$$\mathbf{z} = \langle \mathbf{X} \rangle + \text{diag}(\mathbf{q}) + \mathbf{e}. \quad (13)$$

In this case \mathbf{z} is known with the standard deviation

$$\sigma_{sc} = \sqrt{\text{diag}(\langle \mathbf{q} \circ \mathbf{q} \rangle) + \langle \mathbf{e} \circ \mathbf{e} \rangle}. \quad (14)$$

We recover the well-known result that the Hadamard transformation decreases the noise induced by the detector by a factor of $(1/n)^{1/2}$ when compared with raster scanning. Note, however, that in the case of HI the photon noise (\mathbf{q}) is averaged over the whole image. This is actually a drawback if the dynamic range of the image is high, as the photon-noise contribution will be increased for dark regions.

B. Hadamard Lifetime Imaging

FLIM by time-correlated single-photon counting²² (TCSPC) consists of recording a fluorescence-decay histogram for each pixel. The heart of a TCSPC sys-

tem is a pulsed light source, typically a laser emitting pulses with a duration in the picosecond range, a fast detector, and a time-to-amplitude converter. Each detected photon starts a linear voltage ramp, and the next excitation pulse stops the ramp. The voltage that corresponds to a certain delay between the detection of a photon emitted by a fluorophore and the succeeding excitation pulse is converted into an address of a register and the corresponding entry is incremented by one. In this way a histogram is generated that represents the number of counts as a function of time after excitation.

Several different methods exist for calculating the lifetimes from the recorded histograms.²² Among them, the most commonly used are linear least-squares fitting, the method of moments, the least-squares method with iterative reconvolution, the Laplace transform method, the Fourier transform method, the phase-plane method, the modulating-functions method, the exponential-series method, and the maximum-likelihood method. It is known that the maximum-likelihood method is the best choice if the number of counted photons is low, since the estimates it yields are unbiased and their variances are minimal.^{23–25} The uncertainty in the estimation of the lifetime, regardless of the method used, results from statistical fluctuations of counts in the time channels of the histogram. These fluctuations are partly due to the random character of fluorescence emission and obey in general Poisson statistics. Depending on the signal strength, detector dark counts can make a considerable contribution to the overall number of counts. As they also arise from a random process, they contribute to statistical fluctuations, especially in time channels where the fluorescence signal is weak (that means for times longer than the fluorescence-decay time). For small overall signal count rates it is therefore important to minimize the detector noise, which we may achieve, for instance, by cooling the detector or, as we propose, by applying the Hadamard transformation. The method we propose is essentially HI with the difference that for each mask subset a full histogram is recorded by TCSPC.

When a Hadamard transformation is applied to fluorescence-decay histograms, the probability distribution for counts is modified. Hence statistical estimators for the decay time have to be modified too. We have chosen a maximum-likelihood estimator for the above-mentioned advantages. Given a data set and a model for the data, the maximum-likelihood estimator maximizes the likelihood function, which is the probability of finding the particular data set as a result of our measurement. In the following discussion we derive the exact form of the likelihood function.

The likelihood $L(\tau_i)$ as a function of the fluorescence-decay time τ_i for a particular pixel i has in our case the form

$$L(\tau_i) = \prod_{i=1}^m P_{Z_{ii}}(z_{ii} | \tau_i; \langle D \rangle, \{\langle z_{ji} \rangle j \neq i\}). \quad (15)$$

Here $\langle D \rangle$ is the expected number of dark counts per pixel, detector, and time channel. The likelihood is a product over the conditional probability distributions $P_{Z_{il}}$ for the different time channels l because the counts Z_{il} in different channels are independent random variables. Please note that the $P_{Z_{il}}$ depend on the signals emerging from all pixels. The maximum-likelihood estimate is the value $\hat{\tau}_i$ for which the likelihood function is maximal:

$$\hat{\tau}_i = \arg\left\{\max_{\tau_i}[L(\tau_i)]\right\}. \quad (16)$$

Below we derive the exact form for the probability mass function of measurands after they undergo a Hadamard transformation and backtransformation. Let the random variables Y_j contain the Hadamard encoded measurement data and let X_{ij} be the original Poisson-distributed signals (for one specific time channel). To begin, we restrict our discussion to the case of no detector noise. The measurement generates a transformation of the variables \mathbf{X} :

$$\mathbf{Y} = \text{diag}(\mathbf{H}\mathbf{X}). \quad (17)$$

The data processing corresponds to the inverse transformation

$$\mathbf{Z} = \mathbf{H}^{-1}\mathbf{Y} \quad (18)$$

$$= \frac{1}{n} \mathbf{H} \text{diag}(\mathbf{H}\mathbf{X}). \quad (19)$$

This may be written as a difference between two sums over the random variables \mathbf{X} :

$$Z_i = \frac{1}{n} [\text{Tr}(\mathbf{A}_i^+ \mathbf{X}) - \text{Tr}(\mathbf{A}_i^- \mathbf{X})], \quad (20)$$

where $\text{Tr}(\cdot)$ means that the trace of the argument is taken. The sum over n independent Poisson random variables has again a Poisson distribution, and transformation (19) turns out to be a difference between the two Poisson random variables $\text{Tr}(\mathbf{A}_i^+ \mathbf{X})$ and $\text{Tr}(\mathbf{A}_i^- \mathbf{X})$. The matrices \mathbf{A}_i^\pm with components $\mathbf{A}_{ijk}^\pm \equiv (\mathbf{A}_i^\pm)_{jk}$ are defined by (no summation over indices)

$$\mathbf{A}_{ijk}^+ := \Theta(H_{ij} H_{jk}), \quad (21)$$

$$\mathbf{A}_{ijk}^- := \Theta(-H_{ij} H_{jk}), \quad (22)$$

where Θ is the Heaviside step function defined by

$$\Theta(x) := \begin{cases} 0, & x < 0 \\ \frac{1}{2}, & x = 0 \\ 1, & x > 0 \end{cases}. \quad (23)$$

Note that \mathbf{A}_i^+ has only ones in the i th column but $n/2$

ones and the rest zeros in each column $j \neq i$. This is due to Eqs. (1) and (3):

$$\mathbf{A}_{iji}^+ = \Theta(H_{ij} H_{ji}) = (H_{ij})^2 = 1, \quad \forall j. \quad (24)$$

In consequence of Eqs. (1), (4), and (21) it is also clear that

$$\sum_{j=1}^n H_{ij} H_{jk} = 0, \quad \forall i \neq k, \quad (25)$$

$$\Rightarrow \sum_{j=1}^n \mathbf{A}_{ijk}^+ = \frac{n}{2}, \quad \forall i \neq k. \quad (26)$$

In the same manner we find that \mathbf{A}_i^- has only zeros in the i th column and $n/2$ ones and $n/2$ zeros in each column $j \neq i$. For the probability mass function of \mathbf{Z} we may write

$$P_{Z_i}(z_i) = P_{\frac{1}{n}[\text{Tr}(\mathbf{A}_i^+ \mathbf{X}) - \text{Tr}(\mathbf{A}_i^- \mathbf{X})]}(z_i) = P_{\text{Tr}(\mathbf{A}_i^+ \mathbf{X}) - \text{Tr}(\mathbf{A}_i^- \mathbf{X})}(nz_i) \quad (27)$$

for all z_i , where nz_i is an integer. It is well known that the probability mass function of the sum of several random variables is a convolution of the original mass functions:

$$P_{R+S+T+\dots}(w) = P_R * P_S * P_T * \dots | w, \quad (28)$$

whereas the probability mass function of the difference of two random variables is given by the correlation of the two original mass functions:

$$P_{R-S}(u) = P_R \star P_S | u. \quad (29)$$

We assume that the original signals are Poisson random variables. Using the explicit form of a Poisson probability distribution for a variable R ,

$$P_R(r) = \frac{\langle R \rangle^r}{r!} \exp(-\langle R \rangle), \quad (30)$$

we calculate the correlation for the two random variables R and S :

$$\begin{aligned} P_U(u) &= \sum_{k=0}^{\infty} P_R(u+k) P_S(k) \\ &= \exp[-(\langle R \rangle + \langle S \rangle)] \langle R \rangle^u \sum_{k=0}^{\infty} \frac{(\langle R \rangle \langle S \rangle)^k}{k! (u+k)!}. \end{aligned} \quad (31)$$

We recall the modified Bessel functions:

$$I_n(z) = \left(\frac{z}{2}\right)^n \sum_{k=0}^{\infty} \frac{\left(\frac{z^2}{4}\right)^k}{k! (k+n)!}, \quad (32)$$

where n is an integer. Writing $z = 2\sqrt{\langle R \rangle \langle S \rangle}$ and substituting Eq. (32) into Eq. (31) leads to²⁶

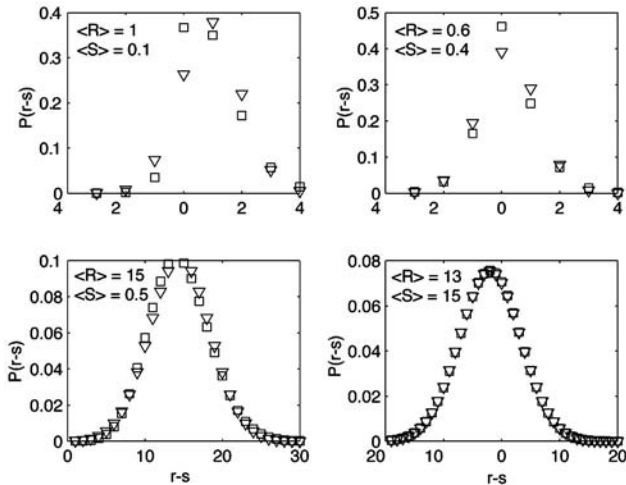


Fig. 2. Probability distributions for the difference of two Poisson random variables. Open squares, exact distribution; open inverted triangles, Gaussian approximation.

$$P_U(u) = \exp[-(\langle R \rangle + \langle S \rangle)] \left(\frac{\langle R \rangle}{\langle S \rangle} \right)^{u/2} I_u(2\sqrt{\langle R \rangle \langle S \rangle}). \quad (33)$$

This distribution has the mean value $\langle U \rangle = \langle R \rangle - \langle S \rangle$ and a variance given by the sum of the variances σ_R and σ_S . An approximation by a Gaussian distribution is valid if $\langle R \rangle \gg 1$ or if $\langle S \rangle \gg 1$. This behavior is apparent in Fig. 2, which shows a comparison between the distribution of Eq. (33) and approximations by a Gaussian for different parameters $\langle R \rangle$ and $\langle S \rangle$.

Keeping in mind the properties of \mathbf{A}_i^\pm mentioned above, we easily find that

$$\langle \text{Tr}(\mathbf{A}_i^+ \mathbf{X}) \rangle = \frac{n}{2} \langle X_i \rangle + \frac{n}{2} \sum_{j=1}^n \langle X_j \rangle, \quad (34)$$

$$\langle \text{Tr}(\mathbf{A}_i^- \mathbf{X}) \rangle = -\frac{n}{2} \langle X_i \rangle + \frac{n}{2} \sum_{j=1}^n \langle X_j \rangle. \quad (35)$$

Here $\langle X_i \rangle = \langle X_{ij} \rangle$ is independent of j , i.e., the actual measurement. $P_{\text{Tr}(\mathbf{A}_i^+ \mathbf{X})}(x)$ is a Poisson distribution with mean $\langle \text{Tr}(\mathbf{A}_i^+ \mathbf{X}) \rangle$, and $P_{\text{Tr}(\mathbf{A}_i^- \mathbf{X})}(x)$ is a Poisson distribution with mean $\langle \text{Tr}(\mathbf{A}_i^- \mathbf{X}) \rangle$. With Eqs. (33) and (27) we derive

$$P_{Z_i}(z_i) = \exp[-(\langle V_i \rangle + \langle W_i \rangle)] \times \left(\frac{\langle V_i \rangle}{\langle W_i \rangle} \right)^{nz_i/2} I_{nz_i}(2\sqrt{\langle V_i \rangle \langle W_i \rangle}), \quad (36)$$

where

$$\langle V_i \rangle := \langle \text{Tr}(\mathbf{A}_i^+ \mathbf{X}) \rangle, \quad (37)$$

$$\langle W_i \rangle := \langle \text{Tr}(\mathbf{A}_i^- \mathbf{X}) \rangle. \quad (38)$$

If (Poisson-distributed) dark counts are present (each of the two detectors contributes on average $\langle D \rangle$ dark counts), we derive in a similar way

$$\langle V_i \rangle := \langle \text{Tr}(\mathbf{A}_i^+ \mathbf{X}) \rangle + n\langle D \rangle, \quad (39)$$

$$\langle W_i \rangle := \langle \text{Tr}(\mathbf{A}_i^- \mathbf{X}) \rangle + n\langle D \rangle. \quad (40)$$

When $n \sum_j \langle X_j \rangle \gg 1$ the above probability distribution may be approximated by a Gaussian distribution. When applied to lifetime imaging, Eq. (36) is the probability distribution for counts in one time channel and $n \sum_j \langle X_j \rangle$ may be small for channels corresponding to late times. If there is a considerable amount of dark counts contaminating the data, an approximation by a Gaussian distribution may even hold for late time channels. However, as simulations showed, the CPU time needed to calculate lifetimes for Hadamard data is nearly the same for an algorithm incorporating the exact probability distribution or the Gaussian approximation.

3. Results

To estimate the benefit of HLI with respect to conventional lifetime imaging by linear scanning, we generated large sets of simulated fluorescence-decay data for varying portions of contaminating dark counts and different parameters such as decay time, spatial or time resolution, etc. The simulations we performed describe an idealized situation in the sense that the instrument response function of the measurement apparatus was approximated by a δ distribution, and no afterpulsing and no photobleaching were taken into account. The disregard of afterpulsing is justified by the fact that the fluorescence signal count rate is of the order of the detector dark-count rate in the investigated data sets; hence afterpulsing is in fact negligible with respect to the dark-count rate.

Photobleaching of the fluorophores may distort the data obtained by HI,^{27,28} as in this case the light falling on the submasks becomes a function of time. Nevertheless we can correct for this distortion by modifying the matrix describing the backtransformation. Another possibility consists of performing several measurement cycles and summing up the data sets for successive measurements to decrease the integration time per mask subset. At the end the number of counts per pixel is the same, but the effect of photobleaching on the time scale of one measurement cycle is negligible if the time for one cycle is small compared with the characteristic bleaching time. Photobleaching will still reduce the overall number of collected photons but no longer distort the data. However, if the photobleaching is very high, the SNR for HI can decrease beyond the value obtained for scanning. This is because the average count rate per pixel in the presence of bleaching will be smaller for HI than for scanning. Probably this disadvantage can be eliminated in the future if nanoparticles are used instead of classical fluorophores. Recent research showed that these particles may become valuable surrogates for fluorophores, exhibiting in particular the advantage that they are not subject to photobleaching.²⁹

To simulate the Hadamard measurement, a Monte Carlo approach was used to generate one histogram

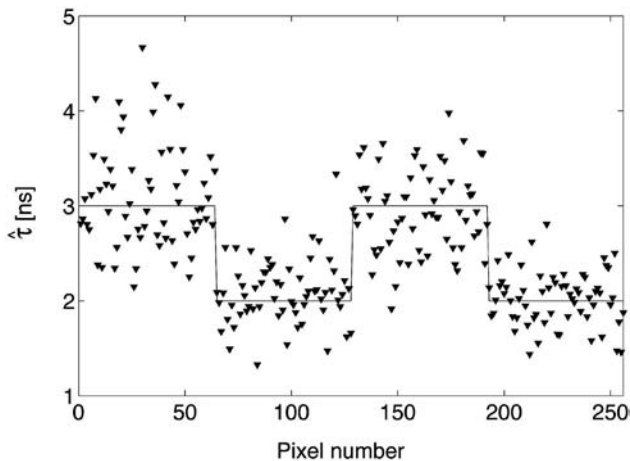


Fig. 3. Result of a simulation for lifetime imaging by scanning. Solid line, real lifetime distribution; triangles, estimates.

per pixel and subset of the mask (submask). The data were subsequently transformed according to Eq. (7). At this stage, uniformly distributed dark counts were added to the data, which were backtransformed afterwards. In the case of conventional lifetime imaging, one histogram per pixel was generated and subsequently contaminated by dark counts.

Figures 3 and 4 show results for lifetime imaging and HLI simulations. The parameters were the same in both cases: fluorescence-decay time, either 3 or 2 ns; 90% dark counts; 256 pixels; 512 channel time resolution corresponding to a measurement window of 25 ns. Because in reality two detectors have to be used for HLI, whereas one is sufficient for scanning, we assumed the double virtual measurement time in the case of the scanning measurement to compare the two methods on a fair basis. The average count number for one pixel was 3000 (HLI) and 6000 (scanning) per submask. The solid lines in both graphs indicate the actual lifetime distributions, which have been superposed for comparison. In both cases a maximum-likelihood approach was used to analyze

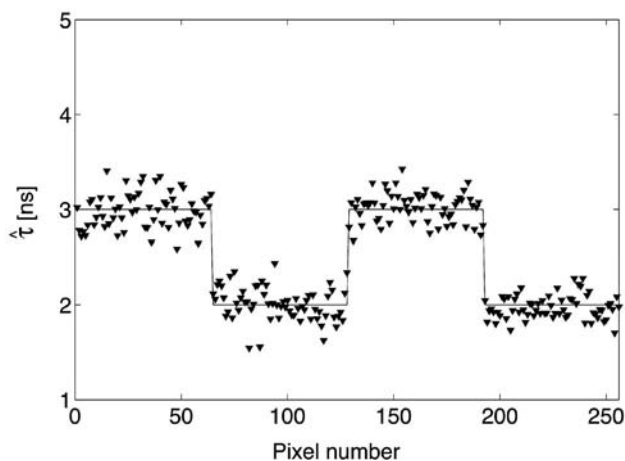


Fig. 4. Simulation with the same parameters as for Fig. 3, based on HLI.

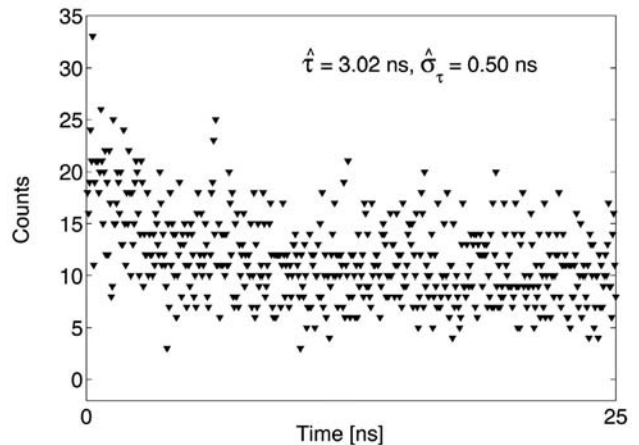


Fig. 5. Scanning approach: histogram obtained for one pixel.

the data sets. A net decrease of the estimator variance is visible in the case of HLI with respect to the standard approach. This decrease in the variance is mainly due to a suppression of dark-count noise in later time channels, as is visible in Figs. 5 and 6, which show the histograms for one pixel in the case of scanning and HLI, respectively.

The benefit of HLI depends on the portion of noise that is due to dark counts in the overall noise level [see Eqs. (12) and (14)]. To further investigate this dependence, we performed simulations for varying background ratios and compared the standard deviations σ_h (for HLI) and σ_{sc} (for the scanning method) of the estimator $\hat{\tau}$ (see Fig. 7). We have chosen the parameters as above, but τ is now 2.5 ns and we have restricted the number of pixels to 32. The expected number of dark counts per channel $\langle D \rangle$ varies between 0 and 5.22 (0% and 90%) in steps of 0.29. Again, the signal strength is the same for all pixels and the variance of τ was calculated for a sample consisting of the set of all pixels (respectively histograms) generated for a certain background value and method. Twenty full images were generated per method and background value.

For small dark-count rates the variance of τ is approximately a factor of 2 smaller for the conventional

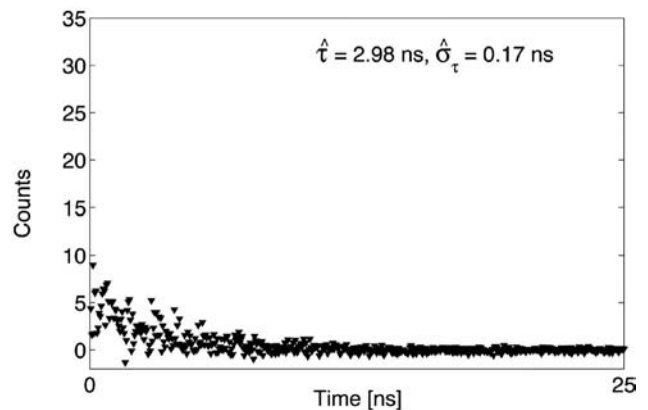


Fig. 6. HLI: histogram obtained for one pixel.

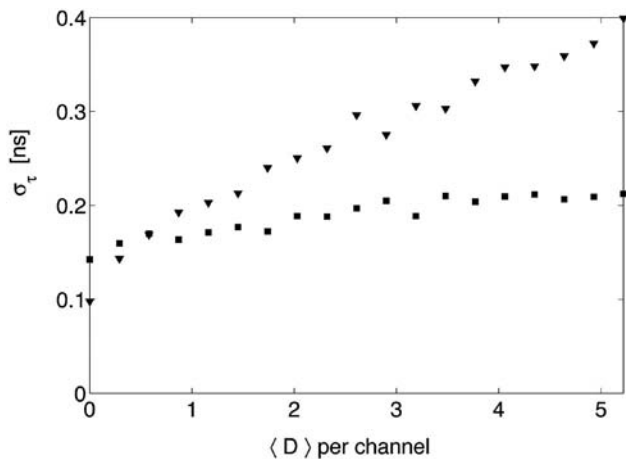


Fig. 7. Standard deviations of the estimator \hat{r} . Filled squares, HLLI; filled inverted triangles, lifetime imaging, scanning approach.

method, which is because we allowed the signal to be two times higher. When the dark count rate increases, the standard deviation increases for the conventional method but increases much slower for HLLI, which is not surprising since it suppresses the noise that is due to detector dark counts. The suppression of this noise becomes even more pronounced when the number of pixels increases and the standard deviation as a function of dark counts approaches a constant.

In medical diagnostics it is frequently the case that a fluorescence signal with a known lifetime is used for detecting pathological tissue. The measured signal consists of the fluorescence emitted by a certain tissue component or an exogenous marker, which has to be distinguished from fluorescence emitted by any tissue.^{1,30,31} In biochip applications, a similar problem is faced when dyes with different known lifetimes are used to label distinct targets.^{14,15} Therefore we investigated the question for the benefit of Hadamard transformation if the unknown variable is not the lifetime but the ratio between two fluorescence signals with different, but known, lifetimes. The approach to analyzing the data set remains the same, but the likelihood function L now becomes

$$L(r) = \prod_{i=1}^m P_{z_{il}}(z_{il} | r; \tau_1, \tau_2, \langle D \rangle, \{z_{jl} | j \neq i\}), \quad (41)$$

where $r = \langle S(\tau_1) \rangle / \langle S(\tau_2) \rangle$; $S(\tau_i)$ is the number of collected photons emitted by the fluorophore with decay time τ_i .

Figures 8 and 9 show the estimated ratios for a data set generated with the following parameters: τ_1 and τ_2 have the values 4 and 1 ns, respectively. The overall number of pixels is 256, each pixel corresponding to a histogram of 512 channels within a measurement window of 25 ns. The data are contaminated by 90% background. The number of counts per pixel is 3000 (HLLI) and 6000 (scanning). Again a net decrease in the fluctuation of the estimate is visible when HLLI is applied. This is most visible for the

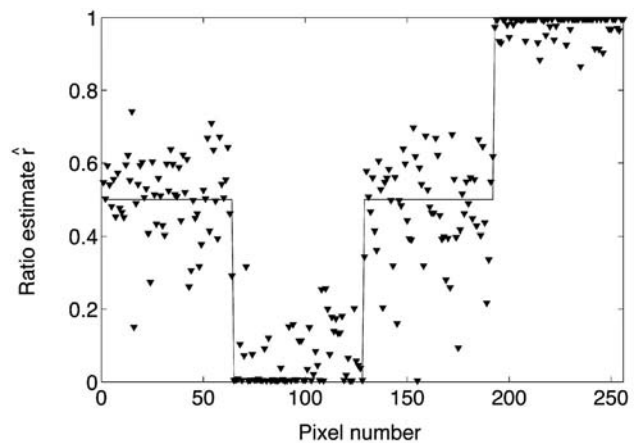


Fig. 8. Estimates for the ratio r of fluorescence signals with decay times of 4 and 1. Solid line, real values of r . Scanning was simulated.

regions where $r = 0.5$. The standard deviation for r was estimated from a sample containing 1024 pixels; r was 0.5 and the other parameters were as for previous simulations. We obtained $\sigma_h = 0.058$ for HLLI, whereas for the conventional method we obtained $\sigma_{sc} = 0.173$, which is approximately three times larger.

In several applications (see, e.g., Ref. 32) there is no need to estimate fluorescence lifetimes, but rather one must distinguish among a number of fluorophores with already-known lifetimes. This may be done with the likelihood criterion, which is known to give the best results in terms of accuracy.^{32,33} It consists of comparing the likelihoods $L(\tau_i)$ for all possible arguments τ_i and one given data set and choosing the τ_i that maximizes the likelihood function.

Figure 10 shows two data sets generated for a background of $\sim 90\%$ and lifetimes $\tau_1 = 2$ ns and $\tau_2 = 4$ ns. Hadamard transformation reduces considerably the percentage of wrongly identified fluorophores (pixels), from $\sim 19\%$ to $\sim 4\%$ in this example.

To investigate the benefit of the Hadamard method we generated 11,400 data sets containing 64 pixels

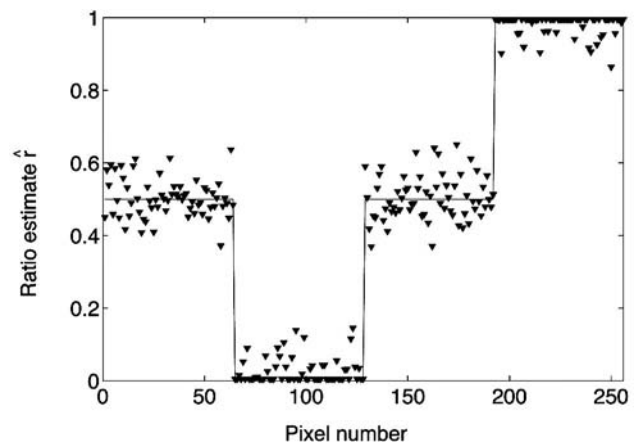


Fig. 9. HLLI simulation, estimates for r . Simulation parameters are identical to those of Fig. 8.

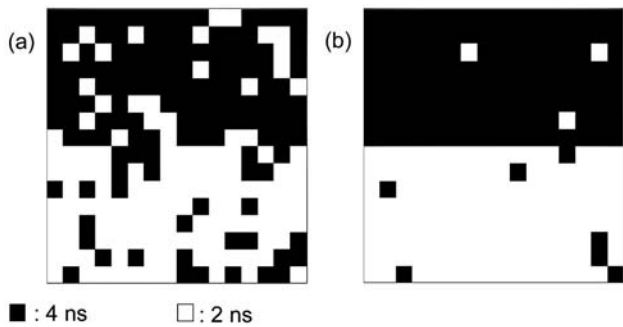


Fig. 10. Fluorophore identification for known lifetimes of 2 and 4 ns. The actual distribution of the lifetimes is 4 ns in the upper half and 2 ns in the lower half. (a) shows estimates based on raster scanning, whereas (b) was obtained by HLI. The dark counts constitute 90% of the overall signal.

each, in which each pixel emits fluorescence light, showing a decay time of either τ_1 and τ_2 in equal portions. The background was varied between zero and approximately 90% in 18 steps. We investigated pairs: $\{(\tau_1, \tau_2)\} = \{(1, 4), (1.5, 3.5), (2, 3), (2.2, 2.8), (2.3, 2.7), (2.4, 2.6)\}$ (in nanoseconds). The expected number of the overall detected fluorescence photons was in all cases 40 per pixel and detector (80 when scanning was used).

Figure 11 shows the average fluorophore misidentification rate for fluorophores with lifetimes of 1 and 4 ns. The average was taken over 50×64 pixels. Even for a low number of pixels the Hadamard transformation suppresses noise induced by dark counts so that the dark-count rate nearly does not influence the misidentification rate in a region $\langle D \rangle \in [0, 0.9]$. Whereas the misidentification rate reaches 8% for the conventional approach in this case, this rate always stays below 0.5% when HLI is applied. Figure 12 shows an example in which $(\tau_1, \tau_2) = (2 \text{ ns}, 3 \text{ ns})$; all other parameters are the same as above. When the

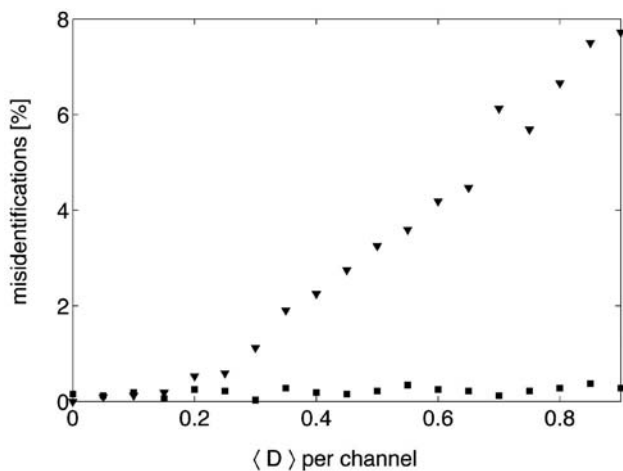


Fig. 11. Errors in fluorophore identification. The graphs show the average number of misidentified pixels per picture as a function of dark counts; $(\tau_1, \tau_2) = (1 \text{ ns}, 4 \text{ ns})$. Filled squares, estimates obtained with Hadamard transformation; filled inverted triangles, estimates obtained with scanning.

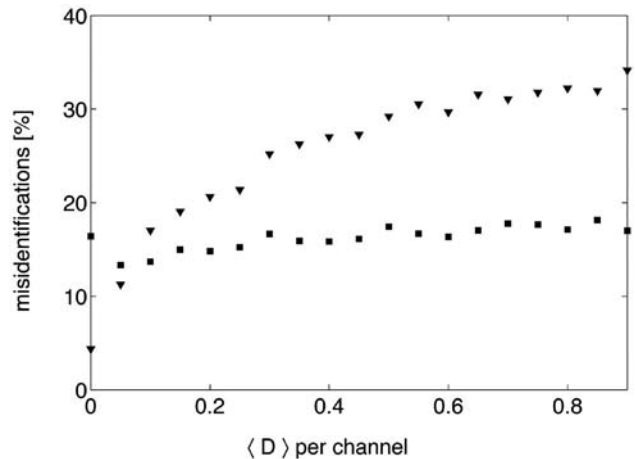


Fig. 12. Same as Fig. 11 but with $(\tau_1, \tau_2) = (2 \text{ ns}, 3 \text{ ns})$.

difference between the two decay times decreases, but the average number of signal counts stays the same, the difference between the two methods is less pronounced but increases again with the number of signal counts. We expect this behavior because for a decreasing difference of the lifetimes and a constant number of counts, the misidentification rate should approach 50% (if the difference vanishes, we cannot do better than guessing).

4. Conclusion

We have reported a new method for performing FLIM measurements by using only one or two single-point detectors. The method is based on HI and reduces detector-induced noise, which may reduce the standard deviation in parameter estimation. Standard deviations are reduced, given that the signal count rate per pixel is low and of the order of the dark-count rate of the detector and that photobleaching is small during the overall measurement time. We calculated the exact likelihood function for Hadamard-transformed fluorescence-decay histograms. Monte Carlo simulations were used to estimate the benefits and limits of the introduced method in several different forms of lifetime imaging, including estimation of lifetimes and signal ratios. Furthermore, we discussed several factors that can reduce the performance of this technique. The factors affecting the performance of the method are high photobleaching and a high dynamic range of the image. Moreover the SNR in HLI will only be higher as compared with that in scanning if a considerable amount of dark noise is present. We have also shown that HLI may produce a superior performance in applications in which fluorophores are identified by means of their prior known lifetimes, as is the case in some biochip applications. In such cases low misidentification rates are possible even for only several tenths of photon counts and low SNRs.

We thank our colleagues from the Laboratory of Biomedical Optics for many helpful discussions. We are especially grateful to Patrice Francois and Jacques Schrenzel (Division of Infectious Diseases,

Geneva University Hospital) for preparing the fluorescence samples used in preliminary experiments. We thank Dietrich Schweitzer and Martin Hammer (Department of Ophthalmology, Friedrich Schiller University, Germany) and Max-Olivier Hongler (Institut de Production et Robotique, Ecole Polytechnique Fédérale de Lausanne) for useful information and discussions. The Swiss National Science Foundation is acknowledged for partly funding this project.

References

1. R. Cubeddu, D. Comelli, C. D'Andrea, P. Taroni, and G. Valentini, "Time-resolved fluorescence imaging in biology and medicine," *J. Phys.* **35**, R61–R76 (2002).
2. S. Bambot, J. R. Lakowicz, and G. Rao, "Potential applications of life-time-based, phase-modulation fluorometry in bioprocess and clinical monitoring," *Trends Biotechnol.* **13**, 106–115 (1995).
3. Bernard Valeur, *Molecular Fluorescence* (Wiley-VCH, 2002).
4. H. Szmazinski and J. R. Lakowicz, "Optical measurements of pH using fluorescence lifetimes and phase-modulation fluorometry," *Anal. Chem.* **65**, 1668–1674 (1993).
5. H. J. Lin, H. Szmazinski, and J. R. Lakowicz, "Lifetime-based pH sensors: indicators for acidic environments," *Anal. Biochem.* **269**, 162–167 (1999).
6. M. E. Lippitsch, J. Pusterhofer, M. J. P. Leiner, and O. S. Wolfbeis, "Fibre-optic oxygen sensor with the fluorescence decay time as the information carrier," *Anal. Chim. Acta* **205**, 1–6 (1988).
7. H. Szmazinski and J. R. Lakowicz, "Sodium green as a potential probe for intracellular sodium imaging based on fluorescence lifetime," *Anal. Biochem.* **250**, 131–138 (1997).
8. T. Q. Ni and L. A. Melton, "Fluorescence lifetime imaging—An approach for fuel equivalence ratio imaging," *Appl. Spectrosc.* **45**, 938–943 (1991).
9. G. Marriott, R. M. Clegg, D. J. Arndtjovin, and T. M. Jovin, "Time resolved imaging microscopy—Phosphorescence and delayed fluorescence imaging," *Biophys. J.* **60**, 1374–1387 (1991).
10. X. F. Wang, T. Uchida, D. M. Coleman, and S. Minami, "A 2-dimensional fluorescence lifetime imaging-system using a gated image intensifier," *Appl. Spectrosc.* **45**, 360–366 (1991).
11. R. Cubeddu, A. Pifferi, P. Taroni, A. Torricelli, G. Valentini, F. Rinaldi, and E. Sorbellini, "Fluorescence lifetime imaging: an application to the detection of skin tumors," *IEEE J. Sel. Top. Quantum Electron.* **5**, 923–929 (1999).
12. P. J. Tadrous, J. Siegel, P. M. W. French, S. Shousha, E. N. Lalani, and G. W. H. Stamp, "Fluorescence lifetime imaging of unstained tissues: early results in human breast cancer," *J. Pathol.* **199**, 309–317 (2003).
13. D. Schweitzer, A. Kolb, M. Hammer, and R. Anders, "Time-correlated measurement of autofluorescence. A method to detect metabolic changes in the fundus," *Ophthalmologie* **99**, 774–779 (2002).
14. G. Valentini, C. d'Andrea, D. Comelli, A. Pifferi, P. Taroni, A. Torricelli, R. Cubeddu, C. Battaglia, C. Consolandi, G. Salani, L. Rossi Bernardi, and G. de Bellis, "Time-resolved DNA-microarray reading by an intensified CCD for ultimate sensitivity," *Opt. Lett.* **25**, 1648–1650 (2000).
15. E. Waddell, Y. Wang, W. Stryjewski, S. McWhorter, A. C. Henry, D. Evans, R. L. McCarley, and S. A. Soper, "High-resolution near-infrared imaging of DNA microarrays with time-resolved acquisition of fluorescence lifetimes," *Anal. Chem.* **72**, 5907–5917 (2000).
16. H. C. Gerritsen, M. A. H. Asselbergs, A. V. Agronskaia, and W. G. J. H. M. Van Sark, "Fluorescence lifetime imaging in scanning microscopes: acquisition speed, photon economy and lifetime resolution," *J. Microsc. (Oxford)* **206**, 218–224 (2002).
17. K. Dowling, M. J. Dayel, M. J. Lever, P. M. W. French, J. D. Hares, and A. K. L. Dymoke Bradshaw, "Fluorescence lifetime imaging with picosecond resolution for biomedical applications," *Opt. Lett.* **23**, 810–812 (1998).
18. N. J. A. Sloane and M. Harwit, "Masks for Hadamard transform optics and weighing designs," *Appl. Opt.* **15**, 107–114 (1976).
19. M. Harwit and N. J. A. Sloane, *Hadamard Transform Optics* (Academic, 1979).
20. P. Fellgett, "Conclusions on multiplex methods," *J. Phys. (Paris)* **28**, 165–171 (1967).
21. R. A. DeVerse, R. M. Hammaker, and W. G. Fateley, "Hadamard transform Raman imagery with a digital micro-mirror array," *Vib. Spectrosc.* **19**, 177–186 (1999).
22. D. Phillips and D. V. O'Connor, *Time-Correlated Single Photon Counting* (Academic, 1984).
23. M. Unser and M. Eden, "Maximum-likelihood estimation of linear signal parameters for Poisson processes," *IEEE Trans. Acoust. Speech Signal Process.* **36**, 942–945 (1988).
24. Z. Bajzer, T. M. Therneau, J. C. Sharp, and F. G. Prendergast, "Maximum-likelihood method for the analysis of time-resolved fluorescence decay curves," *Eur. Biophys. J. Biophys. Lett.* **20**, 247–262 (1991).
25. M. Köllner, A. Fischer, J. ArdenJacob, K. H. Drexhage, R. Müller, S. Seeger, and J. Wolfrum, "Fluorescence pattern recognition for ultrasensitive molecule identification: comparison of experimental data and theoretical approximations," *Phys. Lett.* **250**, 355–360 (1996).
26. A. Papoulis and S. U. Pillai, *Probability, Random Variables and Stochastic Processes* (McGraw-Hill, 2002).
27. Q. S. Hanley, "Masking, photobleaching, and spreading effects in Hadamard transform imaging and spectroscopy systems," *Appl. Spectrosc.* **55**, 318–330 (2001).
28. G. Q. Chen, E. Mei, W. F. Gu, X. B. Zeng, and Y. Zeng, "Instrument for Hadamard-transform 3-dimensional fluorescence microscope image analysis," *Anal. Chim. Acta* **300**, 261–267 (1995).
29. A. G. Tkachenko, H. Xie, D. Coleman, W. Glomm, J. Ryan, M. F. Anderson, S. Franzen, and D. L. Feldheim, "Multifunctional gold nanoparticle-peptide complexes for nuclear targeting," *J. Am. Chem. Soc.* **125**, 4700–4701 (2003).
30. M. van Zandvoort, C. J. de Grauw, H. C. Gerritsen, J. L. V. Broers, M. Egbrink, F. C. S. Ramaekers, and D. W. Slaaf, "Discrimination of DNA and RNA in cells by a vital fluorescent probe: lifetime imaging of syto13 in healthy and apoptotic cells," *Cytometry* **47**, 226–235 (2002).
31. J. Siegel, D. S. Elson, S. E. D. Webb, K. C. B. Lee, A. Vlanclas, G. L. Gambaruto, S. Leveque-Fort, M. J. Lever, P. J. Tadrous, G. W. H. Stamp, A. L. Wallace, A. Sandison, T. F. Watson, F. Alvarez, and P. M. W. French, "Studying biological tissue with fluorescence lifetime imaging: microscopy, endoscopy, and complex decay profiles," *Appl. Opt.* **42**, 2995–3004 (2003).
32. J. Enderlein, "Maximum-likelihood criterion and single-molecule detection," *Appl. Opt.* **34**, 514–526 (1995).
33. J. Enderlein, P. M. Goodwin, A. VanOrden, W. P. Ambrose, R. Erdmann, and R. A. Keller, "A maximum likelihood estimator to distinguish single molecules by their fluorescence decays," *Chem. Phys. Lett.* **270**, 464–470 (1997).

Paper II

High Count Rates with Total Internal Reflection Fluorescence Correlation Spectroscopy

Kai Hassler,* Tiemo Anhut,[†] Rudolf Rigler,* Michael Gösch,* and Theo Lasser*

*Ecole Polytechnique Fédérale de Lausanne (EPFL), Laboratoire d'Optique Biomédicale, CH-1015 Lausanne, Switzerland; and [†]Fraunhofer Institut für Biomedizinische Technik (IBMT), D-66386 St. Ingbert, Germany

ABSTRACT We achieved photon count rates per molecule as high as with commonly used confocal fluorescence correlation spectroscopy instruments using a new total internal reflection fluorescence correlation spectroscopy system based on an epi-illumination configuration.

Received for publication 1 October 2004 and in final form 27 October 2004.

Address reprint requests and inquiries to Michael Gösch, Tel.: 41-21-693-77-37; E-mail: michael.goesch@epfl.ch.

Fluorescence correlation spectroscopy (FCS) (1) requires a particularly high photon count rate per molecule (cpm) and low background when employed to investigate single molecule dynamics. To fulfill this requirement, it is crucial to restrain the observation volume to the close proximity of the system under study. In this respect, the standard confocal detection scheme suffers from drawbacks when used to investigate dynamical processes of biomolecules attached to a surface (for example, ligand-receptor kinetics on cell surfaces or model membranes (2) and conformational changes of biomolecules (3; 4)) since the axial confinement of the confocal volume element is in general large compared to the axial extent of the attached biomolecule. Additionally, excitation light reflected at the surface contributes substantially to the background.

These drawbacks are circumvented in total internal reflection fluorescence correlation spectroscopy (TIR-FCS) (5), where the sample is excited by an evanescent field, generated by total internal reflection of a laser beam. TIR is typically obtained on the interface between a prism serving as a substrate for the system under study and an aqueous solution. The field intensity decays exponentially within the solution with increasing distance from the interface and drops to 1/e of its value after typically < 200 nm. This axial extent of the detection volume is substantially smaller than in the case of confocal FCS, where it is generally on the order of 1.5 μm . Fluorescence is detected from above the prism by means of a microscope and a single photon avalanche diode (SPAD). An aperture or pinhole in the intermediate image plane of the microscope assures lateral confinement of the detection volume element.

TIR-FCS has been applied successfully to investigate a number of different phenomena as, for example, ligand-receptor binding on membranes (6) and surface binding of biomolecules to silica surfaces (7), but little work has been done to further improve sensitivity of TIR-FCS (8). Nonetheless, a high sensitivity, especially high cpm, are crucial for single molecule applications, and increasing them to values

obtained in confocal FCS would considerably augment the number of possible applications (9).

We have developed a TIR-FCS system and obtained cpm values comparable to those achieved with a common confocal FCS system. In contrast to the above described prism-based TIR-FCS setup, we adapted an objective-based total internal reflection fluorescence (TIRF) system (10), which makes use of an epi-illumination configuration to excite and detect fluorescence (see Fig. 1). Here, the beam of an argon ion laser (model 2214-25ML, Cyonics, Sunnyvale, CA) is focused onto the back focal plane (bfp) of an oil-immersion objective (α -Plan-Fluar, 1.45 NA, 100 \times , Carl Zeiss Jena GmbH, Jena, Germany) residing in an inverted microscope (IX70, Olympus, Tokyo, Japan). The location of the focal spot within the bfp determines the inclination angle under which the collimated beam impinges on the upper surface of a microscope slide. By tilting the glass plate, the location of the spot is adjusted to satisfy the condition for total internal reflection. The fluorescence emission is collected by the same objective, focused to a multi-mode fiber with a 50 μm diameter core, serving as a pinhole and finally detected by a SPAD (SPCM-AQR-13-FC, PerkinElmer, Wellesley, MA).

With respect to the classical prism-based TIR-FCS scheme, this approach has several advantages. Most important, as the sample of interest is situated directly on the microscope slide, all light that is emitted in the lower half space and not reflected is collected by the high NA objective. Therefore, we expect a significant higher value of counts per molecule compared to a prism-based setup. Further, once the setup is properly aligned, it is very stable and samples can be exchanged easily. Compared to confocal FCS, a smaller portion of the reflected laser light reaches the detector. This is because the back-reflected laser beam is collimated and therefore not focused onto the pinhole.

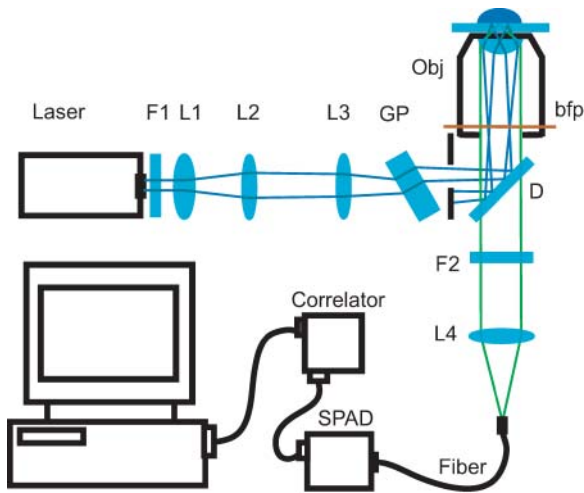


FIGURE 1 Schematic of setup for objective type TIR-FCS. The laser beam is enlarged and collimated through the telescope formed by lenses L1 and L2. Lens L3 focuses the beam at the bfp of the objective. GP, glass plate; F1, F2, filter; D, dichroic mirror; Obj, microscope objective; L1–L4, lenses.

To show the described advantages, diffusion of carboxy fluorescein in aqueous solution was measured within the evanescent field. To fit the autocorrelation data, a mathematical model based on the theoretical description by Starr and Thompson (11) was adapted (Eq. 1). An approximation disregarding binding to the surface could be used since fluorescein is negatively charged and therefore almost not subject to unspecific binding to the glass surface. Whereas in Starr and Thompson the influence of transversal diffusion has been neglected, it is necessary to take this into account in our case, since the observation volume was laterally restricted by introducing a pinhole. We used a Gauss function to model the lateral intensity distribution and an exponential decay in axial direction. Furthermore, our model contains a term accounting for triplet state kinetics to meet the experimental conditions and to fit the data more accurately. With these modifications, the correlation function reads

$$G(\tau) = 1 + \frac{1}{2N} \left(1 + \frac{p}{1-p} e^{-\frac{\tau}{\tau_t}} \right) \left(1 + \frac{\tau}{\tau_{xy}} \right)^{-1} \times \left[\left(1 - \frac{\tau}{2\tau_z} \right) w \left(i \sqrt{\frac{\tau}{4\tau_z}} \right) + \sqrt{\frac{\tau}{\pi\tau_z}} \right]. \quad (1)$$

N is the number of molecules in an effective volume defined by $V_{\text{eff}} \equiv \pi \omega_{xy}^2 d$, where ω_{xy} is the lateral extend of the Gaussian intensity distribution and d is the distance from the surface where the intensity decreases by a factor $1/e$. The diffusion times are $\tau_z \equiv d^2/(4D)$ and $\tau_{xy} \equiv \omega_{xy}^2/(4D)$ for the axial diffusion and diffusion parallel to the surface, respectively. D denotes the diffusion constant. The triplet state decay time is given by τ_t , and p is the average fraction of molecules in the effective volume that are in the triplet state.

w is the complex generalization of the error function, $w(x) \equiv \exp(-x^2) \text{erfc}(-ix)$. As in confocal FCS without regarding triplet state kinetics, the amplitude of the correlation function (after the subtraction of 1) is inversely proportional to the number of molecules in the detection volume element V_{eff} :

$$G(\tau) - 1 = \frac{1}{2N}.$$

Measurements were performed on droplets containing carboxy fluorescein in TRIS buffer (pH 8) deposited on microscope coverslips. cpm values as high as 34 kHz could be achieved. Fig. 2 shows a typical example for an auto-correlation curve obtained with our setup. The overall background was ~ 6.1 kHz for TIR-FCS. The axial diffusion time was on the order of $15 \mu\text{s}$, for an evanescent field depth of ~ 200 nm. This implies a diffusion constant of $D = 7 \times 10^{-6} \text{ cm}^2 \text{ s}^{-1}$ for fluorescein, which is in agreement with values measured in previous work (12).

Similar values could be obtained with our TIR-FCS setup when working in confocal FCS mode. This is possible by

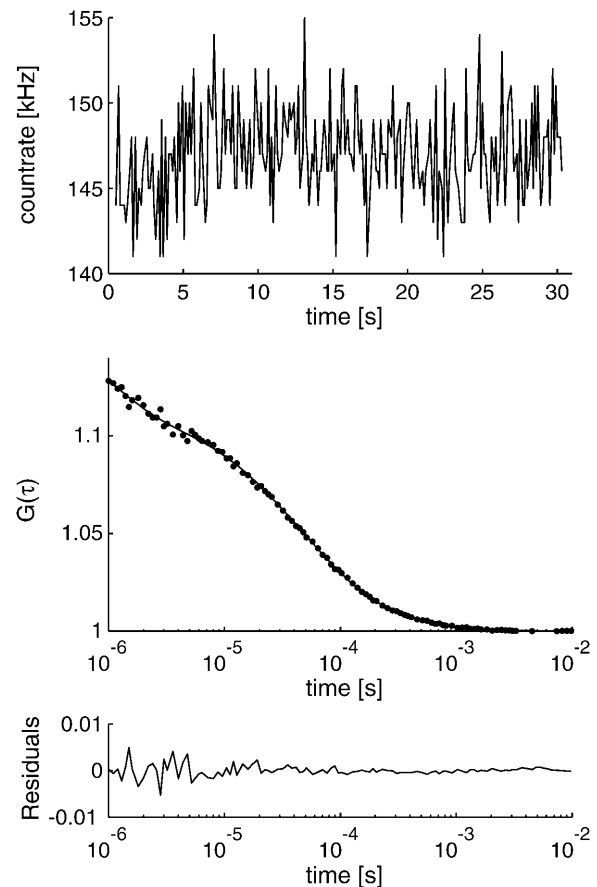


FIGURE 2 Time trace and correlation curve obtained with the proposed setup, curve fit according to Eq. 1. cpm = 33 kHz, $N = 4.4$, $\tau_z = 12.9 \mu\text{s}$, $p = 29\%$, $\tau_t = 1.1 \mu\text{s}$, and $d/\omega_{xy} = 0.4$ (fixed parameter).

removing the glass plate, the focusing lens L3, and using an appropriate water-immersion objective. In this configuration, we obtained for measurements on the surface comparable cpm values (maximum 38 kHz). The background, however, was >2 times higher (14 kHz) than obtained for TIR-FCS.

In conclusion, we presented an effective, stable, and practically simple TIR-FCS system, which allows measurements to be performed with surprisingly high cpm values. This work, thereby, opens the way for TIR-FCS to be used in applications where a high signal/noise ratio is crucial.

ACKNOWLEDGMENTS

We thank Carl Zeiss Jena GmbH for providing us with the α -Plan-Fluar objective.

REFERENCES and FOOTNOTES

- (1) Rigler, R., and E. L. Elson. 2001. *Fluorescence Correlation Spectroscopy: Theory and Applications*. Berlin, Springer.
- (2) Auer, M., K. J. Moore, F. J. Meyer-Almes, R. Guenther, A. J. Pope, and K. A. Stoekli. 1998. Fluorescence correlation spectroscopy: lead discovery by miniaturized HTS. *Drug Discov. Today*. 3:457–465.
- (3) Jia, Y. W., A. Sytnik, L. Q. Li, S. Vladimirov, B. S. Cooperman, and R. M. Hochstrasser. 1997. Nonexponential kinetics of a single tRNA(Phe) molecule under physiological conditions. *Proc. Natl. Acad. Sci. USA*. 94:7932–7936.
- (4) Edman, L., U. Mets, and R. Rigler. 1996. Conformational transitions monitored for single molecules in solution. *Proc. Natl. Acad. Sci. USA*. 93:6710–6715.
- (5) Thompson, N. L., T. P. Burghardt, and D. Axelrod. 1981. Measuring surface dynamics of biomolecules by total internal-reflection fluorescence with photobleaching recovery or correlation spectroscopy. *Biophys. J.* 33:435–454.
- (6) Lieto, A. M., R. C. Cush, and N. L. Thompson. 2003. Ligand-receptor kinetics measured by total internal reflection with fluorescence correlation spectroscopy. *Biophys. J.* 85:3294–3302.
- (7) Hansen, R. L., and J. M. Harris. 1998. Measuring reversible adsorption kinetics of small molecules at solid/liquid interfaces by total internal reflection fluorescence correlation spectroscopy. *Anal. Chem.* 70:4247–4256.
- (8) Ruckstuhl, T., and S. Seeger. 2004. Attoliter detection volumes by confocal total-internal-reflection fluorescence microscopy. *Opt. Lett.* 29:569–571.
- (9) Schwille, P. 2003. TIR-FCS: staying on the surface can sometimes be better. *Biophys. J.* 85:2783–2784.
- (10) Axelrod, D. 2001. Total internal reflection fluorescence microscopy in cell biology. *Traffic*. 2:764–774.
- (11) Starr, T. E., and N. L. Thompson. 2001. Total internal reflection with fluorescence correlation spectroscopy: combined combined surface reaction and solution diffusion. *Biophys. J.* 80:1575–1584.
- (12) Culbertson, C. T., S. C. Jacobson, and J. M. Ramsey. 2002. Diffusion coefficient measurements in microfluidic devices. *Talanta*. 56:365–373.

Paper III

Total internal reflection fluorescence correlation spectroscopy (TIR-FCS) with low background and high count-rate per molecule

Kai Hassler¹, Marcel Leutenegger¹, Per Rigler², Ramachandra Rao¹,
Rudolf Rigler¹,
Michael Gösch¹ and Theo Lasser¹

¹*Ecole Polytechnique Fédérale de Lausanne (EPFL), Laboratoire d'Optique Biomédicale,
1015 Lausanne, Switzerland*
theo.lasser@epfl.ch

²*Universität Basel, Physikalische Chemie, 4056 Basel, Switzerland*

Abstract: We designed a fluorescence correlation spectroscopy (FCS) system for measurements on surfaces. The system consists of an objective-type total internal reflection fluorescence (TIRF) microscopy setup, adapted to measure FCS. Here, the fluorescence exciting evanescent wave is generated by epi-illumination through the periphery of a high NA oil-immersion objective. The main advantages with respect to conventional FCS systems are an improvement in terms of counts per molecule (cpm) and a high signal to background ratio. This is demonstrated by investigating diffusion as well as binding and release of single molecules on a glass surface. Furthermore, the size and shape of the molecule detection efficiency (MDE) function was calculated, using a wave-vectorial approach and taking into account the influence of the dielectric interface on the emission properties of fluorophores.

© 2005 Optical Society of America

OCIS codes: (300.2530) Fluorescence, laser induced; (170.6280) Spectroscopy, fluorescence and luminescence; (240.6490) Spectroscopy, surface

References and links

1. D. Magde, W. W. Webb, and E. Elson, "Thermodynamic Fluctuations in a Reacting System - Measurement by Fluorescence Correlation Spectroscopy," *Phys. Rev. Lett.* **29**, 705–& (1972).
2. R. Rigler and E. L. Elson, *Fluorescence Correlation Spectroscopy: Theory and Applications* (Springer, Berlin, 2001).
3. O. Krichevsky and G. Bonnet, "Fluorescence correlation spectroscopy: the technique and its applications," *Rep. Progr. Phys.* **65**, 251–297 (2002).
4. R. Rigler, U. Mets, J. Widengren, and P. Kask, "Fluorescence Correlation Spectroscopy with High Count Rate and Low-Background - Analysis of Translational Diffusion," *Eur. Biophys. J. Biophys. Lett.* **22**, 169–175 (1993).
5. R. Brock and T. M. Jovin, "Fluorescence correlation microscopy (FCM) - Fluorescence correlation spectroscopy (FCS) taken into the cell," *Cell. Mol. Biol.* **44**, 847–856 (1998).
6. M. Auer, K. J. Moore, F. J. Meyer-Almes, R. Guenther, A. J. Pope, and K. A. Stoekli, "Fluorescence correlation spectroscopy: lead discovery by miniaturized HTS," *Drug Discov. Today* **3**, 457–465 (1998).
7. A. M. Lieto, R. C. Cush, and N. L. Thompson, "Ligand-receptor kinetics measured by total internal reflection with fluorescence correlation spectroscopy," *Biophys. J.* **85**, 3294–3302 (2003).
8. U. Kettling, A. Koltermann, P. Schwille, and M. Eigen, "Real-time enzyme kinetics monitored by dual-color fluorescence cross-correlation spectroscopy," *Proc. Natl. Acad. Sci. USA* **95**, 1416–1420 (1998).

9. L. Edman, Z. Foldes-Papp, S. Wennmalm, and R. Rigler, "The fluctuating enzyme: a single molecule approach," *Chem. Phys.* **247**, 11–22 (1999).
10. N. L. Thompson, T. P. Burghardt, and D. Axelrod, "Measuring Surface Dynamics of Biomolecules by Total Internal-Reflection Fluorescence with Photobleaching Recovery or Correlation Spectroscopy," *Biophys. J.* **33**, 435–454 (1981).
11. K. Hassler, T. Anhut, R. Rigler, M. Gösch, and T. Lasser, "High count rates with total internal reflection fluorescence correlation spectroscopy," *Biophys. J.* **88**, L1–L3 (2005).
12. D. Axelrod, E. H. Hellen, and R. M. Fulbright, "Total Internal Reflection Fluorescence," in *Topics in Fluorescence Spectroscopy: Biochemical Applications*, J. R. Lakowicz, ed., vol. 3 (Plenum Press, 1992).
13. D. Axelrod, "Total internal reflection fluorescence microscopy in cell biology," *Traffic* **2**, 764–774 (2001).
14. D. Toomre and D. J. Manstein, "Lighting up the cell surface with evanescent wave microscopy," *Tr. Cell Biol.* **11**, 298–303 (2001).
15. R. L. Hansen, J. M. Harris, "Total Internal Reflection Fluorescence Correlation Spectroscopy for Counting Molecules at Solid/Liquid Interfaces," *Anal. Chem.* **70**, 2565–2575 (1998).
16. W. Lukosz, "Light-Emission by Magnetic and Electric Dipoles Close to a Plane Dielectric Interface .3. Radiation-Patterns of Dipoles with Arbitrary Orientation," *J. Opt. Soc. Am.* **69**, 1495–1503 (1979).
17. J. Enderlein, "Fluorescence detection of single molecules near a solution/glass interface - an electrodynamic analysis," *Chem. Phys. Lett.* **308**, 263–266 (1999).
18. N. L. Thompson, "Fluorescence Correlation Spectroscopy," in *Topics in Fluorescence Spectroscopy*, J. R. Lakowicz, ed., vol. 1 (Plenum Press, New York, 1991).
19. B. Richards and E. Wolf, "Electromagnetic Diffraction in Optical Systems .2. Structure of the Image Field in an Aplanatic System," *Proc. Roy. Soc. A* **253**, 358–379 (1959).
20. J. Mertz, "Radiative absorption, fluorescence, and scattering of a classical dipole near a lossless interface: a unified description," *J. Opt. Soc. Am. B-Opt. Phys.* **17**, 1906–1913 (2000).
21. S. Weiss, "Fluorescence Spectroscopy of Single Biomolecules," *Science* **283**, 1676–1683 (1999).
22. K. Hassler, M. Leutenegger, M. Gösch, T. Lasser, Laboratoire d'Optique Biomédicale, Ecole Polytechnique Fédérale de Lausanne (EPFL), 1015 Lausanne, Switzerland are preparing a manuscript to be called "Mathematical Models for Total Internal Reflection Fluorescence Correlation Spectroscopy".
23. C. T. Culbertson, S. C. Jacobson, and J. M. Ramsey, "Diffusion coefficient measurements in microfluidic devices," *Talanta* **56**, 365–373 (2002).

1. Introduction

An increasing number of research fields in biology and medicine requires spectroscopic techniques with single molecule sensitivity in order to understand biochemical or microbiological processes. One of the technological milestones for spectroscopy was therefore the development of the confocal principle, which subsequently resulted in a very high signal to noise ratio in many applications. The implementation of the confocal principle, known from microscopy, in fluorescence correlation spectroscopy (FCS) [1, 2, 3] in the early 90's, was a technical innovation that dramatically enhanced the sensitivity of FCS [4]. From this moment on, FCS was used in an ever increasing number of applications to investigate dynamic and kinetic properties of molecular systems including measurements of diffusion inside cells [5], investigations of receptor - ligand binding kinetics [6, 7] and enzyme binding and reaction kinetics [8, 9]. The latter applications generally require the molecular system under investigation to be attached to a surface. In this case, the use of total internal reflection FCS (TIR-FCS) [10] can be advantageous over confocal FCS. In contrast to confocal FCS where fluorophores are excited inside the waist of a laser beam, TIR-FCS uses an evanescent wave to excite molecules. This leads to a reduced axial extent of the observation volume and hence to a decreased background from Raman scattered light and from unwanted fluorescence of molecules in solution. However, both techniques, when used for measurements on surfaces, have disadvantages. For instance, confocal FCS suffers from a large axial extent of the excitation- and hence observation volume, while for classical TIR-FCS, the light collection efficiency is comparably low. To circumvent these inadequacies we propose a new technique that combines several aspects of TIR-FCS and confocal FCS [11]. Based on an objective-type TIRF setup [12, 13, 14], the proposed system uses epi-illumination through the periphery of a high NA oil-immersion objective to generate an evanescent wave on the surface of a microscope slide. The fluorescence signal is collected

by the same objective, which leads to an excellent light collection efficiency while retaining the advantage of a reduced detection volume. In the present paper, we demonstrate the high performance of 'objective-type TIR-FCS' by investigating diffusion and binding of free dye molecules on surfaces, respectively. Our results show that the proposed technique has superior performance compared to classical FCS methods with respect to the signal to background ratio and counts per molecule (cpm). The parameter cpm is a frequently used figure of merit in FCS, which denotes the detection rate of photons, emitted by a single fluorophore inside the observation volume. Furthermore, the molecule detection efficiency (MDE) function and the size of the observation volume was calculated using high-angle vectorial diffraction integrals. The calculations incorporate the influence of the dielectric interface on the emission properties of fluorophores. Parameters derived from experimental data, in particular the structure parameter and diffusion times, agree with the calculated MDEs.

2. Instrumentation

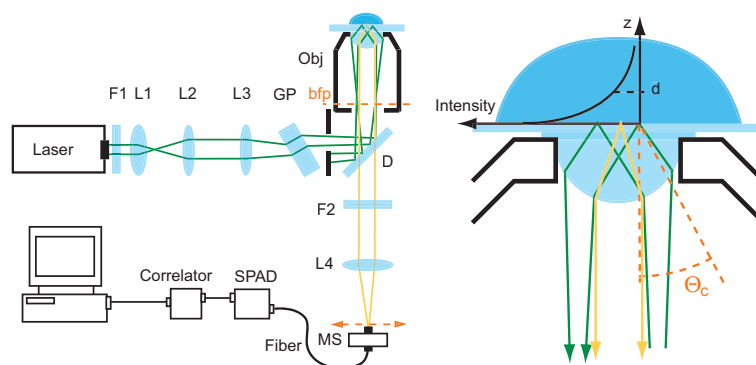


Fig. 1. Schematic representation of the 'objective-type TIR-FCS' setup (left). L1 - L4: lenses; F1, F2: fluorescence filters; GP: glass plate; D: dichroic mirror; Obj: microscope objective; bfp: back focal plane of the objective; MS: motorized scanning stage. An enlargement of the ray-path inside the microscope objective (right). d : evanescent wave depth; Θ_c : critical angle.

The setup (Fig. 1) is essentially an objective-type ('prismless') total internal reflection fluorescence (TIRF) setup adapted to measure FCS. Here, the beam of an argon ion laser (model 2214-25ML, Cyonics, Sunnyvale, CA) is enlarged by means of a telescope formed by lenses L1 and L2. Lens L3 focuses the beam onto the back focal plane (BFP) of an oil-immersion objective (α -Plan-Fluar, 1.45 NA, 100 \times , Carl Zeiss Jena GmbH, Jena, Germany) in order to get a collimated beam emerging from the objective. A pivotable glass-plate GP enables lateral shifting of the laser beam with respect to the optical axis. By shifting the beam, the angle of incidence at the glass-sample interface can be adjusted to exceed the critical angle Θ_c , thereby introducing total internal reflection. In this way, an evanescent wave with an intensity distribution that is Gaussian in the xy plane (parallel to the interface) and exponential in the z direction (along the optical axis) is generated at the glass-sample interface. The intersection of the beam with the interface is elliptical, with a lateral dimension (full width at half maximum of the intensity distribution in the plane of incidence) of roughly 15 μm . Fluorescence light is collected by the same objective and focused onto the end of a fiber, which is connected to a single photon avalanche diode (SPAD) (SPCM-AQR-13-FDC, PerkinElmer, Wellesley, MA). The core of the fiber acts as a pinhole assuring the lateral confinement of the observation volume. In our measurements we used a fiber with a core diameter of 50 μm , unless otherwise stated,

which was a convenient choice for the experimental investigations. The signal of the SPAD is processed by a hardware correlator or a single photon counting module (SPCM, SPC-630, Becker & Hickl GmbH, Berlin, Germany) to record the intensity versus time trace with high time resolution.

The illuminated region at the glass-water interface is several times larger than the observation volume, whose lateral extent is delimited by a pinhole in the microscope's image plane. The actual size of the illuminated region is adjustable by changing the magnification of the telescope used to enlarge the beam. Because of the large illuminated region, TIRF imaging using a camera and spectroscopic measurements can be performed at the same time. For spectroscopic measurements, locating a position of interest in the sample, e.g. a single receptor attached to the glass surface, may be achieved by scanning the fiber end in the image plane. There is no need to move the sample in this case, which makes the system very stable under experimental conditions. However, for some applications, where the residence time of fluorophores on the surface is large, illuminating a whole area may be disadvantageous due to the risk of photo-bleaching.

The advantages of the objective-type configuration with respect to prism-based configurations are, in particular, a higher light collection efficiency and easier handling of the system. In conventional (prism-based) TIR-FCS [10, 15], the evanescent wave is generated by means of a prism, placed on top of an objective that resides, in general, in an inverted microscope. A microscope slide is interfaced to the lower surface of the prism using immersion oil. The biological system (e.g. a membrane containing receptors) is attached to the lower surface of this glass slide, where fluorescence is excited by the evanescent wave. The sample, containing the biological system and some type of aqueous solution is sandwiched between the glass slide and another microscope-, or coverslide. An objective (typically a water immersion objective), placed below the coverslide is used to collect fluorescence light. The objective therefore focuses into an aqueous solution.

For objective-type TIR-FCS, the coverslide carrying the biological system is situated directly upon the objective and focusing into an aqueous solution is avoided. Only in such a case does the use of high NA oil immersion objectives become senseful because these objectives are designed to collect light in a high refractive index environment. They perform poorly, due to aberrations, if the focal plane is not right at the surface of the coverglass [3]. Using an oil immersion objective with NA 1.45 in the proposed configuration guarantees that almost all of the light from fluorescent particles at the focus position, emitted into the lower half-space falls into the cone of light accepted by the objective. The portion of light that is accepted even exceeds 50% because the light emission for dipoles near a dielectric interface is anisotropic, favoring emission into the medium with the higher refractive index [16, 17]. A further advantage of the present system is easier sample access. In particular, there is no hindrance by a prism as is the case in prism-based TIRF or TIR-FCS instruments [14].

3. Observation volume

In order to determine the shape and estimate the size of the detection volume, we calculated the normalized molecule detection efficiency (MDE) function [18], based on a wave-vectorial approach [19]. The MDE expresses the relative intensity seen by the detector as a function of the position of a point-emitter in the sample space; it is therefore the correct mathematical representation of the detection volume.

Figure 2 shows the normalized MDEs for a confocal FCS system (left) and for our TIR-FCS system (right). The MDE is calculated by multiplying the intensity distribution, $I(\mathbf{r})$, by the collection efficiency function (CEF), the CEF being proportional to the probability for a photon to be detected as a function of the position of the emitter:

$$\text{MDE}(\mathbf{r}) = c \text{CEF}(\mathbf{r})I(\mathbf{r}). \quad (1)$$

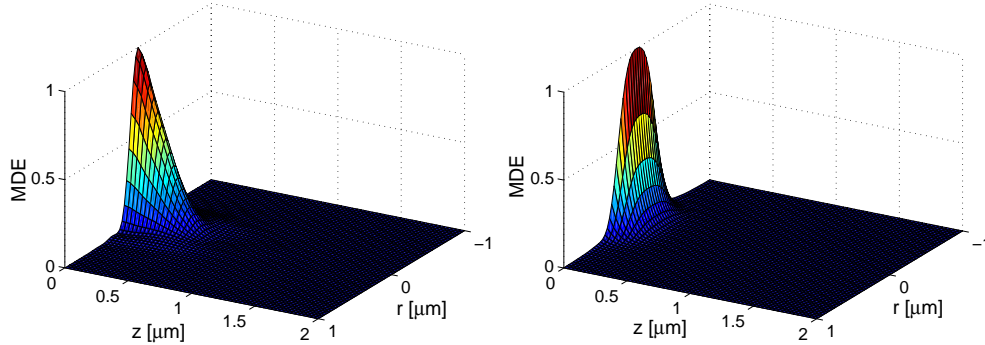


Fig. 2. The normalized MDEs for confocal FCS (left) and TIR-FCS (right). The confocal FCS case was calculated for a 1.15 NA, 40 × water-immersion objective. For the TIR-FCS case a 1.45 NA, 100 × oil-immersion objective was considered. A diameter of the pinhole (core of the fiber) of 50 μm was assumed in both cases. The excitation wavelength was 488 nm and the fluorescence emission wavelength was 542 nm.

The constant c is a normalization coefficient introduced to make $MDE(0) = 1$. The fiber core diameter in both cases was 50 μm and the excitation wavelength was 488 nm, corresponding to the blue line of the argon laser. The fluorophore under consideration was fluorescein. We assumed an emission wavelength of 542 nm, which is the average of the emission spectrum of fluorescein multiplied by the transmission function of the emission filter. In the confocal FCS case, we calculated the MDE for a 1.15 NA, 40× water immersion objective, which is standard. For confocal FCS, the intensity distribution was approximated by the point-spread function (PSF) of the system. The intensity distribution for TIR-FCS was assumed to be constant in the xy plane on the length scale of the typical diameter of the observation volume. It was further assumed to decay exponentially in the z direction with a penetration depth, d , of the intensity distribution given by:

$$d = \frac{\lambda}{4\pi} (n_2^2 \sin^2(\theta) - n_1^2)^{-1/2}. \quad (2)$$

This was calculated for a maximal lateral displacement of the excitation beam, implying a minimal angle of incidence $\theta = 71^\circ$. Here, n_1 and n_2 are the refractive indices of water and of the glass slide, respectively. The angle of incidence at the glass-water interface, θ , was measured by out-coupling the beam with the aid of a prism.

In the proximity of a dielectric interface the emission of a dipole with random orientation becomes highly anisotropic. This results in an apparent increase of the fluorophores brightness with decreasing distance to the interface [16, 17]. To take this effect into account we introduce the function $P(z)$, the fraction of power emitted by a single dipole at a distance z from the interface into the cone of light accepted by the objective. This is calculated for a dipole with random orientation situated at the optical axis according to [20]. The CEF may then be approximated by

$$CEF(\mathbf{r}) = P(z) \int_S \text{circ}(\mathbf{q}'/a) \text{PSF}(\mathbf{q} - \mathbf{q}', z) d\mathbf{q}'. \quad (3)$$

This is a convolution of the systems point spread function, $\text{PSF}(\mathbf{r})$, calculated according to [19], with the transmission function of the pinhole represented by a disk function, $\text{circ}(\mathbf{q}/a)$, and multiplied by $P(z)$. The convolution is carried out in the focal plane in object space ($z = 0$). The symbol \mathbf{q} denotes a vector in the focal plane and a is the pinhole size divided by the

magnification of the microscope. Results in Fig. 2 are consistent with experimental results, which we discuss later in section 5.

Given the MDE, we numerically calculated the W_1 volume and the effective volume, $V_{eff} \equiv W_1^2/W_2$, using [18]

$$W_n \equiv \int_V \text{MDE}^n(\mathbf{r}) d\mathbf{r}, \quad (4)$$

where V is the half-space containing the sample. The quantity W_1 is the size of the geometrical volume that would produce the given count-rate if the detection efficiency were equal to the maximum of the MDE and constant inside the volume. The numerical calculations give $W_1 = 17$ al (17 attoliter), $V_{eff} = 57$ al for TIR-FCS and $W_1 = 26$ al, $V_{eff} = 134$ al for confocal FCS.

The numerically calculated MDE for TIR-FCS is close to the analytical approximation given by

$$\text{MDE}_a(x, y, z) = \exp\left(-2\frac{(x^2 + y^2)}{\omega_{xy}^2}\right) \exp\left(-\frac{z}{h}\right). \quad (5)$$

The calculations of the autocorrelation function in section 5 are based on this approximation. Here, h is the axial displacement at which the normalized MDE decreases to $1/e$. This is smaller than the evanescent field depth, since the MDE, being the product of two in z monotonically decreasing functions (I and CEF), decreases faster with z than the intensity I .

4. Single molecule binding

Several groups were able to show the single fluorophore detection capabilities of objective-type TIRF (see [21] and references therein). We would expect that the proposed TIR-FCS setup features similar sensitivity since it differs from an objective-type TIRF setup essentially in the way the detected signal is processed and in the fact that for FCS only a single-point detector is used. Using our TIR-FCS setup, we performed measurements on single rhodamine 6G molecules undergoing adsorption and desorption on glass coverslips. Thereby we were able to examine the performance of our system; in particular, from high resolution intensity time traces we could estimate a lower bound for the maximal cpm that can be achieved in objective-type TIR-FCS experiments on binding kinetics. Dye molecules, present at a low concentration, diffused through the sample and eventually adsorbed at some location at the surface. For dyes entering the observation volume, and especially for binding events inside the observation volume, intensity peaks or bursts were observed. In general, the height of a burst depends on the lateral location of the bound dye within the observation volume or, for a diffusing dye, on its trajectory. It further depends on the dyes residence time inside the observation volume in the case that this is shorter than the binning time. Therefore, the cpm inferred from single molecule bursts are in general lower than the maximal cpm. For example, the maximal cpm would be obtained in experiments investigating binding kinetics of a single receptor, perfect alignment presumed; in other words, if the receptor is situated at the position where the MDE is maximal.

For these measurements, we have chosen experimental conditions described in the following. We used standard microscope coverslips previously cleaned by sonication in 2% Helmanex. The applied laser power incident on the microscope slide was approximately 10 - 15 mW. We used a dye solution containing 1 nM rhodamine 6G in buffer (potassium phosphate, pH 7.0), a concentration, low enough to assure that only single molecule events are observed. Due to adsorption, this concentration of free dye drops to smaller values immediately after applying the solution to the coverslide. Using a conventional confocal FCS system (Confocor I, Zeiss Jena GmbH), we checked the sample to exclude further that bursts are due to aggregated molecules. No aggregation could be inferred from the FCS data.

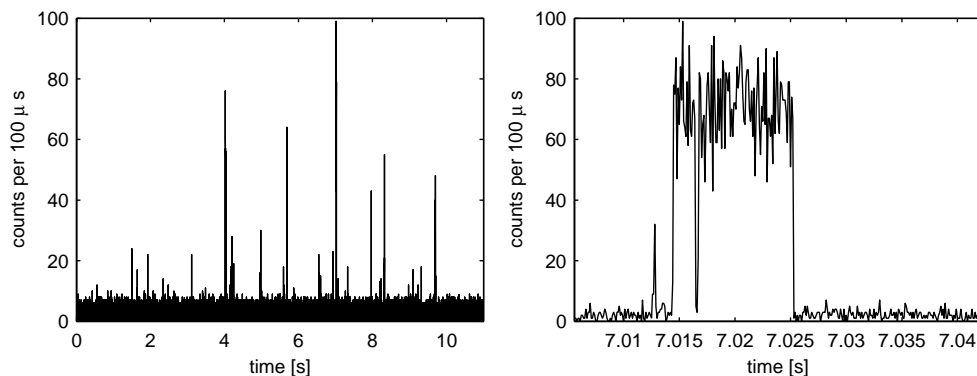


Fig. 3. Typical time trace for single rhodamine 6G molecules binding to a microscope slide (left). The right picture shows an enlargement of the two highest bursts. The binning time is $100\mu\text{s}$.

Figure 3 shows a typical time trace (left) and an enlargement of the highest photon bursts (right). The threshold for identifying a burst was set to 10 counts per $100\mu\text{s}$ (given a background of 2 counts per $100\mu\text{s}$), in order to keep the probability for false positives (bursts due to variations of the background) low. Given this threshold, one can expect about one false positive in a time window of ten seconds. Intensity peaks, lasting on average for about $400\mu\text{s}$, occurred with a frequency of about 7 per second. The average number of overlaps of two or more bursts in a time interval of 10 s was calculated to be approximately one, for about 70 bursts in total. The probability to observe two molecules residing at the same time in the observation volume was therefore small. For broader bursts the binning time ($100\mu\text{s}$) was small compared to the lasting of the bursts (sometimes several milliseconds). Bursts due to two (or more) molecules could in this case be easily distinguished from single molecule events by the necessary existence of steps or spikes. This is because a timely overlap of two binding events will never be exact; two molecules will not adsorb to, and desorb from the surface at exactly the same time, presumed that there is no aggregation (see above). In the example shown, inspection of the enlargement confirms the assumption that the observed event was caused either by a single molecule, or two, but successively binding molecules. In particular no spikes or steps are observed during the photon bursts lasting for about 10 ms. In general, burst heights frequently exceeded 70 counts, which implies cpm of more than 700 kHz. The background was approximately 20 kHz, which implies a signal to background ratio of 35 for the highest burst shown in Fig. 3. These values are further supported by FCS measurements of diffusing dyes as is shown in the following section.

5. FCS on diffusing molecules

We performed TIR-FCS measurements on rhodamine 6G molecules freely diffusing near a coverglass surface. To prevent unspecific binding, the microscope slides were treated with oxygen plasma before use. This renders the surface of the slides highly hydrophilic and lowers the probability to observe binding events. As a result, the correlation time becomes orders of magnitude smaller compared to measurements on slides not specially prepared. Furthermore, after cleaning with oxygen plasma no bursts are observed in the time traces, given a binning time of 100 ms and a fluorophore concentration, C , of 1 nM.

Figure 4 shows an autocorrelation curve and the corresponding time trace obtained for a solution of 100 nM rhodamine 6G in water. To fit the data, we used the model presented in [11]

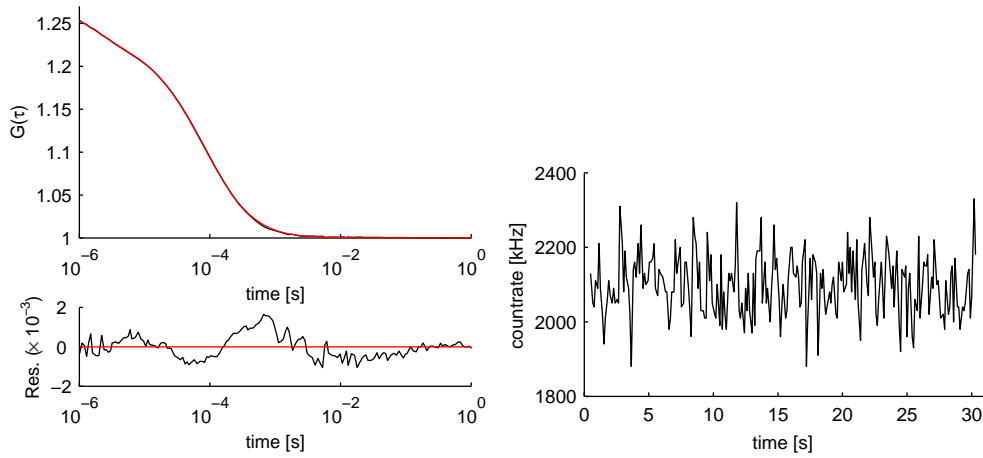


Fig. 4. Autocorrelation for diffusing rhodamine 6G molecules (upper left) and time trace (right). The overall measurement time was 30 s. Fitting the data with the model represented by equation 6 yields the following parameters: $N = 1.2$, $\tau_z = 21.1 \mu\text{s}$, $\omega = 0.38$, $p = 15.4\%$, $\tau_t = 1.6 \mu\text{s}$ and $\text{cpm} = 1.77 \text{ MHz}$. The red curve represents the fit to the autocorrelation data.

and further discussed in [22]:

$$G(\tau) = 1 + \frac{\gamma}{N} \left[1 + \frac{p}{1-p} \exp\left(-\frac{\tau}{\tau_t}\right) \right] \left(1 + \frac{\tau}{\omega^2 \tau_z} \right)^{-1} \times \left[\left(1 - \frac{\tau}{2\tau_z} \right) w \left(i\sqrt{\frac{\tau}{4\tau_z}} \right) + \sqrt{\frac{\tau}{\pi\tau_z}} \right]. \quad (6)$$

The diffusion times are $\tau_z = h^2/(4D)$ and $\tau_{xy} = \omega_{xy}^2/(4D) = \omega^2 \tau_z$ for the axial diffusion and diffusion parallel to the surface, D is the diffusion coefficient, and $\omega = \omega_{xy}/h$. The parameters h and ω_{xy} describe the geometry of the observation volume (equation 5). The parameter p denotes the percentage of molecules in the triplet state and τ_t denotes the triplet state decay time. The function w is defined by $w \equiv \exp(-x^2)\text{erfc}(-ix)$, and γ is a correction factor defined as $\gamma \equiv W_2/W_1$ [18]. This factor describes the deviation of the effective volume, $V_{eff} \propto 1/(CG(0))$, from W_1 . From equations 4 and 5 it follows that γ equals 1/4. However, in the subsequent calculations we used the value $\gamma = 1/3.4$, which was obtained from the numerical calculations.

To estimate the cpm from diffusion measurements, we used $\text{cpm} = r/N$ where r stands for the total average count-rate. N is the number of molecules in the volume W_1 , which implies the cpm is the maximal value for a molecule that stays at the position where the MDE is maximal. This deviates from the definition in [11], where cpm describes an averaged value. The value for cpm in the example shown in Fig. 4 reaches almost 1.8 MHz. This is higher than the value obtained from the more direct investigation of the time traces (Fig. 3). The discrepancy may be due to a different alignment, especially of the focus position with respect to the sample and/or a different incident angle of the laser beam. Indeed, the background in these diffusion measurements was higher too; we estimated it to be approximately 45 kHz for FCS measurements in distilled water. This implies a signal to background ratio of about 39, which is close to the value obtained from direct measurements, which is 35.

From inspection of the residuals (Fig. 5, lower left), we conclude that the model still deviates from reality. This may be due to the fact, that there is some interaction of the dye with the surface even after treating the slides with oxygen plasma. In the present model, interaction of

dyes with the surface is not taken into account. Nevertheless, fitting of the data with the model represented by equation 6 gives reasonable parameter estimates.

In order to experimentally verify the model given by equation 6, TIR-FCS measurements for three different core diameters (37.5 μm , 50 μm and 100 μm) were performed on diffusing fluorescein. A solution of 50 nM fluorescein in buffer (TRIS, pH 8) was used for these experiments. The results for three typical measurements over 100 s measurement time are shown in Table 1.

Table 1. Parameter estimates for measurements with different pinhole diameters. pd : diameter of the pinhole. D : diffusion coefficient. ω_t : theoretically obtained structure parameter. For other symbols refer to the discussion of equation 6. The parameter τ was fixed to 1 μs .

pd [μm]	N	τ_z [μs]	τ_{xy} [μs]	ω_t	ω	p [%]	τ_t [μs]	D [$10^{-6}\text{cm}^2\text{s}^{-1}$]
37.5	5.3	3.7	75.5	0.20	0.22	38	1	2.8
50	5.4	3.4	97.7	0.17	0.19	27	1	3.0
100	17.3	4.3	255.2	0.10	0.12	33	1	2.4

The diffusion coefficients in Table 1 were calculated from the estimated value of τ_z , using the relation $D = h^2/4\tau_z$. The value of h was estimated from the numerical calculations of the MDE to be 64 nm. Values for the structure parameter, ω , that were derived from the data, are in excellent agreement with values ω_t , that were obtained from the numerically calculated MDEs. Also values for D coincide to a satisfactory degree with values previously published [23]. For a pinhole diameter of 100 μm , the MDE function is not well approximated by equation 5, which explains the deviations of the values τ_z and D in this case. However, these values are all in the same range, which is to be expected, because changing the pinhole diameter should only marginally change the axial extent of the MDE.

6. Conclusion

By adapting an objective-type TIRF setup for FCS measurements, a very sensitive system is obtained. High counts per molecule (cpm) are achieved due to the good light collection efficiency inherent to this system. A small observation volume decreases background and measurement artifacts. The signal to background ratio is excellent, as can be inferred from intensity time traces of single molecules adsorbing to a glass slide, or more indirectly from TIR-FCS measurements. Numerical calculations of the observation volume are in good agreement with experimental TIR-FCS data, obtained for freely diffusing fluorophores. In particular, the diffusion coefficient and structure parameters derived from experimental data are in good agreement with reported and theoretical values. The system allows for simultaneous parallel TIRF imaging by simply connecting a camera to a second port of the microscope. All these features, in addition easy handling and excellent stability, make the proposed set-up perfectly suitable for surface FCS measurements on a single molecule level.

Acknowledgment

We thank Mona Wells for careful reading of the manuscript and helpful discussions. This research was supported by the Swiss National Science Foundation (SNSF).

CV

Curriculum vitae

Kai Haßler

Born on December 16, 1975 in Graz, Austria; Austrian nationality; single.

Education

2001–2005 Ph.D. candidate at the Laboratoire d’Optique Biomédicale, Ecole Polytechnique Fédérale de Lausanne, Switzerland.

Thesis title: “Single molecule detection and fluorescence correlation spectroscopy on surfaces”

Supervisor: Prof. Theo Lasser

1994–2001 University degree in theoretical physics, University of Vienna, Austria.

Degree: Mag. rer. nat.

Diploma work: “Zum Begriff der quasilokalen Masse am Beispiel von axialsymmetrischen pp-Wellen”

Supervisor: Prof. Peter C. Aichelburg

1998/1999 Exchange student at University of Rennes 1, France.

1994 High school degree (Matura) at Bundesrealgymnasium Viktring, Austria.

Professional experience

Summer 2001 Research associate at the Austrian Academy of Science, Institute of High Energy Physics, Austria.

Project: Development of data processing software in the framework of the CMS project at CERN.

Summer 2000 Research associate at the Austrian Academy of Science, Institute of High Energy Physics, Austria.

Project: Development of a test-station for semiconductor sensors in the framework of the CMS project at CERN.

Language skills

German: mother tongue

English: fluent

French: fluent

Computer skills

Languages: C

Packages: Matlab, LabView

Software: MS Office, Adobe Illustrator, Latex

Systems: Windows, Linux, Unix

Hobbies

Mountaineering, climbing, skiing, long distance running.

Publications

- K. Hassler, M. Leutenegger, P. Rigler, R. Rao, R. Rigler, M. Gösch, and T. Lasser, “Total internal reflection fluorescence correlation spectroscopy (TIR-FCS) with low background and high count-rate per molecule,” *Opt. Exp.* **13**, 7415–7423 (2005).
- K. Hassler, T. Anhut, R. Rigler, M. Gösch, and T. Lasser, “High count rates with total internal reflection fluorescence correlation spectroscopy,” *Biophys. J.* **88**, L1–L3 (2005).
- K. Hassler, T. Anhut, and T. Lasser. “Time-resolved Hadamard fluorescence imaging,” *Appl. Opt.* **44**, 7564–7572 (2005)
- B. Karamata, K. Hassler, M. Laubscher, and T. Lasser. “Speckle statistics in optical coherence tomography,” *J. Opt. Soc. Am. A* **22**, 593–596 (2005).

Conference proceedings and patents

- System und Verfahren nach dem Hadamard Prinzip zur lateral aufgelösten Messung von Lichtsignalen, PCT/IB05/050739
- T. Anhut, K. Hassler, T. Lasser, K. König, and R. Rigler. “Fluorescence correlation spectroscopy on dielectric surfaces in total internal reflection geometries,” *Proc. SPIE* **5699**, 159–166 (2005).